Investigation of More Complete Constitutive Theories for Heat Conduction in Solids and for Deviatoric Stress Tensor in Incompressible Fluids

By

Sayali R. Kedari

Submitted to the Department of Mechanical Engineering and the
Graduate Faculty of the University of Kansas
in partial fulfillment of the requirements for the degree of
Master of Science

Prof. Karan S. Surana, Chairperson

Committee members

Prof. Peter TenPas

Prof. Robert Sorem

Date defended: August 12, 2016

The Thesis Committee for Sayali R. Kedari certifies
that this is the approved version of the following thesis :

Investigation of More Complete Constitutive Theories for Heat Conduction in Solids and for Deviatoric Stress Tensor in Incompressible Fluids

Prof. Karan S. Surana, Chairperson

Date approved: August 12, 2016

Abstract

This thesis presents numerical studies utilizing more complete constitutive theories for: (i) Heat vector in isotropic, homogeneous, incompressible, elastic solid continua and (ii) Deviatoric stress tensor for isotropic, homogeneous, incompressible, viscous fluids without memory. The derivation of the constitutive theories for heat vector in Lagrangian description for solid continua and for deviatoric stress tensor for incompressible fluent continua without memory in Eulerian description, using theory of generators and invariants, have been presented by Surana, Reddy, Eringen [1–4]. These theories utilize integrity i.e. complete basis, hence are complete. A serious shortcoming of these theories is that they require too many material coefficients that must be determined experimentally. Due to the lack of availability of the material coefficients, these theories have not been used commonly in applications, instead their simplified forms requiring fewer material coefficients are currently being used. The purpose of this investigation is to study the influence of additional terms in the more complete constitutive theories derived using integrity that are routinely neglected to examine the influence of the additional physics that is introduced in the constitutive theories by their presence and their impact in applications.

In specific, the first study focuses on constitutive theory for heat conduction in Lagrangian description for solid continua in which the argument tensors of heat vector $\boldsymbol{q}$ are temperature gradient $\boldsymbol{g}$ and temperature θ and the constitutive theory for $\boldsymbol{q}$ is based on integrity and is derived using theory of generators and invariants [1–4]. The second study considers incompressible, viscous fluids without memory in which the constitutive theory for the deviatoric Cauchy stress tensor is also based on theory of

generators and invariants in which symmetric part of velocity gradient tensor ($[\bar{D}]$) and its square ($[\bar{D}]^2$) are combined generators of its argument tensors.

1D transient heat conduction in a rod, fully developed flow between parallel plates, square lid driven cavity and asymmetric expansion are used as model problems to illustrate the significance of the newer constitutive theories considered here.

Acknowledgements

I would like to take this opportunity to acknowledge those who helped and supported me during my masters program. First and foremost I want to thank my advisor, Dr. Karan Surana. I have been constantly inspired and motivated by his knowledge and enthusiasm, and all of the work done in this thesis would have been impossible without his guidance. I am truly grateful for the work he has done to ensure I graduate in a timely manner. I also would like to thank Dr. Peter W. TenPas and Dr. Robert Sorem for serving on my committee. I am grateful to both of them, as I have learnt tremendously while taking courses as well as working with them.

I would like to thank Dr. Surana, the 'Mechanical' and the 'Physics and Astronomy' departments for providing financial support during my graduate studies.

There are others who also deserve to be recognized for their contributions to my success. I am thankful to my friends and the students in the Computational Mechanics program and Mechanical department, both past and present, for the work they have done that has led to this, as well as for the support during hard times.

Finally, I would like to thank my parents and my sister for their love, encouragement and support.

Contents

List of Figures

List of Symbols

Solids (Lagrangian description)

$\hat{c_v}$: Specific heat

c_v : Dimensionless specific heat

$\hat{k}$: Thermal conductivity

k : Dimensionless thermal conductivity

$\hat{k}_1$: Material coefficient associated with first higher degree term

k_1 : Dimensionless material coefficient associated with first higher degree term

$\hat{\theta}$: Temperature

θ : Dimensionless Temperature

$\hat{\rho}$: Density

ρ : Dimensionless density

L_0 : Reference length

k_0 : Reference thermal conductivity

$\hat{\boldsymbol{q}}$: Heat vector

$\hat{\boldsymbol{g}}$: Temperature gradient

Fluids (Eulerian description)

$\hat{\overline{\rho}}$: Density

$\overline{\rho}$: Dimensionless density

$\hat{\eta}$: Zero shear rate viscosity

η : Dimensionless zero shear rate viscosity

$\hat{\eta_1}$: Material coefficient associated with first higher degree term

η_1 : Dimensionless material coefficient associated with first higher degree term

$\hat{\eta_3}$: Material coefficient associated with second higher degree term

η_3 : Dimensionless material coefficient associated with second higher degree term

$\hat{\overline{p}}$: Mechanical pressure

$\overline{p}$: Dimensionless mechanical pressure

$\frac{\partial \overline{p}}{\partial \overline{x}}$: Dimensionless mechanical pressure gradient w.r.t x

$\frac{\partial \overline{p}}{\partial \overline{y}}$: Dimensionless mechanical pressure gradient w.r.t y

$\overline{u}$: Dimensionless velocity in x direction

$\overline{v}$: Dimensionless velocity in y direction

${}_d\overline{\sigma}_{xx}$: Dimensionless normal stress in x direction

$({}_d\overline{\sigma}_{xx})_l$: Dimensionless normal stress (linear term) in x direction

$({}_d\overline{\sigma}_{xx})_{nl}$: Dimensionless normal stress (non-linear term) in x direction

${}_d\overline{\sigma}_{yy}$: Dimensionless normal stress in y direction

$({}_d\overline{\sigma}_{yy})_l$: Dimensionless normal stress (linear term) in y direction

$({}_d\overline{\sigma}_{yy})_{nl}$: Dimensionless normal stress (non-linear term) in y direction

${}_d\overline{\sigma}_{xy}$: Dimensionless shear stress in xy plane

Re : Reynold's number

$\hat{\bar{x}}$: x co-ordinate

$\bar{x}$: Dimensionless x co-ordinate

$\hat{\bar{y}}$: y co-ordinate

$\bar{y}$: Dimensionless y co-ordinate

τ_0 : Reference stress

ρ_0 : Reference density

u_0 : Reference velocity

L_0 : Reference length

η_0 : Reference viscosity

$\bar{\boldsymbol{v}}$: Velocity vector

${}_d\overline{\boldsymbol{\sigma}}$: Deviatoric Cauchy stress tensor

$\bar{\boldsymbol{D}}$: Symmetric part of the velocity gradient tensor

$\boldsymbol{I}$: Identity tensor

Chapter 1

Introduction, Literature Review and Scope of Work

The constitutive theories for heat conduction in solids and for deviatoric stress tensor in fluids considered here are rather fundamental in all solid and fluent continua. Fourier heat conduction law [5–7] stating that heat is proportional to the temperature gradient is the result of experimental observation resulting from heat conduction experiments by Fourier with metal tubes and rods. Based on this, heat vector is equal to a material coefficient, thermal conductivity times the temperature gradient in which the thermal conductivity can be a function of temperature. For many simple materials, this constitutive theory for heat vector may be sufficient to describe the physics in applications. However, this constitutive theory lacks thermodynamics basis or continuum mechanics foundation which may reveal other possibilities for the constitutive theories for heat vector that may perhaps enable us to incorporate more complex physics if so desired in applications. It is now well established that [1–4] all deforming matter if in thermodynamic equilibrium must satisfy laws of thermodynamics i.e. conservation and balance laws. Out of these, only the second law of thermodynamics (entropy inequality) provides possible mechanism or conditions through which constitutive theories for the deforming matter can be derived. When this approach is not possible we use conjugate pairs resulting from entropy inequality and the theory of generators and

invariants to derive desired constitutive theories. The constitutive theories so derived using both approaches are more comprehensive, specially those using theory of generators and invariants than simple Fourier heat conduction law. In the present work, a small subset of these theories are explored numerically using model problems to understand benefits of such theories over standard Fourier heat conduction law.

The second aspect of the present work is the investigation of the constitutive theories for deviatoric stress tensor for incompressible fluids derived using entropy inequality in conjunction with the theory of generators and invariants with the aim of understanding if such theories will enable a more comprehensive treatment of the physics of fluid flow. This work is motivated by closer examination of the Newton's law of viscosity in which the deviatoric stress tensor is proportional to the symmetric part of velocity gradient tensor, an extremely limiting case of general constitutive theory for the deviatoric stress tensor based on integrity, hence perhaps limiting in describing the physics of deformation. Specifically, in the present work, theory of generators and invariants is used [1–4] to derive constitutive theory for the deviatoric contravariant Cauchy stress tensor in which symmetric part of the velocity gradient tensor and its square are used as generators.

1D transient heat conduction in a rod, fully developed flow between parallel plates, a square lid driven cavity and asymmetric sudden expansion are used as model problems. The model problems for fluid flow are boundary value problems. In all model problems, the simulations using the constitutive theories described here are compared with the classical constitutive theories used currently to illustrate the additional physics described by these theories.

Chapter 2

Heat Conduction in Thermoelastic Solids

2.1 Introduction

The classical Fourier heat conduction law [5–7] used for solids as well as fluids is given by

$$\boldsymbol{q} = -k(\theta)\boldsymbol{g} \tag{2.1}$$

in which $\boldsymbol{q}$ is heat vector, θ is temperature, $k(\theta)$ is temperature dependent thermal conductivity and $\boldsymbol{g}$ is temperature gradient given by

$$\boldsymbol{g} = \boldsymbol{\nabla}(\theta) \tag{2.2}$$

Power law, Sutherland law etc. [1, 8, 9] are generally used to describe temperature dependent thermal conductivity. For thermoelastic solids that are continuous media, the Fourier heat conduction law or its alternate forms must be derivable using principles of thermodynamics or principles of continuum mechanics. It is now well established [1–4] that the second law of thermodynamics or entropy inequality forms the basis for the derivations of the constitutive theories. It establishes conjugate pairs and condition that must not be violated by the constitutive theories. In case of thermoelastic solids, the entropy inequality expressed in terms of Helmholtz Free energy density ϕ require that

$$\frac{\boldsymbol{q}\cdot\boldsymbol{g}}{\theta} \leq 0 \quad \text{or} \quad \boldsymbol{q}\cdot\boldsymbol{g} \leq 0 \tag{2.3}$$

must hold. Inequality (2.3) can be viewed in two ways,

(i) find a $\boldsymbol{q}$ that satisfies (2.3)

(ii) the inequality (2.3) implies that $\boldsymbol{q}$ is conjugate to $\boldsymbol{g}$ and $\boldsymbol{g}$ is conjugate to $\boldsymbol{q}$, hence $\boldsymbol{q} = \boldsymbol{q}(\boldsymbol{g}, \theta)$ in which $\boldsymbol{g}$ and θ are argument tensors of $\boldsymbol{q}$ can be used in conjunction with the theory of generators and invariants to derive a constitutive theory for $\boldsymbol{q}$.

Both approaches have been considered [1] and the constitutive theories have been derived. These are summarized in the following section.

2.2 Constitutive theories for $\boldsymbol{q}$

2.2.1 Strictly using the condition resulting from entropy inequality

Using (2.3) and following reference [1], it is straightforward to derive the following:

$$\boldsymbol{q} = -k(\theta)\boldsymbol{g} \quad ; \quad \boldsymbol{g} = \boldsymbol{\nabla}(\theta) \tag{2.4}$$

in which $k(\theta)$ is a scalar material coefficient, the temperature dependent thermal conductivity. Since the solid matter is isotropic and homogeneous, the following form of the constitutive theory is not admissible.

$$q_i = -k_{ij} g_j \tag{2.5}$$

In (2.5), k_{ij} is viewed as non-symmetric or symmetric thermal conductivity matrix for anisotropic or orthotropic matter.

2.2.2 Using $\boldsymbol{q} = \boldsymbol{q}(\boldsymbol{g}, \theta)$

In this approach, we consider $\boldsymbol{g}$ and θ as argument tensors of $\boldsymbol{q}$. This is supported by entropy inequality. $\boldsymbol{q}$ and $\boldsymbol{g}$ are tensors of rank one whereas θ is a tensor of rank zero. The combined generators of $\boldsymbol{g}$ and θ that are tensors of rank one is just $\boldsymbol{g}$ and the combined invariants is ${}^{q}I = \boldsymbol{g} \cdot \boldsymbol{g} = \{g\}^T \{g\}$. Thus, we can express $\boldsymbol{q}$ as [1]

$$\{q\} = -{}^{q}\alpha\{g\} \tag{2.6}$$

in which ${}^{q}\alpha = {}^{q}\alpha({}^{q}I, \theta, \rho_0)$

Expanding ${}^{q}\alpha$ in Taylor series in ${}^{q}I$ and θ about a known configuration $\underline{\Omega}$ and retaining only up to linear terms in ${}^{q}I$ and θ and then substituting ${}^{q}\alpha$ back in (2.6) yields (neglecting θ term)

$$\{q\} = -k\{g\} - k_1(\{g\}^T\{g\})\{g\} \tag{2.7}$$

in which

$$k = k({}^{q}I|_{\underline{\Omega}}, \theta|_{\underline{\Omega}}, \rho_0) \quad \text{and} \quad k_1 = k_1({}^{q}I|_{\underline{\Omega}}, \theta|_{\underline{\Omega}}, \rho_0) \tag{2.8}$$

The constitutive theory for $\boldsymbol{q}$ given by (2.7) is the simplest possible constitutive theory based on theory of generators and invariants. We note that (2.5) is recoverable from (2.7) if the second term on the right side of (2.7) is discarded and if we assume that k only depends upon θ.

2.2.3 Energy equation

For isotropic, homogeneous, incompressible solid in Lagrangian description [1], the energy equation can be written as (in the absence of sources sinks and dissipations)

$$\rho_0 c_v \frac{\partial \theta}{\partial t} + \boldsymbol{\nabla} \cdot \boldsymbol{q} = 0 \qquad \forall (x,t) \in \Omega_{xt} = \Omega_x \times \Omega_t = (0,L) \times (0,\tau) \tag{2.9}$$

in which $\boldsymbol{q}$ is defined by (2.7) from which standard Fourier heat conduction law can be derived by only retaining $k = k(\theta)$. Equations (2.7) and (2.9) provide energy equation in which the constitutive theory for $\boldsymbol{q}$ is based on integrity, hence more complete. Alternatively, (2.7) can be substituted in (2.9) and assuming constant k and k_1, we obtain the following for one dimensional case (in $\mathbb{R}^1$).

$$\rho_0 c_v \frac{\partial \theta}{\partial t} - k\frac{\partial^2 \theta}{\partial x^2} - 3k_1 \left(\frac{\partial \theta}{\partial x}\right)^2 \frac{\partial^2 \theta}{\partial x^2} = 0 \qquad \forall (x,t) \in \Omega_{xt} = \Omega_x \times \Omega_t = (0,L) \times (0,\tau) \tag{2.10}$$

2.2.4 Dimensionless form of the energy equation in $\mathbb{R}^1$

First we express all quantities with hat ($\hat{}$) in (2.10) implying that they all have their usual dimensions.

$$\hat{\rho_0}\hat{c_v}\frac{\partial\hat{\theta}}{\partial\hat{t}} - \hat{k}\frac{\partial^2\hat{\theta}}{\partial\hat{x}^2} - 3\hat{k_1}\left(\frac{\partial\hat{\theta}}{\partial\hat{x}}\right)^2\frac{\partial^2\hat{\theta}}{\partial\hat{x}^2} = 0 \tag{2.11}$$

We choose the following reference quantities (with subscript zero or the subscript 'ref') and the dimensionless variables (without hat($\hat{}$)).

$$\begin{aligned} x &= \frac{\hat{x}}{L_0} \quad , \quad \theta = \frac{\hat{\theta}}{\theta_0} \quad , \quad \rho = \frac{\hat{\rho}_0}{(\rho_0)_{ref}} \quad , \quad c_{v_0} = \frac{\hat{c}_v}{c_{v_0}} \\ k &= \frac{\hat{k}}{k_0} \quad , \quad t = \frac{\hat{t}}{t_0} \end{aligned} \tag{2.12}$$

Using (2.12) in (2.11), the following can be obtained.

$$\frac{(\rho_0)_{ref}c_{v_0}\theta_0}{t_0}\rho c_v\frac{\partial\theta}{\partial t} - \frac{k_0\theta_0}{{L_0}^2}k\frac{\partial^2\theta}{\partial x^2} - \left(\frac{{\theta_0}^2}{{L_0}^2}\right)\frac{\theta_0}{{L_0}^2}(3\hat{k_1})\left(\frac{\partial\theta}{\partial x}\right)^2\frac{\partial^2\theta}{\partial x^2} = 0 \tag{2.13}$$

or

$$\frac{(\rho_0)_{ref}c_{v_0}{L_0}^2}{k_0t_0}\rho c_v\frac{\partial\theta}{\partial t} - k\frac{\partial^2\theta}{\partial x^2} - \left(\frac{{\theta_0}^2}{{L_0}^2k_0}\right)3\hat{k_1}\left(\frac{\partial\theta}{\partial x}\right)^2\frac{\partial^2\theta}{\partial x^2} = 0 \tag{2.14}$$

$$\text{Let} \quad t_0 = \frac{L_0^2(\rho_0)_{ref}c_{v_0}}{k_0} \quad \text{and} \quad \hat{k_1} = k_1(k_1)_{ref} \tag{2.15}$$

Using (2.15) in (2.14),

$$\rho c_v\frac{\partial\theta}{\partial t} - k\frac{\partial^2\theta}{\partial x^2} - \left(\frac{{\theta_0}^2}{{L_0}^2k_0}\right)(k_1)_{ref}(3k_1)\left(\frac{\partial\theta}{\partial x}\right)^2\frac{\partial^2\theta}{\partial x^2} = 0 \tag{2.16}$$

If we choose $(k_1)_{ref} = \dfrac{k_0L_0^2}{\theta_0^2}$, then (2.16) reduces to

$$\rho c_v\frac{\partial\theta}{\partial t} - k\frac{\partial^2\theta}{\partial x^2} - 3k_1\left(\frac{\partial\theta}{\partial x}\right)^2\frac{\partial^2\theta}{\partial x^2} = 0 \tag{2.17}$$

Equation (2.17) is the final form of 1D energy equation with constant material coefficients. We perform numerical studies using (2.17).

2.3 Numerical Studies

In this section, two numerical studies are presented using the energy equation (2.17). Computations are performed using space-time least squares finite element formulation based on space-time residual functional [10] for non-linear space-time differential operators in which a space-time strip for an increment of time Δt is discretized using a row of p-version hierarchical space-time higher order global differentiability finite elements. The non-linear algebraic equations are solved using Newton's linear method with line search. The evolution is computed for an increment of time and when converged, then is time marched to compute the entire evolution for desired final value of time. The computational processes in this approach are unconditionally stable throughout the evolution.

The first numerical study consists of 1D heat conduction in a rod of length $L(0 \leq x \leq L)$. The left end ($x = 0$) is insulated and the right end is subjected to a change in temperature over time Δt from θ_1 to θ_2. (θ_1 being initial condition) and thereafter kept θ_2 for all values of time beyond Δt. The second model problem consists of the same rod as in model problem-I in which the left and the right ends are insulated and the initial condition consists of a Gaussian distribution centered at $x = 0.2$ (for $L = 1.0$). We consider numerical studies of the evolution with space-time coupled finite element method for an increment of time Δt. Upon convergence, the solution is time marched till the entire evolution is obtained.

2.3.1 Model problem – I: 1D transient heat conduction in a rod

Consider a rod of uniform cross-section. The left end of the rod is insulated and the right end of the bar is subjected to a continuous and differentiable temperature change from θ_1 to θ_2 ($\theta_2 > \theta_1$) over an increment of time Δt and $\theta = \theta_2$ for $t > \Delta t$. For $0 \leq t \leq \Delta t$, θ is a cubic distribution in time

over Δt such that $\theta = \theta_1$ at $t = 0$ and $\left.\dfrac{\partial \theta}{\partial t}\right|_{t=0} = 0$ and $\theta|_{\Delta t} = \theta_2$, $\left.\dfrac{\partial \theta}{\partial t}\right|_{\Delta t} = 0$. Figure 2.1 shows a schematic with boundary conditions and figure 2.2 shows θ as a function of time for $0 \leq t \leq \Delta t$.

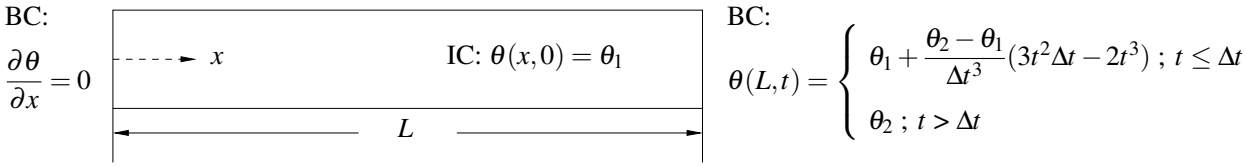

Figure 2.1: Schematic of 1-D heat conduction in a thermoelastic solid

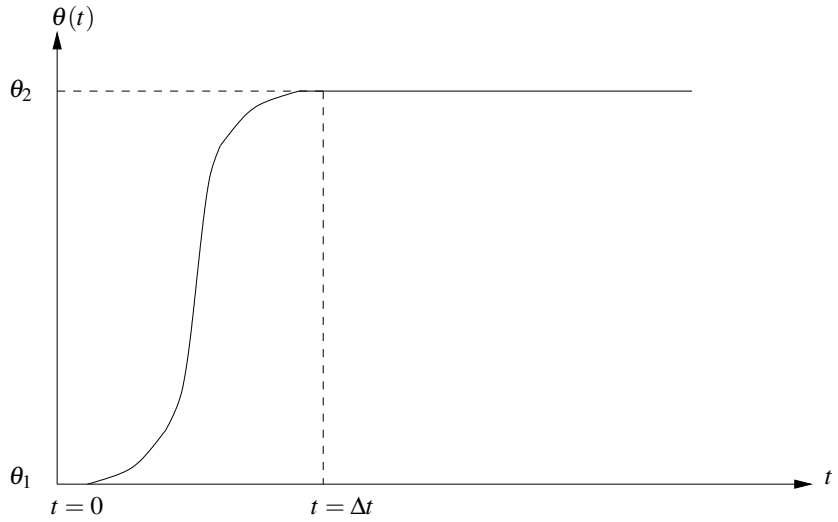

Figure 2.2: Boundary condition $\theta(t)$ at $x = L$

In the computations of the numerical solutions we choose [11]

$$L_0 = \hat{L} = 0.1 \text{ m} \quad ; \quad \theta_0 = \hat{\theta}_1 = 300 \text{ K} \quad ; \quad (\rho_0)_{ref} = \hat{\rho}_0 = 2700 \text{ kg/m}^3$$

$$c_{v_0} = \hat{c}_v = 903.0 \text{ J/kg.K} \quad ; \quad k_0 = \hat{k} = 237 \text{ Watt/m.K}$$

which gives

$$L = 1 \quad ; \quad \theta_1 = 1 \quad ; \quad \rho = 1 \quad ; \quad c_v = 1 \quad ; \quad k = 1 \quad ; \quad k_1 = 37974.68\hat{k}_1$$

A ten element uniform mesh with element length of 0.1 in space and time step of $\Delta t = 0.1$ is used in the present study (figure 2.3). The local approximations are p-version (9-node elements)

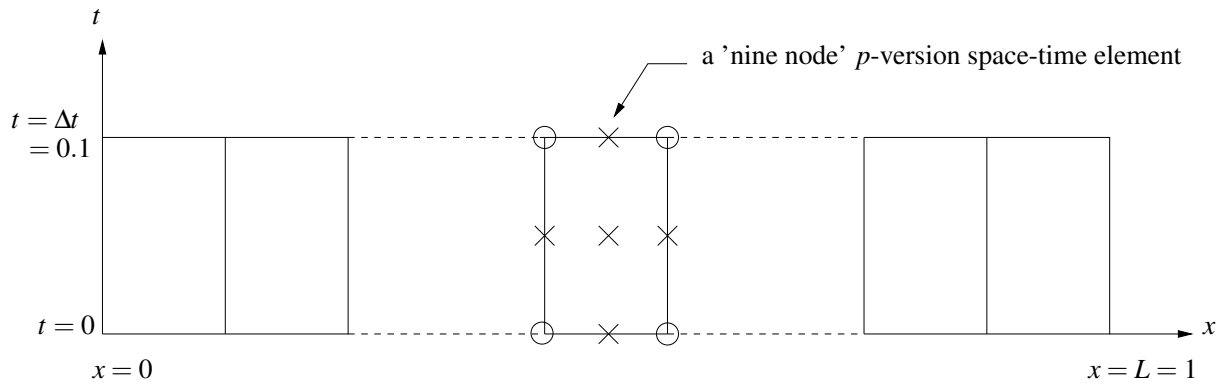

Figure 2.3: Uniform space-time discretization of the first space-time strip using ten 'nine-node' p-version space-time elements

in higher order spaces. Initial p-convergence studies with this discretization suggest that p = 11 with k = 2, local approximations of class $C^{1,1}(\Omega^e_{xt})$ are sufficient for good accuracy of results. The residual or least squares functional values for the space-time strip remain $O(10^{-16}) - O(10^{-14})$ indicating that the PDEs are satisfied accurately. Newton's linear method used for solving the non-linear algebraic equations converges in less than 7 iterations for all increments of time. In the numerical studies, we consider the following dimensionless values of temperature θ_2:

$$\theta_2 = 1.2 \quad ; \quad \theta_2 = 1.3 \quad ; \quad \theta_2 = 1.7 \quad ; \quad \theta_2 = 2.5 \tag{2.18}$$

which corresponds to θ_2 values of 360 K (86.85°C), 390 K (116.85°C), 510 K (236.85°C) and 750 K (476.85°C). We chose the following values of the coefficient $\hat{k_1}$.

$$\hat{k_1} = 0.0000 \text{ W/m.K}^3 \quad ; \quad \hat{k_1} = 0.0001 \text{ W/m.K}^3 \quad ; \quad \hat{k_1} = 0.0005 \text{ W/m.K}^3 \tag{2.19}$$

The corresponding values of k_1 are 0.00, 3.7975 and 18.987. When $\hat{k_1} = 0.0000$, (2.7) reduces to the standard Fourier heat conduction equation. The values of $\hat{k_1}$ are chosen so that with progressively increasing temperature gradient, we can observe the influence of the non-linear terms and hence, deviation from the Fourier heat conduction law.

Figures 2.4 – 2.11 show graphs of evolution of temperature θ versus distance x and evolution of temperature gradient $\frac{\partial \theta}{\partial x}$ versus distance x for different values of θ_2 but for the same choices of k_1.

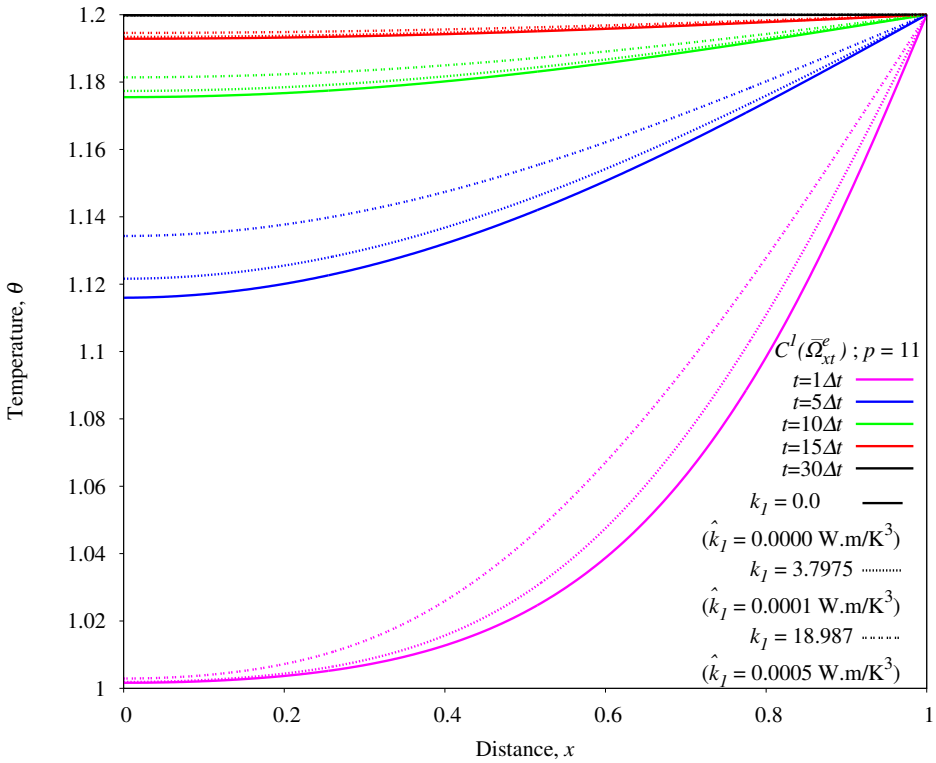

Figure 2.4: Temperature θ versus distance x for a prescribed $\theta_2 = 1.2$

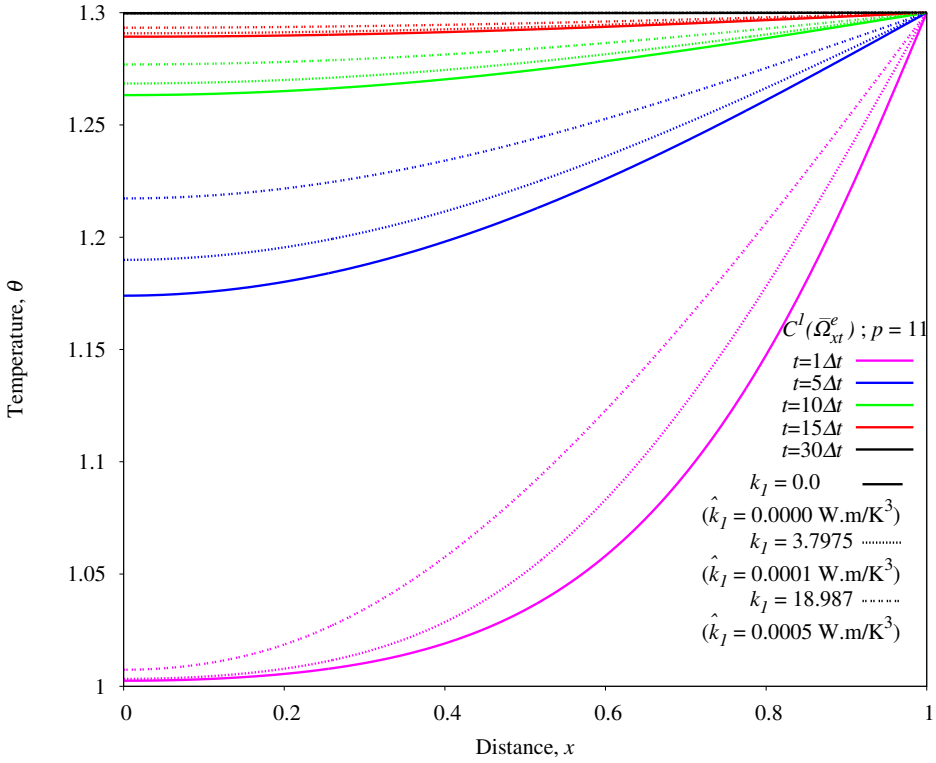

Figure 2.5: Temperature θ versus distance x for a prescribed $\theta_2 = 1.3$

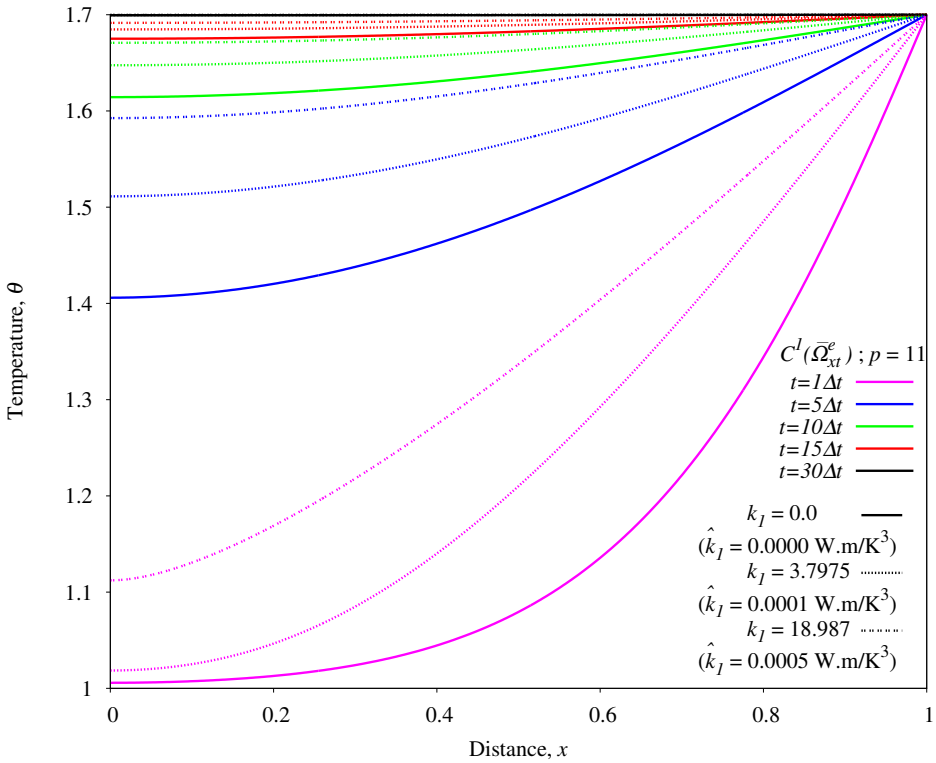

Figure 2.6: Temperature θ versus distance x for a prescribed $\theta_2 = 1.7$

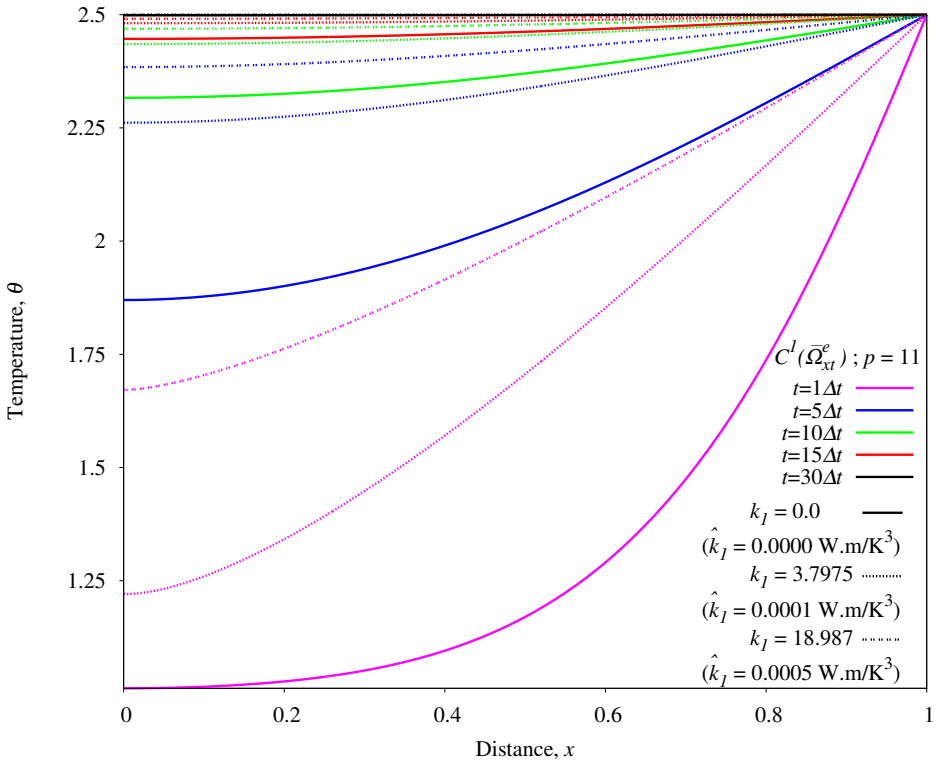

Figure 2.7: Temperature θ versus distance x for a prescribed $\theta_2 = 2.5$

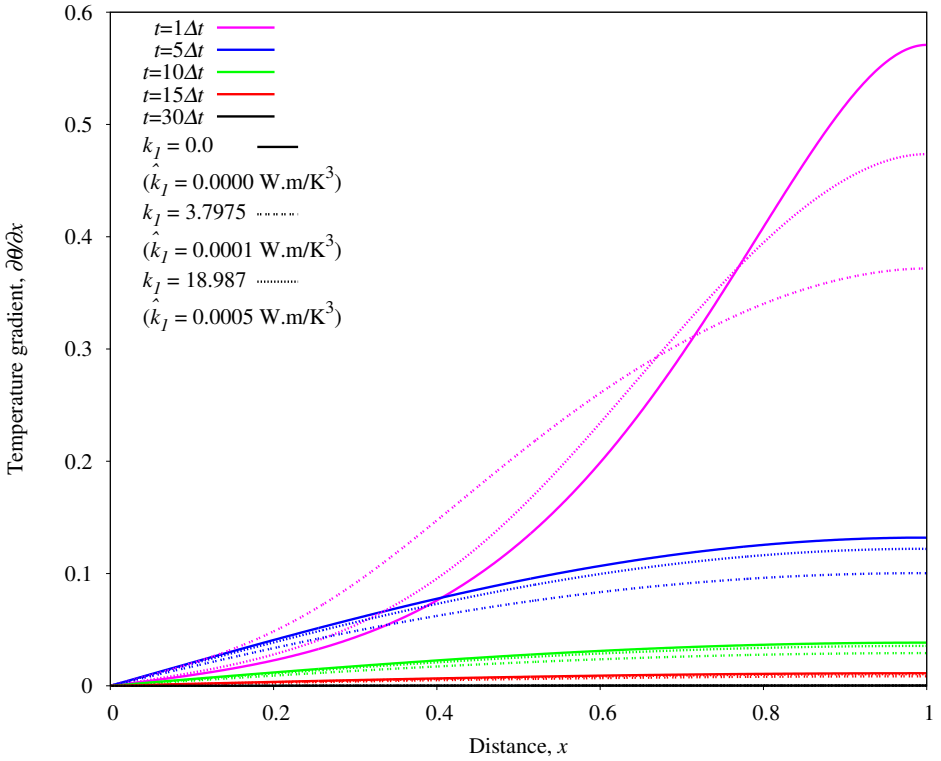

Figure 2.8: Temperature gradient $\frac{\partial \theta}{\partial x}$ versus distance x for a prescribed $\theta_2 = 1.2$

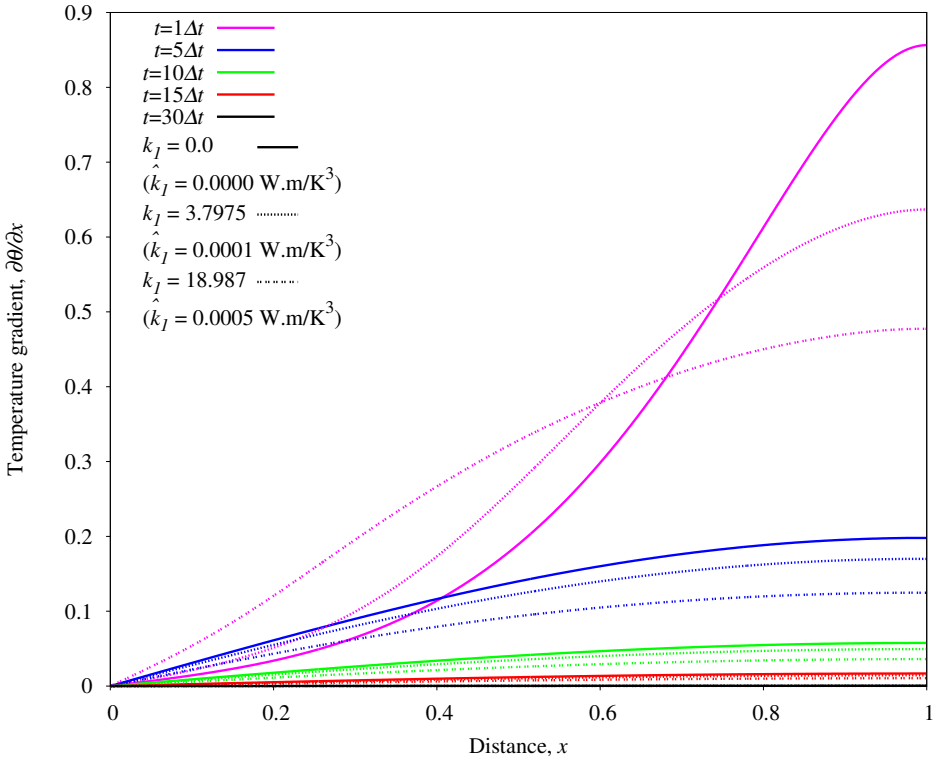

Figure 2.9: Temperature gradient $\frac{\partial \theta}{\partial x}$ versus distance x for a prescribed $\theta_2 = 1.3$

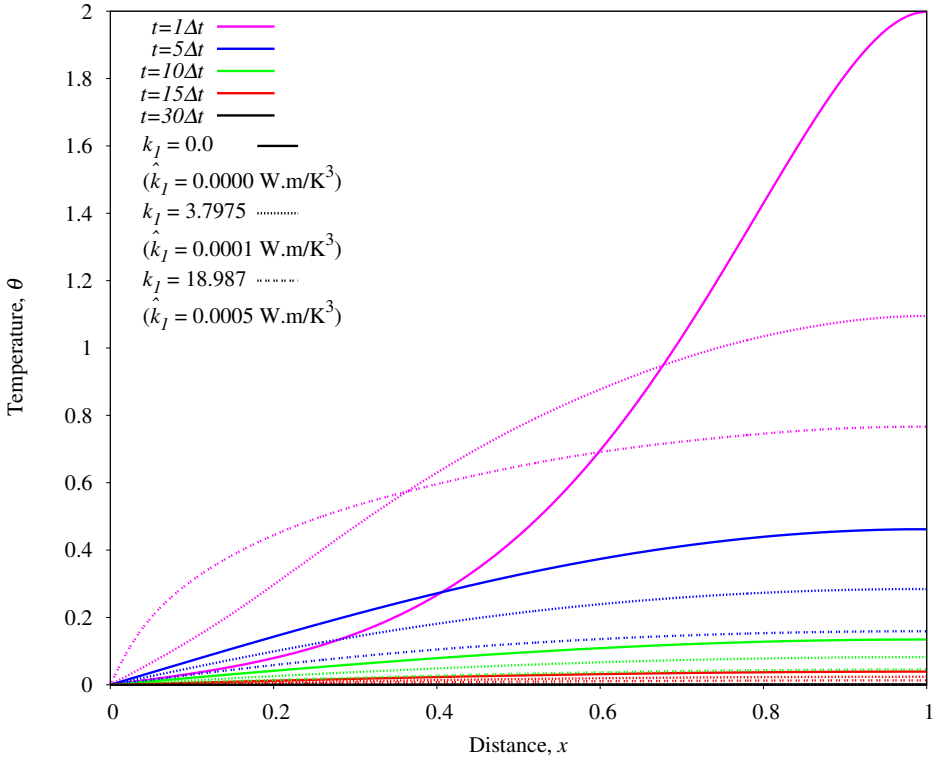

Figure 2.10: Temperature gradient $\frac{\partial \theta}{\partial x}$ versus distance x for a prescribed $\theta_2 = 1.7$

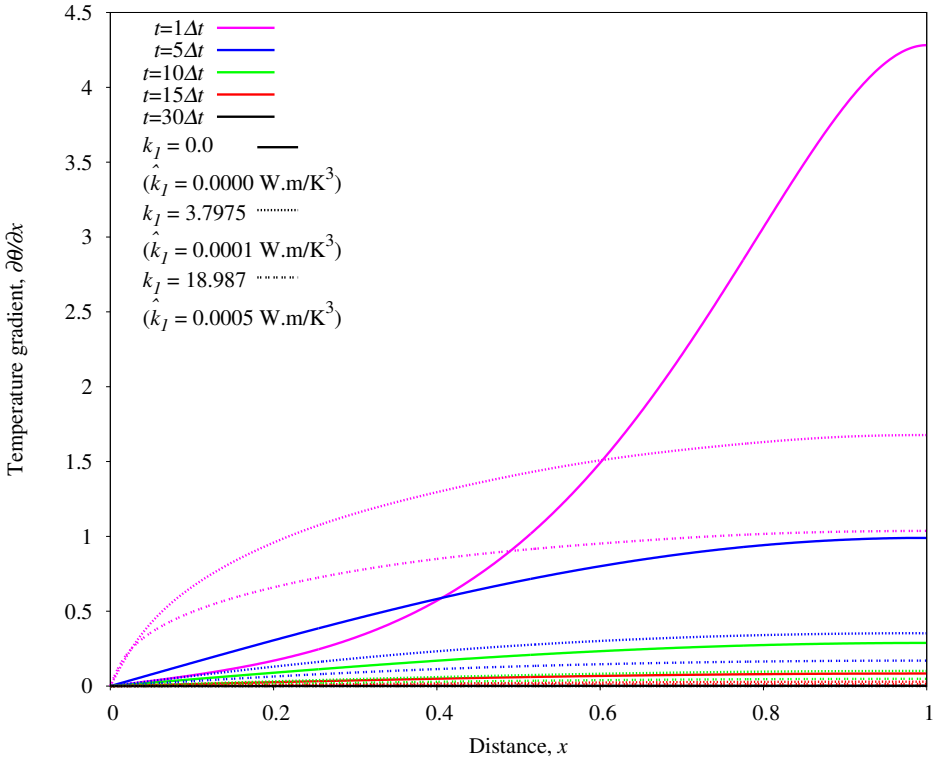

Figure 2.11: Temperature gradient $\frac{\partial \theta}{\partial x}$ versus distance x for a prescribed $\theta_2 = 2.5$

We observe that with progressively increasing values of θ_2, the numerical solutions obtained for non-zero k_1 begin to deviate from Fourier heat conduction law. For θ_2 = 2.5 (figure 2.7), the temperature distribution along the length of the rod differs significantly compared to Fourier heat conduction law. We also observe that with progressively increasing values of $\frac{\partial \theta}{\partial x}$ for certain value of θ_2, there is significant deviation from Fourier heat conduction law. The difference in temperature gradients for certain value of θ_2 and for different values of k_1 is not negligible and cannot be ignored. Larger value of k_1 obviously results in greater deviation from Fourier heat conduction law. The study demonstrates that (i) Lower values of k_1 (order of $O(10^{-4})$) affect heat conduction drastically; (ii) When temperature gradients are high, the non-linear constitutive theory for the heat vector may be a more realistic representation of the physics as opposed to standard Fourier heat conduction law.

2.3.2 Model problem – II: 1D transient heat conduction in a rod

In this case also, we consider 1D transient heat conduction with different boundary conditions and initial conditions. Figure 2.12 shows a schematic of the problem with boundary condition (both ends insulated and surface of the rod insulated as well).

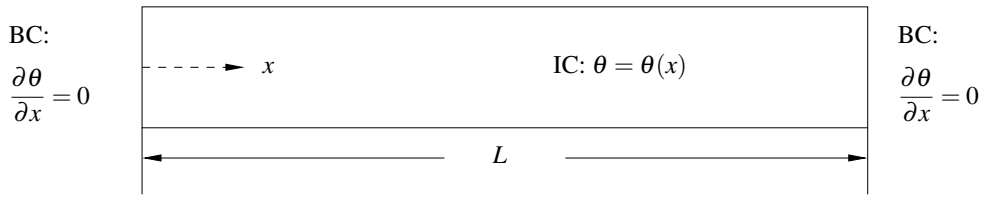

Figure 2.12: Schematic of 1-D heat conduction in a thermoelastic solid

Figure 2.13 shows initial condition at $t = 0$, a Gaussian distribution of temperature θ centered at $x = 0.2$ and with the support of $L = 1$ unit and a peak value of $\theta = 1$. The distribution ranges from 0 to 1 over $0.1 \leq x \leq 0.3$ in continuous and differentiable manner. Equation (2.20) describes a Gaussian distribution in which x_0 and σ_0 are mean and standard deviations of the distribution. [10]

$$\theta(x,0) = exp\left(-\frac{(x-x_0)^2}{2(\sigma_0)^2}\right) \tag{2.20}$$

We choose the mean and standard deviations of the initial Gaussian distribution to be $x_0 = 0.2$ and $\sigma_0 = 0.03$.

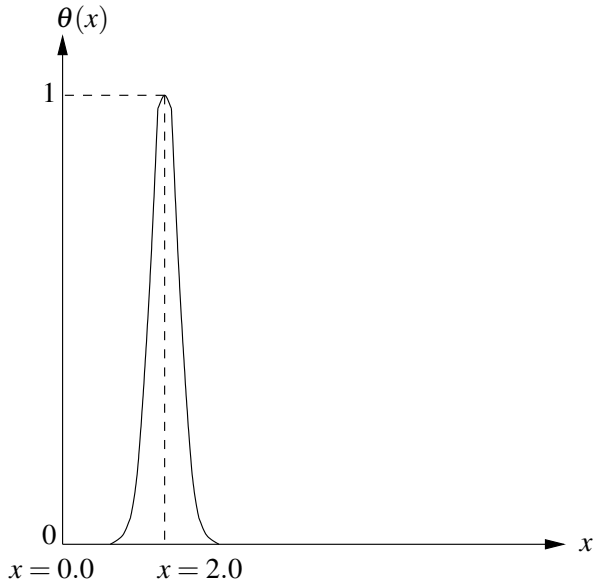

Figure 2.13: Initial condition $\theta(x)$ at $t = 0$: Gaussian Distribution

Initial p-convergence studies with this discretization (figure 2.3) suggest that $p = 7$ with $k = 2$, local approximations of class $C^{1,1}(\Omega^e_{xt})$ are sufficient for good accuracy of results. The residual or least squares functional values remain $O(10^{-18}) - O(10^{-14})$ indicating that the PDEs are satisfied accurately. Newton's linear method used for solving the non-linear algebraic equations converges in less than 7 iterations for all results. The following values of the coefficient $\hat{k_1}$ are used.

$$\hat{k_1} = 0.00\ W/m.K^3; \quad \hat{k_1} = 10^{-06}\ W/m.K^3; \quad \hat{k_1} = 5 \times 10^{-06}\ W/m.K^3; \quad \hat{k_1} = 10^{-05}\ W/m.K^3 \tag{2.21}$$

The corresponding values of k_1 are 0.00, 0.037975, 0.18987 and 0.37975. The values of $\hat{k_1}$ are chosen so that with progressively increasing value of $\hat{k_1}$, the change in the physics of heat conduction can be illustrated.

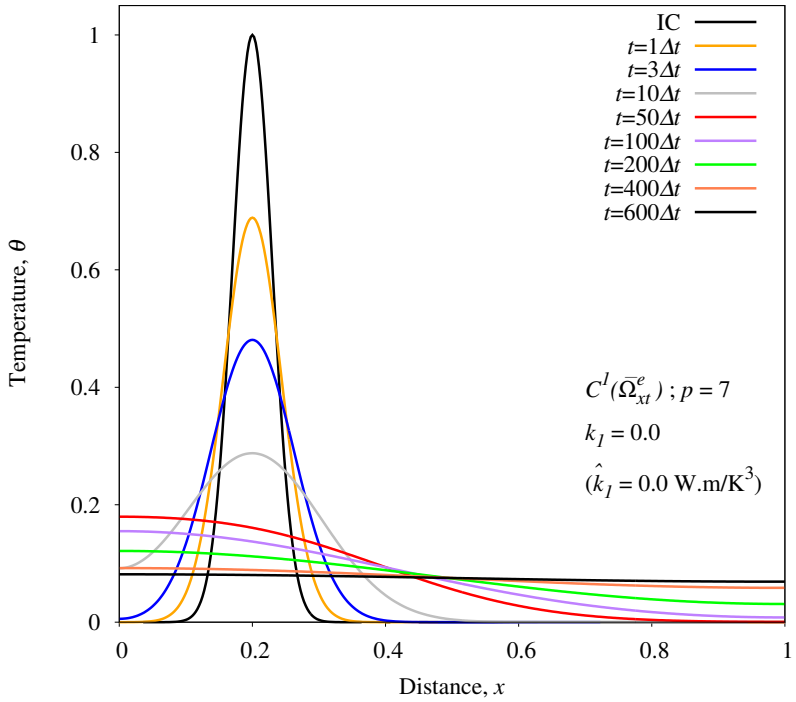

Figure 2.14: Temperature θ versus distance x for $\hat{k_1} = 0.00$ W/m.K^3

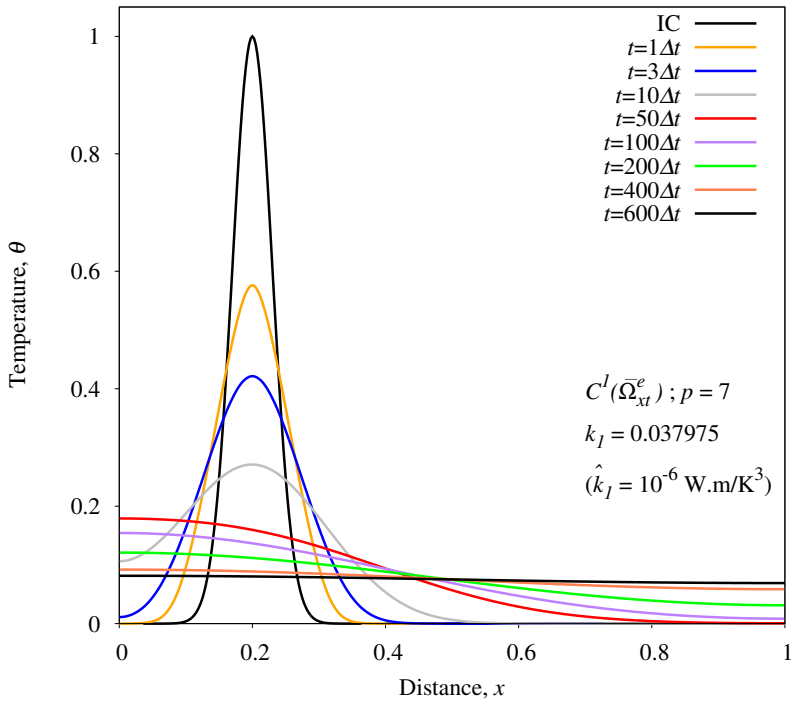

Figure 2.15: Temperature θ versus distance x for $\hat{k_1} = 10^{-06}$ W/m.K^3

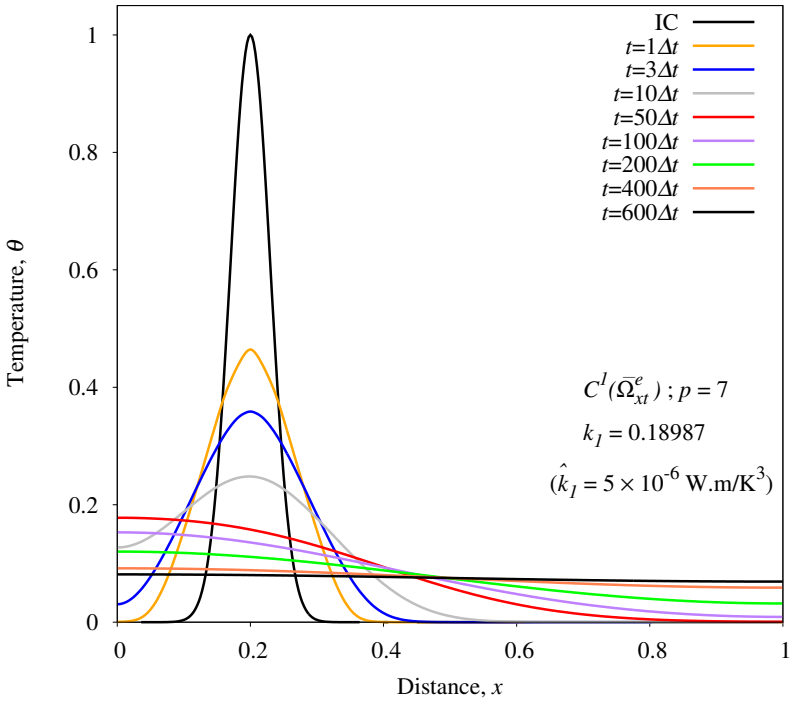

Figure 2.16: Temperature θ versus distance x for $\hat{k_1} = 5 \times 10^{-06}$ W/m.K^3

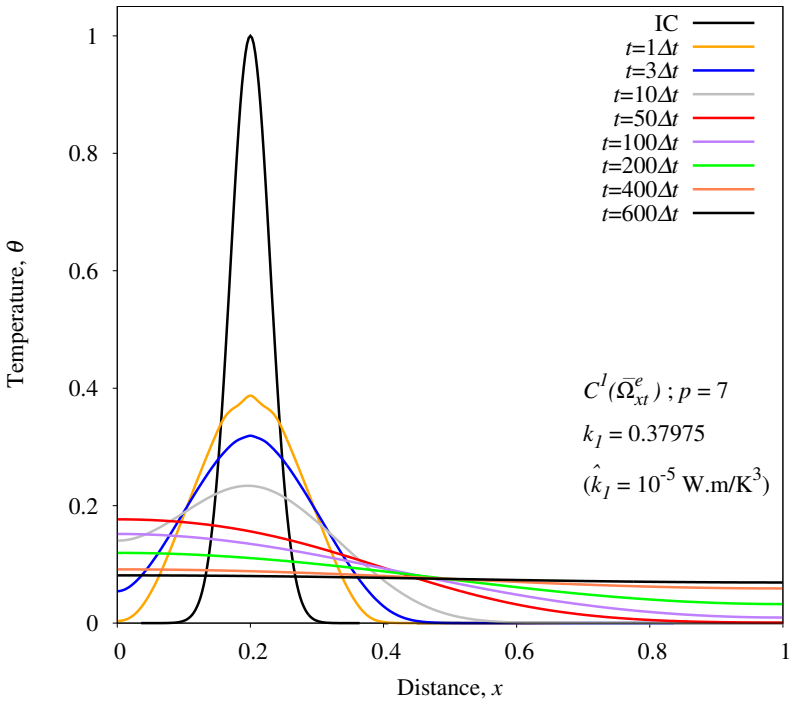

Figure 2.17: Temperature θ versus distance x for $\hat{k_1} = 10^{-05}$ W/m.K^3

Figures 2.14 – 2.17 show graphs of variation of temperature θ versus distance x for different values of $\hat{k_1}$. Comparatively, higher values of $\hat{k_1}$ result in faster decay of peak values and progressive base elongation. Here also lower values of k_1 (order of $O(10^{-6})$) affect heat conduction significantly.

2.4 Summary

A more complete constitutive theory for heat conduction in solid continua in Lagrangian description has been used to present numerical studies to demonstrate the significance and importance of this constitutive theory in high temperature heat transfer that often results in higher localized temperature gradients. The standard Fourier heat conduction law though can be derived using conditions resulting from entropy inequality is shown to be a limiting case [1–4] of more complete constitutive theory for heat vector based on theory of generators and invariants used here. The resulting constitutive theory for $\boldsymbol{q}$ is a cubic function of temperature gradients. Numerical studies for two model problems demonstrate: (i) With progressively increasing temperature gradients, the standard Fourier heat conduction law is inadequate. (ii) With the material coefficients k_1 of the order of $O(10^{-6}) - O(10^{-4})$, there is a significant deviation from the Fourier heat conduction law. (iii) The conductivity material coefficient depends on temperature θ as well as invariant of g i.e. $\{g\}^T\{g\}$ but in a known configuration.

Chapter 3

Constitutive Theory for Deviatoric Cauchy Stress Tensor for Viscous Fluids without Memory

3.1 Introduction

Newton's law of viscosity with constant or variable viscosity is used almost exclusively to describe constitutive theory for deviatoric Cauchy stress tensor for isotropic, homogeneous, viscous fluids without memory [9, 12]. Using Eulerian description [1–4], we can write

$$[{}_d\overline{\sigma}] = 2\eta[\bar{D}] \tag{3.1}$$

in which $[{}_d\overline{\sigma}]$ is the deviatoric Cauchy stress tensor, η is viscosity and $[\bar{D}]$ is the symmetric part of the velocity gradient tensor. When η is constant, equation (3.1) is said to describe Newtonian fluids and when $\eta = \eta(II_D, \theta)$, then equation (3.1) describes what are called generalized Newtonian fluids such as Power Law and Carreau Fluids. II_D is the second invariant of $[\bar{D}]$ based on characteristic equation of $[\bar{D}]$.

There is ample experimental evidence to support that equation (3.1) is an adequate constitutive

theory for deviatoric Cauchy stress tensor for simple fluids with relatively simple flow physics. In considering equation (3.1) as a constitutive theory for $[{}_d\overline{\sigma}]$, there are two major concerns:

(i) Since it describes constitutive behavior of a continuous media, is there a thermodynamic or continuum mechanics basis for its derivation?

(ii) If (i) is true, then it is worth investigating if there are assumptions or approximations involved in arriving at equation (3.1).

In the present work, either we cite published works to answer these questions or present new derivations. If there is a more comprehensive theory possible for $[{}_d\overline{\sigma}]$ than equation (3.1), then we consider such theories to present some numerical studies using some model boundary value problems such as 'fully developed flow between parallel plates', 'a square lid driven cavity' and 'asymmetric sudden expansion' and comparison with the results is obtained using equation (3.1) with the aim of observing and quantifying the additional physics described by the newer or more complete theories.

3.2 Constitutive theories for deviatoric Cauchy stress tensor

It is well established that for thermodynamic equilibrium in the deforming matter, entropy inequality must provide conditions or mechanism for deriving constitutive theories so that the derived constitutive theories will satisfy the entropy inequality. Following reference [1–4], for isotropic, homogeneous thermofluids (without memory) the deviatoric stress tensor ${}_d\overline{\boldsymbol{\sigma}}$ and $\bar{\boldsymbol{D}}$, the symmetric part of the velocity gradient tensor are conjugate. Based on reference [13], the choice of contravariant deviatoric Cauchy stress tensor is meritorious. We also note that $[\bar{D}]$ is the first convected time derivative of the Green's strain tensor. Since the first convected time derivative of green and Almansi strain tensor is $\bar{\boldsymbol{D}}$, the first convected time derivatives of co- and contravariant strain tensors are basis independent. Thus, as long as the constitutive theory for the deviatoric stress only depends on $[\bar{D}]$, we can use ${}_d\overline{\boldsymbol{\sigma}}$ for the deviatoric stress tensor as it is basis independent. Following [1], $[\bar{D}]$, $\overline{\rho}$ and $\overline{\theta}$ can be considered as argument tensors of ${}_d\overline{\boldsymbol{\sigma}}$, hence we can write

$$ {}_d\overline{\boldsymbol{\sigma}} = {}_d\,\overline{\boldsymbol{\sigma}}(\overline{\rho},\, \bar{\boldsymbol{D}},\, \overline{\theta}) \tag{3.2} $$

Constitutive theory for ${}_d\overline{\boldsymbol{\sigma}}$ can be derived using equation (3.2) in conjunction with theory of generators and invariants. The combined generators of the argument tensors of ${}_d\overline{\boldsymbol{\sigma}}$ that are symmetric tensors of rank two are $[\bar{D}]$ and $[\bar{D}]^2$ and there are three invariants of $[\bar{D}]$ either based on traces of $[\bar{D}]$, $[\bar{D}]^2$ and $[\bar{D}]^3$ or based on the characteristic equations. Thus we can write ${}_d\overline{\boldsymbol{\sigma}}$ (a symmetric tensor of rank two) as a linear combination of $[I]$, $[\bar{D}]$ and $[\bar{D}]^2$.

$$ [{}_d\overline{\sigma}] = {}^{\sigma}\alpha_0[I] + {}^{\sigma}\alpha_1[\bar{D}] + {}^{\sigma}\alpha_2[\bar{D}]^2 \tag{3.3} $$

in which

$$ {}^{\sigma}\alpha_i = {}^{\sigma}\alpha_i(I_\sigma, II_\sigma, III_\sigma) \tag{3.4} $$

$I_\sigma, II_\sigma, III_\sigma$ being invariants of $[\bar{D}]$.

Expanding ${}^{\sigma}\alpha_i, i = 0,1,2$ in Taylor series in $I_\sigma, II_\sigma, III_\sigma$ about a known configuration $\underline{\Omega}$ and retaining only up to linear terms in the invariants, we can obtain a general constitutive theory for ${}_d\overline{\boldsymbol{\sigma}}$. This theory uses complete basis or integrity, hence, is the most complete constitutive theory. In the present work, we consider a constitutive theory for ${}_d\overline{\boldsymbol{\sigma}}$ that contains up to quadratic terms in $[\bar{D}]$. Following [1], we can write

$$ [{}_d\overline{\sigma}] = 2\eta[\bar{D}] + k(tr[\bar{D}])[I] + 4\eta_1[\bar{D}]^2 + 2\eta_3\left(tr[\bar{D}]^2\right)[I] \tag{3.5} $$

For incompressible fluid, $tr[\bar{D}] = 0$, hence equation (3.5) reduces to

$$ [{}_d\overline{\sigma}] = 2\eta[\bar{D}] + \eta_1[\bar{D}]^2 + \eta_3\left(tr[\bar{D}]^2\right)[I] \tag{3.6} $$

Equation (3.6) is the final form of the constitutive theory for ${}_d\overline{\boldsymbol{\sigma}}$ used in the present work.

3.3 Complete mathematical model, dimensionless form

3.3.1 Mathematical model in $\mathbb{R}^3$

For homogenous, isotropic, incompressible, viscous fluid, we have the following for continuity and momentum equations and constitutive theory for the isothermal conditions (in absence of body forces).

$$\overline{\boldsymbol{\nabla}} \cdot \bar{\boldsymbol{v}} = 0 \tag{3.7}$$

$$\overline{\rho} \frac{D\bar{\boldsymbol{v}}}{Dt} + \overline{\boldsymbol{\nabla}} \overline{p} - ({}_d\overline{\boldsymbol{\sigma}})^T \cdot \overline{\boldsymbol{\nabla}} = 0 \tag{3.8}$$

$${}_d\overline{\boldsymbol{\sigma}} = 2\eta \bar{\boldsymbol{D}} + \eta_1 (\bar{\boldsymbol{D}})^2 + \eta_3 \left(tr(\bar{\boldsymbol{D}})^2 \right) \boldsymbol{I} \tag{3.9}$$

We choose following reference quantities and dimensionless variables:

$$\begin{aligned} &\overline{x}_i = \frac{\hat{\bar{x}}_i}{L_0} \quad , \quad \overline{v}_i = \frac{\hat{\bar{v}}_i}{v_0} \quad , \quad \overline{\rho} = \frac{\hat{\bar{\rho}}}{\rho_0} \quad , \quad {}_d\overline{\sigma} = \frac{{}_d\hat{\bar{\sigma}}}{\tau_0}, \\ &\eta = \frac{\hat{\eta}}{\eta_0} \quad , \quad \underset{\sim}{\eta}_1 = \frac{\hat{\eta}_1}{\eta_0} \quad , \quad \underset{\sim}{\eta}_3 = \frac{\hat{\eta}_3}{\eta_0} \quad , \overline{p} = \frac{\hat{\bar{p}}}{p_0} \end{aligned} \tag{3.10}$$

First, we express equations (3.7) – (3.9) with hat (ˆ) implying that these have dimensions and then use equation (3.10) to obtain

$$\overline{\boldsymbol{\nabla}} \cdot \bar{\boldsymbol{v}} = 0 \tag{3.11}$$

$$\overline{\rho} \frac{D\bar{\boldsymbol{v}}}{Dt} + \frac{p_0}{\rho_0 {v_0}^2} \overline{\boldsymbol{\nabla}} \overline{p} - \frac{\tau_0}{\rho_0 {v_0}^2} ({}_d\overline{\boldsymbol{\sigma}})^T \cdot \overline{\boldsymbol{\nabla}} = 0 \tag{3.12}$$

$$[{}_d\overline{\sigma}] = \left(\frac{\eta_0 v_0}{\tau_0 L_0} \right) 2\eta [\bar{D}] + \left(\frac{\eta_0 {v_0}^2}{\tau_0 {L_0}^2} \right) \underset{\sim}{\eta}_1 ([\bar{D}])^2 + \underset{\sim}{\eta}_3 \left(\frac{\eta_0 {v_0}^2}{\tau_0 {L_0}^2} \right) \left(tr([\bar{D}])^2 \right) [I] \tag{3.13}$$

$$\begin{aligned} &\text{Using} \quad Re = \frac{\rho_0 v_0 L_0}{\eta_0} \quad \text{and} \quad \eta_{10} = \underset{\sim}{\eta}_1 \frac{v_0}{L_0} \quad \text{and} \quad \eta_{30} = \underset{\sim}{\eta}_3 \frac{v_0}{L_0} \\ &\text{and} \quad \tau_0 = p_0 = \rho_0 {v_0}^2, \quad \text{characteristic kinetic energy} \end{aligned} \tag{3.14}$$

We can write the following for equations (3.11) – (3.13):

$$\overline{\boldsymbol{\nabla}} \cdot \bar{\boldsymbol{v}} = 0 \tag{3.15}$$

$$\overline{\rho}\frac{D\overline{\boldsymbol{v}}}{Dt}+\overline{\boldsymbol{\nabla}}\overline{p}-({}_d\overline{\boldsymbol{\sigma}})^T\cdot\overline{\boldsymbol{\nabla}}=0 \tag{3.16}$$

$$[{}_d\overline{\sigma}]=\frac{2\eta}{Re}[\bar{D}]+\frac{\eta_{10}}{Re}([\bar{D}]^2)+\frac{\eta_{30}}{Re}\left(tr([\bar{D}]^2)\right)[I] \tag{3.17}$$

Equations (3.15) – (3.17) are the final dimensionless form of the dimensionless mathematical model.

Using equations (3.15) – (3.17), the mathematical model in $\mathbb{R}^2$ can be written as (defining $\eta_{10}=\eta_1$ and $2\eta_{30}=\eta_3$)

$$\frac{\partial\overline{u}}{\partial\overline{x}}+\frac{\partial\overline{v}}{\partial\overline{y}}=0 \tag{3.18}$$

$$\overline{\rho}\left(\overline{u}\frac{\partial\overline{u}}{\partial\overline{x}}+\overline{v}\frac{\partial\overline{u}}{\partial\overline{y}}\right)+\frac{\partial\overline{p}}{\partial\overline{x}}-\left(\frac{\partial({}_d\overline{\sigma}_{xx})}{\partial\overline{x}}+\frac{\partial({}_d\overline{\sigma}_{xy})}{\partial\overline{y}}\right)=0 \tag{3.19}$$

$$\overline{\rho}\left(\overline{u}\frac{\partial\overline{v}}{\partial\overline{x}}+\overline{v}\frac{\partial\overline{v}}{\partial\overline{y}}\right)+\frac{\partial\overline{p}}{\partial\overline{y}}-\left(\frac{\partial({}_d\overline{\sigma}_{xy})}{\partial\overline{x}}+\frac{\partial({}_d\overline{\sigma}_{yy})}{\partial\overline{y}}\right)=0 \tag{3.20}$$

$$\begin{aligned}{}_d\overline{\sigma}_{xx}=\frac{1}{Re}\Bigg[&\left(2\eta\frac{\partial\overline{u}}{\partial\overline{x}}\right)+\eta_1\left\{\left(\frac{\partial\overline{u}}{\partial\overline{x}}\right)^2+\frac{1}{4}\left(\frac{\partial\overline{u}}{\partial\overline{y}}+\frac{\partial\overline{v}}{\partial\overline{x}}\right)^2\right\}\\&+\eta_3\left\{\left(\frac{\partial\overline{u}}{\partial\overline{x}}\right)^2+\left(\frac{\partial\overline{v}}{\partial\overline{y}}\right)^2+\frac{1}{2}\left(\frac{\partial\overline{u}}{\partial\overline{y}}+\frac{\partial\overline{v}}{\partial\overline{x}}\right)^2\right\}\Bigg]\end{aligned} \tag{3.21}$$

$$\begin{aligned}{}_d\overline{\sigma}_{yy}=\frac{1}{Re}\Bigg[&\left(2\eta\frac{\partial\overline{v}}{\partial\overline{y}}\right)+\eta_1\left\{\left(\frac{\partial\overline{v}}{\partial\overline{y}}\right)^2+\frac{1}{4}\left(\frac{\partial\overline{u}}{\partial\overline{y}}+\frac{\partial\overline{v}}{\partial\overline{x}}\right)^2\right\}\\&+\eta_3\left\{\left(\frac{\partial\overline{u}}{\partial\overline{x}}\right)^2+\left(\frac{\partial\overline{v}}{\partial\overline{y}}\right)^2+\frac{1}{2}\left(\frac{\partial\overline{u}}{\partial\overline{y}}+\frac{\partial\overline{v}}{\partial\overline{x}}\right)^2\right\}\Bigg]\end{aligned} \tag{3.22}$$

$${}_d\overline{\sigma}_{xy}=\frac{\eta}{Re}\left(\frac{\partial\overline{v}}{\partial\overline{x}}+\frac{\partial\overline{u}}{\partial\overline{y}}\right) \tag{3.23}$$

This mathematical model is used for 'square lid driven cavity' (Model Problem-II) and 'asymmetric sudden expansion' (Model Problem-III).

3.3.2 Mathematical model for fully developed flow between parallel plates

Using $\overline{x}$ as the direction of flow, we can obtain the following mathematical models from equations (3.18) – (3.23). This mathematical model is used for Model Problem-I.

$$\frac{\partial \overline{p}}{\partial \overline{x}} - \frac{\partial ({}_d\overline{\sigma}_{xy})}{\partial \overline{y}} = 0 \tag{3.24}$$

$$\frac{\partial \overline{p}}{\partial \overline{y}} - \frac{\partial ({}_d\overline{\sigma}_{yy})}{\partial \overline{y}} = 0 \tag{3.25}$$

$${}_d\overline{\sigma}_{xx} = \frac{1}{Re}(\eta_1 + \eta_3)\left(\frac{\partial \overline{u}}{\partial \overline{y}}\right)^2 \tag{3.26}$$

$${}_d\overline{\sigma}_{yy} = \frac{1}{Re}(\eta_1 + \eta_3)\left(\frac{\partial \overline{u}}{\partial \overline{y}}\right)^2 \tag{3.27}$$

$${}_d\overline{\sigma}_{xy} = \frac{1}{Re}\left(\eta\frac{\partial \overline{u}}{\partial \overline{y}}\right)^2 \tag{3.28}$$

In equations (3.26) and (3.27), we have redefined the $2\eta_3 = \eta_3$.

A theoretical solution of equations (3.24) – (3.28) can be obtained for a fixed pressure gradient $\frac{\partial \overline{p}}{\partial \overline{x}}$.

Referring to figure 3.1, we can obtain

$${}_d\overline{\sigma}_{xy} = \left(\frac{\partial \overline{p}}{\partial \overline{x}}\right)\overline{y} \tag{3.29}$$

$$\overline{u} = Re\left(\frac{1}{2\eta}\frac{\partial \overline{p}}{\partial \overline{x}}\right)(\overline{y}^2 - \overline{H}^2) \tag{3.30}$$

Using equations (3.29), ${}_d\overline{\sigma}_{xx}$, ${}_d\overline{\sigma}_{yy}$ can be obtained using equations (3.26) and (3.27).

3.4 Model Problems

In this section, we consider 'fully developed flow between parallel plates', 'a square lid driven cavity' and 'an asymmetric sudden expansion' as model problems and present numerical solution for them using *p*-version finite element method with local approximations in higher order spaces.

3.4.1 Model Problem-I: Fully Developed Flow between Parallel Plates

Figure 3.1 shows a schematic and boundary conditions of the model problem. The plates are separated by a distance $2\overline{H}$. The origin of the $\overline{x}\overline{y}$-coordinate is located at the center of the plates and the positive $\bar{x}$-direction is the direction of the flow. The flow is pressure driven i.e. $\partial\overline{p}/\partial\bar{x}$ is specified and is constant.

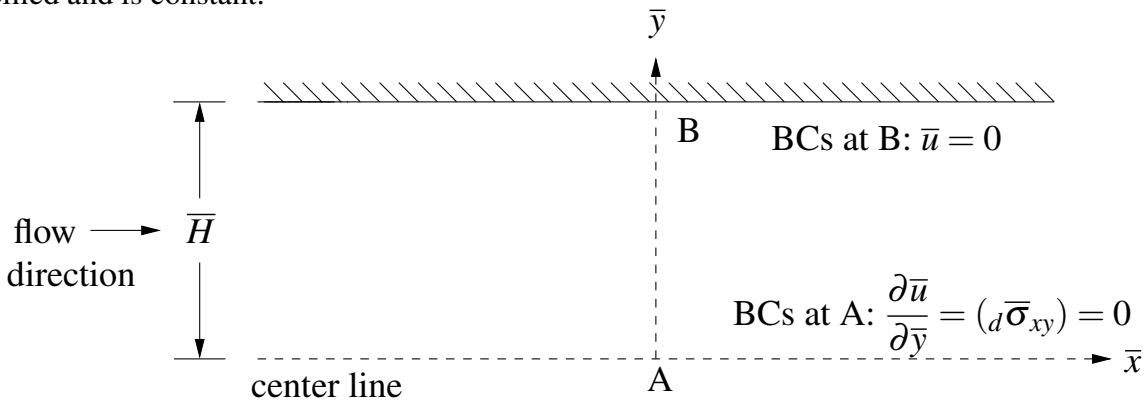

Figure 3.1: Schematic of 1-D fully developed flow between parallel plates (half domain)

The mathematical model and its theoretical solution is described in section 3.3.2. We consider following fluid properties and η_1, η_3 values:

$$\hat{\overline{\rho}} = \rho_0 = 998.2 \text{ kg/m}^3 \quad ; \quad \hat{\eta} = \eta_0 = 0.001002 \text{ Pa.s.}$$

$$\hat{\overline{H}} = L_0 = 0.015 \text{ m}, \quad u_0 = 0.0153247 \text{ m/s}, \quad \frac{\partial\overline{p}}{\partial\bar{x}} = -0.0133$$

$$\eta_1; \eta_3 \quad = \quad 0\% \text{ of } \eta, \quad 10\% \text{ of } \eta, \quad 12\% \text{ of } \eta, \quad 15\% \text{ of } \eta \quad \text{and} \quad 20\% \text{ of } \eta.$$

These give Re = 229.

When $\eta_1 = \eta_3 = 0\%$ of η, the behavior is Newtonian with ${}_d\overline{\sigma}_{xx} = 0$ and ${}_d\overline{\sigma}_{yy} = 0$ and linear ${}_d\overline{\sigma}_{xy}$ (figure 3.3). Velocity profile remains unaffected by the choices of η_1 and η_3. (figure 3.2). From the mathematical model (section 3.3.2), we note that for this model problem, ${}_d\overline{\sigma}_{xx} = {}_d\,\overline{\sigma}_{yy}$ when $\eta_1 \neq 0$ and $\eta_3 \neq 0$. Furthermore we obtain the same ${}_d\overline{\sigma}_{xx}$ and ${}_d\overline{\sigma}_{yy}$ for same values of η_1 and η_3. The results in figures 3.2 – 3.4 are obtained using the theoretical solution. We note that due to non-linear constitutive theory, the velocity field is not affected, hence the standard shear stress due to $[\bar{D}]$ remains unaffected in the non-linear constitutive theory for ${}_d\overline{\boldsymbol{\sigma}}$. Newton's law of viscosity yields ${}_d\overline{\sigma}_{xx} = {}_d\overline{\sigma}_{yy} = 0$, hence pure shear flow. The constitutive theory used here

clearly shows the presence of normal stresses ${}_d\overline{\sigma}_{xx} = {}_d\overline{\sigma}_{yy}$. The magnitude of these depend upon the value of the material coefficients η_1 and η_3. The values used in the studies presented here are chosen to be a fraction of the viscosity η. Since the dimensionless η is 1, the value listed in the graphs can be viewed as dimensionless values of 0.0, 0.1, 0.12, 0.15 and 0.2 for η_1 and η_3. Based on the constitutive theory used here, the normal stresses are always non-zero and are equal in magnitude but these values are not strictly quantifiable as the material coefficients η_1 and η_3 need to be determined experimentally.

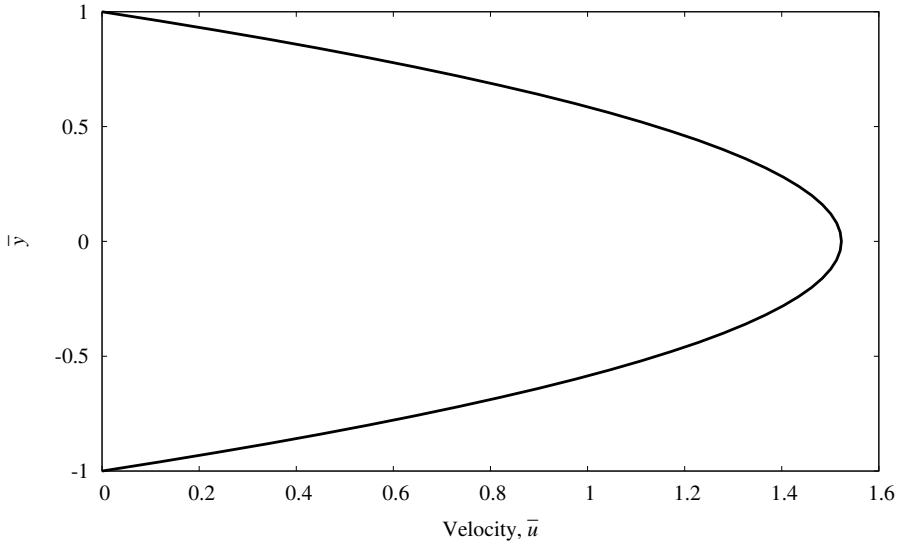

Figure 3.2: Velocity $\overline{u}$ versus $\overline{y}$ for different values of η_1 and/or η_3

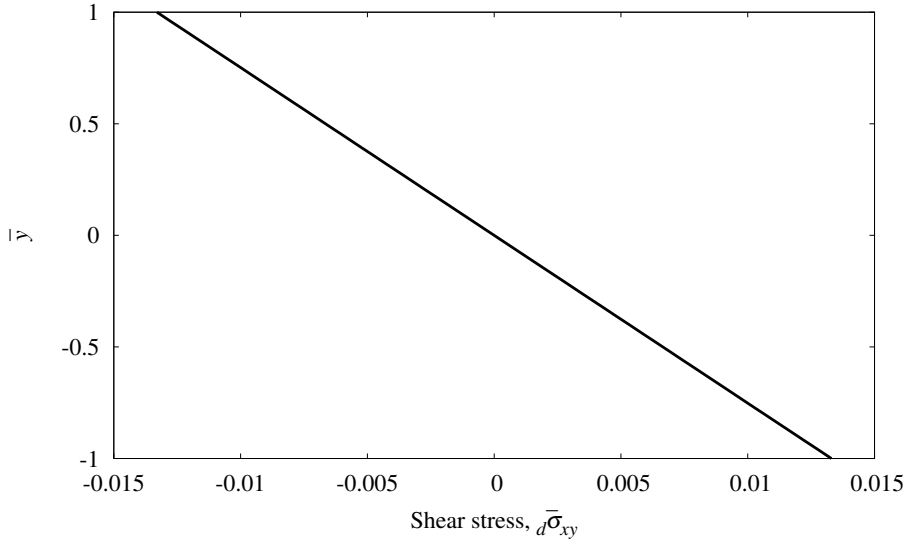

Figure 3.3: Shear stress ${}_d\overline{\sigma}_{xy}$ versus $\overline{y}$ for different values of η_1 and/or η_3

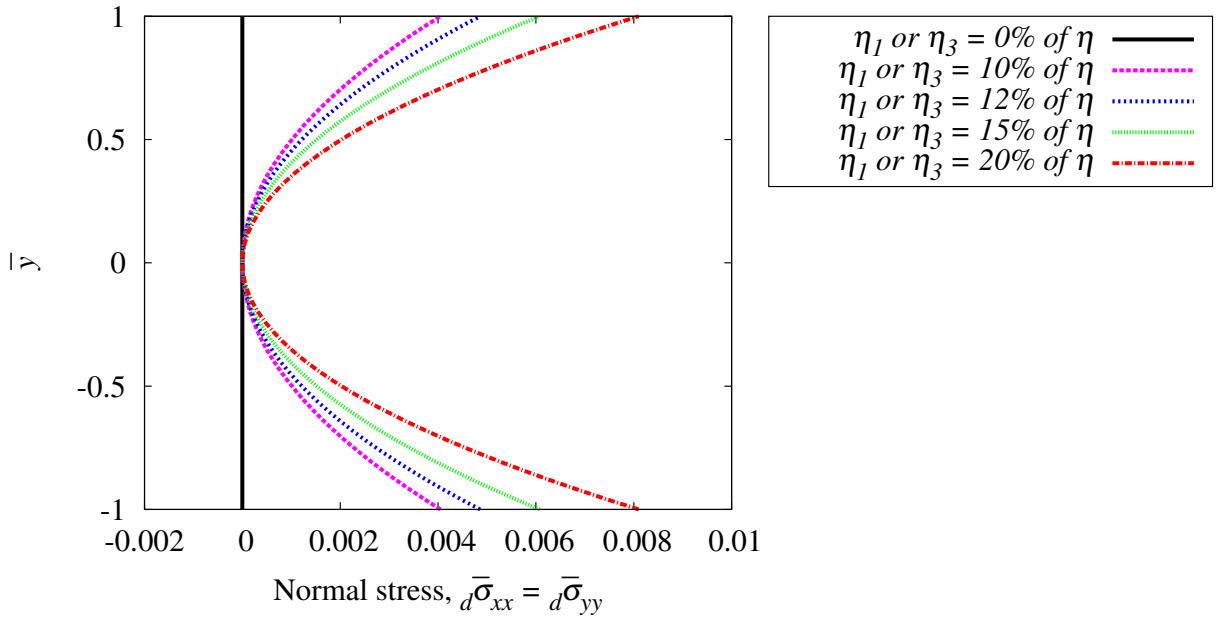

Figure 3.4: Normal stress ${}_d\overline{\sigma}_{xx}$ (or ${}_d\overline{\sigma}_{yy}$) versus $\bar{y}$ for different values of η_1 or η_3

3.4.2 Model Problem-II: A square lid driven cavity

Figure 3.5(a) and (b) show the schematic of the square lid driven cavity and boundary conditions. The length $\overline{h}_d$ determines the sharpness of the rise in velocity from zero at the vertical walls to the constant value of $\overline{u} = 1$ at the lid. Figure 3.6 shows two graded discretizations consisting of 196 and 256 p-version elements with $\overline{h}_d$ values of 0.005 and 0.0025. [14]

We consider the following fluid properties, constant reference quantities and the values of η_1 and η_3.

$$\hat{\overline{\rho}} = 868 \text{ kg/m}^3 \quad ; \quad \hat{\eta} = 3 \text{ Pa.s.}$$

$$\hat{\overline{\rho}} = \rho_0, \quad \hat{\eta} = \eta_0, \quad u_0 = 69.124 \text{ m/s}$$

$$\hat{\overline{H}} = L_0 = 0.05 \text{ m}$$

$$\eta_1; \eta_3 = 0\% \text{ of } \eta, \quad 10\% \text{ of } \eta, \quad 12\% \text{ of } \eta, \quad 15\% \text{ of } \eta \quad \text{and} \quad 20\% \text{ of } \eta.$$

These yield a one unit square cavity with Re = 1000.

Numerical solutions are calculated using $k = 2$ and $p = 7$ with local approximations in $H^{k,p}(\bar{\Omega}^e)$

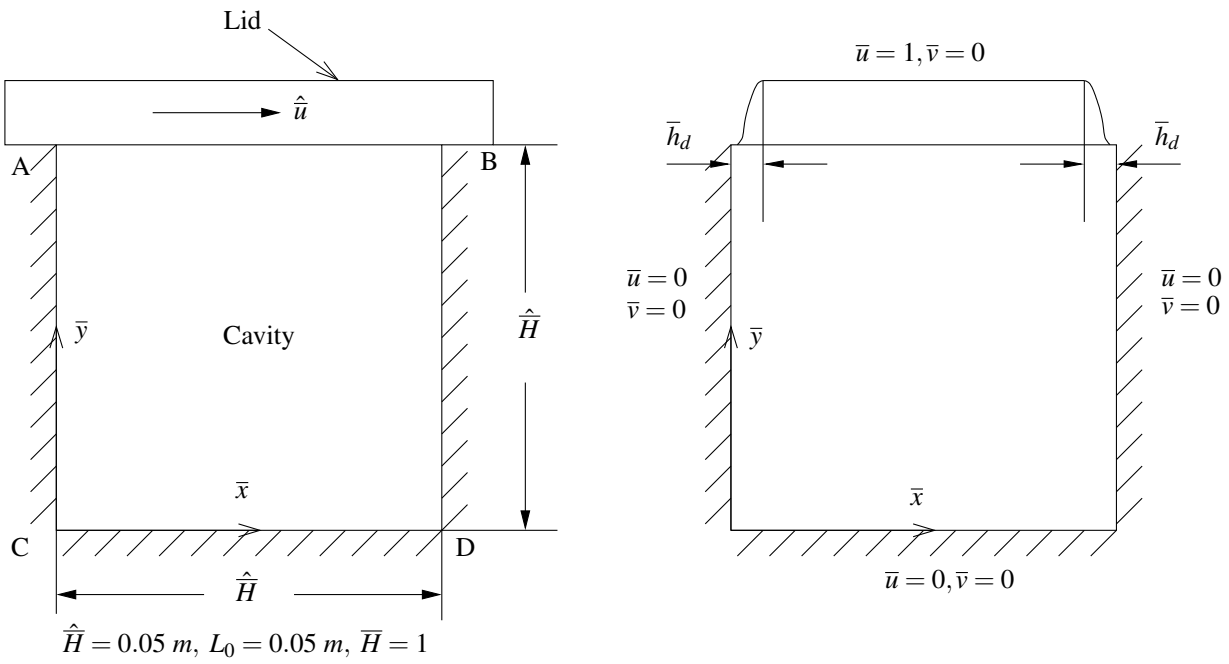

(a) Schematic of Lid Driven Cavity

(b) Idealization of Lid Driven Cavity in (a), computational domain and boundary conditions.

Figure 3.5: Schematic representation and computational domain for the lid driven square cavity

Side	Element lengths						
$\overrightarrow{CA}$	0.005	0.01	0.02	0.04	0.08	0.1725	0.1725
	0.1725	0.1725	0.08	0.04	0.02	0.01	0.005
$\overrightarrow{CD}$	0.005	0.01	0.02	0.04	0.08	0.1725	0.1725
	0.1725	0.1725	0.08	0.04	0.02	0.01	0.005

(a) A 196 element discretization : mesh M1 ; $\overline{h}_d = 0.005$

Side	Element lengths						
$\overrightarrow{CA}$	0.0025	0.005	0.01	0.02	0.04	0.08	0.16
	0.1825	0.1825	0.16	0.08	0.04	0.02	0.01
	0.005	0.0025					
$\overrightarrow{CD}$	0.0025	0.005	0.01	0.02	0.04	0.08	0.16
	0.1825	0.1825	0.16	0.08	0.04	0.02	0.01
	0.005	0.0025					

(b) A 256 element discretization : mesh M2 ; $\overline{h}_d = 0.0025$

Figure 3.6: Two discretizations used for the lid driven square cavity

spaces for which I values of the order of $O(10^{-4})$ are achieved, which are in good agreement with the published results [15]. Solutions with mesh M2 yield lower values of I compared to those with mesh M1, confirming better accuracy of solutions. Hence, we have presented our numerical studies using mesh M2 in this work.

The normal stress results are best illustrated if we consider the following:

$$ {}_d\overline{\sigma}_{xx} = ({}_d\overline{\sigma}_{xx})_l + ({}_d\overline{\sigma}_{xx})_{nl} \tag{3.31} $$

$$ {}_d\overline{\sigma}_{yy} = ({}_d\overline{\sigma}_{yy})_l + ({}_d\overline{\sigma}_{yy})_{nl} \tag{3.32} $$

in which

$$ ({}_d\overline{\sigma}_{xx})_l = \frac{2\eta}{Re}\left(\frac{\partial\overline{u}}{\partial\overline{x}}\right) \tag{3.33} $$

$$ ({}_d\overline{\sigma}_{yy})_l = \frac{2\eta}{Re}\left(\frac{\partial\overline{v}}{\partial\overline{y}}\right) \tag{3.34} $$

and

$$ \begin{aligned} ({}_d\overline{\sigma}_{xx})_{nl} = \frac{1}{Re}\Bigg[\eta_1\left\{\left(\frac{\partial\overline{u}}{\partial\overline{x}}\right)^2 + \frac{1}{4}\left(\frac{\partial\overline{u}}{\partial\overline{y}} + \frac{\partial\overline{v}}{\partial\overline{x}}\right)^2\right\} \\ + \eta_3\left\{\left(\frac{\partial\overline{u}}{\partial\overline{x}}\right)^2 + \left(\frac{\partial\overline{v}}{\partial\overline{y}}\right)^2 + \frac{1}{2}\left(\frac{\partial\overline{u}}{\partial\overline{y}} + \frac{\partial\overline{v}}{\partial\overline{x}}\right)^2\right\}\Bigg] \end{aligned} \tag{3.35} $$

$$ \begin{aligned} ({}_d\overline{\sigma}_{yy})_{nl} = \frac{1}{Re}\Bigg[\eta_1\left\{\left(\frac{\partial\overline{v}}{\partial\overline{y}}\right)^2 + \frac{1}{4}\left(\frac{\partial\overline{u}}{\partial\overline{y}} + \frac{\partial\overline{v}}{\partial\overline{x}}\right)^2\right\} \\ + \eta_3\left\{\left(\frac{\partial\overline{u}}{\partial\overline{x}}\right)^2 + \left(\frac{\partial\overline{v}}{\partial\overline{y}}\right)^2 + \frac{1}{2}\left(\frac{\partial\overline{u}}{\partial\overline{y}} + \frac{\partial\overline{v}}{\partial\overline{x}}\right)^2\right\}\Bigg] \end{aligned} \tag{3.36} $$

In case of standard Newton's law of viscosity in which $[{}_d\overline{\sigma}_{xx}] = 2\eta[\bar{D}]$, $({}_d\overline{\sigma}_{xx})_l$ and $({}_d\overline{\sigma}_{yy})_l$ are non-zero but $({}_d\overline{\sigma}_{xx})_{nl}$ and $({}_d\overline{\sigma}_{yy})_{nl}$ are zero. Furthermore, $({}_d\overline{\sigma}_{xx})_l$ and $({}_d\overline{\sigma}_{yy})_l$ are not affected by non-zero values of η_1 and η_3, hence the decomposition in equations (3.31) and (3.32) is beneficial to study the quantitative contribution of $[\bar{D}]^2$ in the constitutive theory for $[{}_d\overline{\sigma}]$. We also note that coefficient of η_3 in $({}_d\overline{\sigma}_{xx})_{nl}$ and $({}_d\overline{\sigma}_{yy})_{nl}$ is same and if we use $\dfrac{\partial\overline{u}}{\partial\overline{x}} = -\dfrac{\partial\overline{v}}{\partial\overline{y}}$ (from continuity), then the coefficient of η_1 term is also same in $({}_d\overline{\sigma}_{xx})_{nl}$ and $({}_d\overline{\sigma}_{yy})_{nl}$. That is $({}_d\overline{\sigma}_{xx})_{nl} = ({}_d\overline{\sigma}_{yy})_{nl}$ holds for different fluids so that coefficients of η_1 and η_3 can be determined.

We can observe that the velocity field is unaffected by non-zero values of η_1 and η_3, since the pressure field remains uniform throughout the fluid because the non-linear terms of the normal stresses are identical when substituted in the momentum equations and the momentum equations show that the shear stress gradients remain same for non-zero values of η_1 and η_3. The normal stresses and hence, the pressure gradients remain same throughout the cavity except in the vicinity of the lid of cavity and near the right boundary of cavity for the non-zero values of η_1 and η_3.

Figure 3.7 show the streamline contours for the square cavity, that remain the same regardless of the η_1 and η_3 values. Solution is smooth with clearly defined recirculation zones at the bottom corners of the cavity. We observe sharp drop in the velocity u values as we move away from the lid.

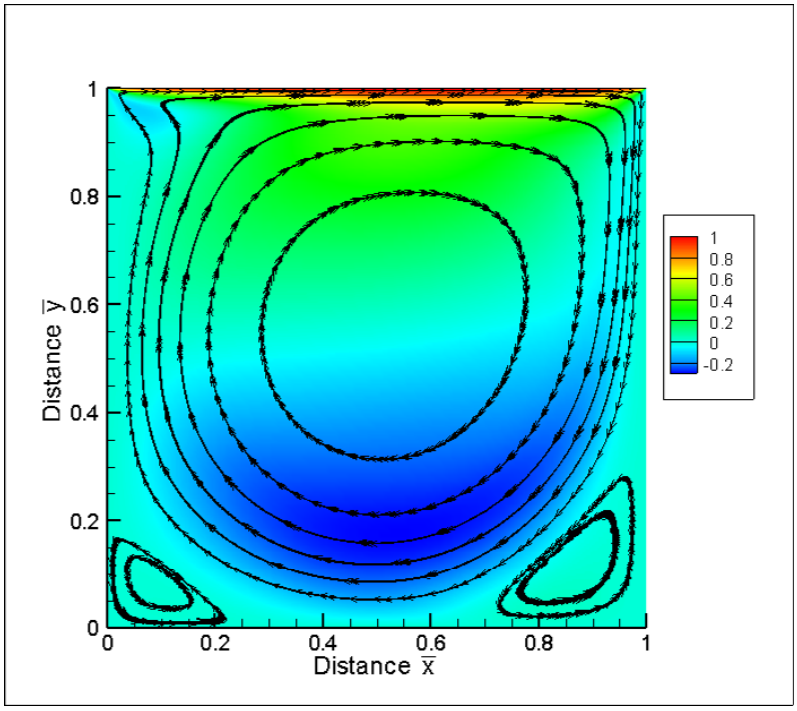

Figure 3.7: Contours of streamlines in the lid driven square cavity for different values of η_1 and η_3

Figures 3.8(a) and (b) show plots of velocities $\bar{u}$ *and* $\bar{v}$ versus $\bar{y}$ at $\bar{x} = 0.5$. Graphs of $\bar{u}$ *and* $\bar{v}$ versus $\bar{x}$ at $\bar{y} = 0.5$ are shown in figures 3.8(c) and (d). These are invariants of η_1 and η_3. Plots of ${}_d\bar{\sigma}_{xy}$ versus $\bar{y}$ at $\bar{x} = 0.5$ and ${}_d\bar{\sigma}_{xy}$ versus $\bar{x}$ at $\bar{y} = 0.5$ are shown in figures 3.9(a) and (b). These are also independent of η_1 and η_3.

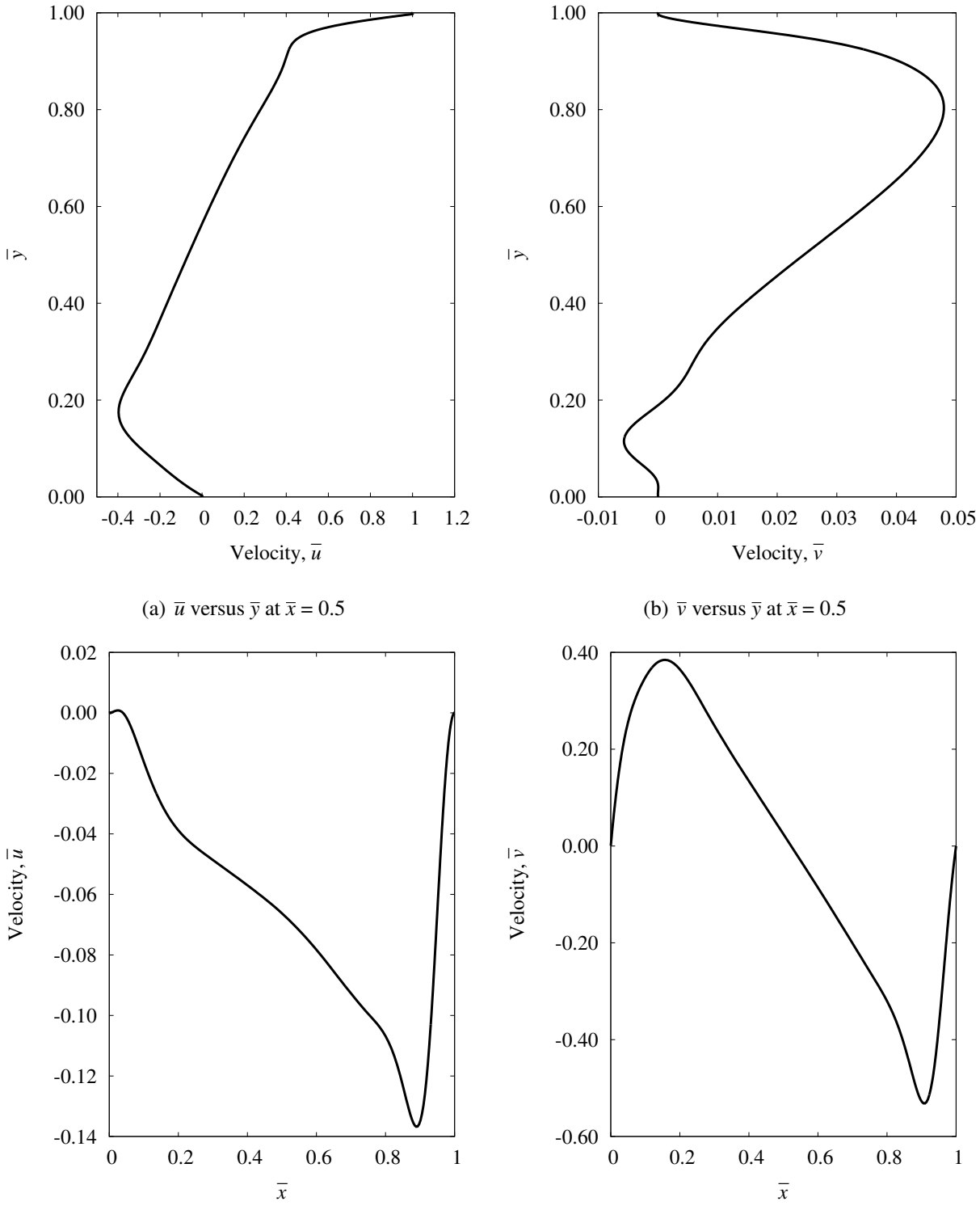

(a) $\overline{u}$ versus $\overline{y}$ at $\overline{x} = 0.5$

(b) $\overline{v}$ versus $\overline{y}$ at $\overline{x} = 0.5$

(c) $\overline{u}$ versus $\overline{x}$ at $\overline{y} = 0.5$

(d) $\overline{v}$ versus $\overline{x}$ at $\overline{y} = 0.5$

Figure 3.8: Velocities $\overline{u}$, $\overline{v}$ versus $\overline{y}$ at $\overline{x} = 0.5$ and velocities $\overline{u}$, $\overline{v}$ versus $\overline{x}$ at $\overline{y} = 0.5$ for different values of η_1 and/or η_3

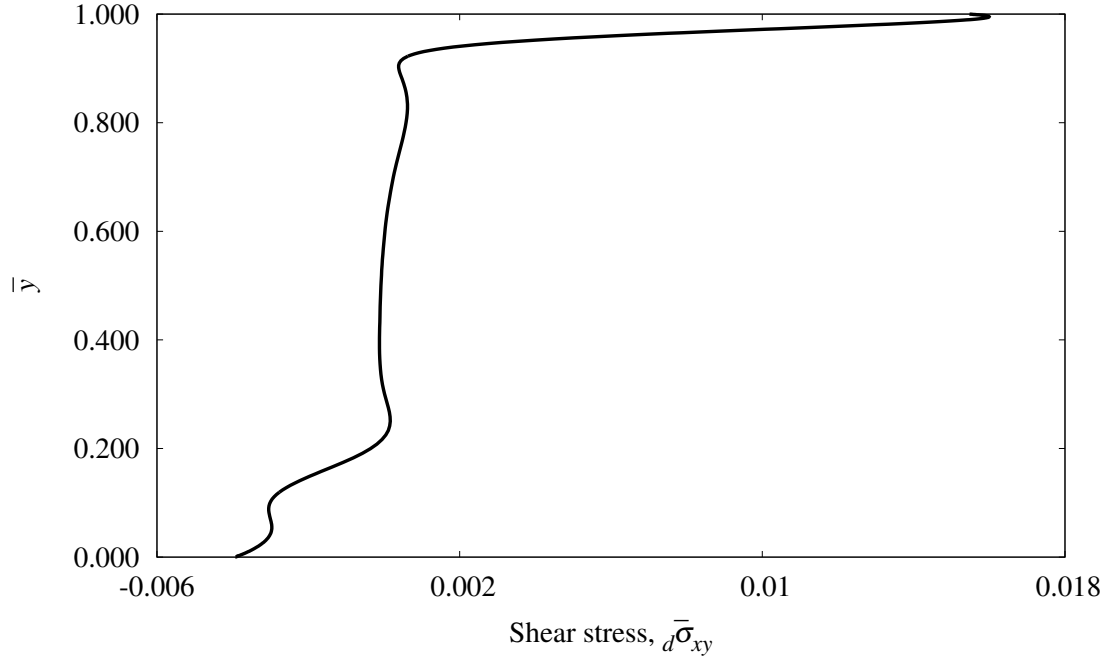

(a) ${}_d\overline{\sigma}_{xy}$ versus $\overline{y}$ at $\overline{x} = 0.5$

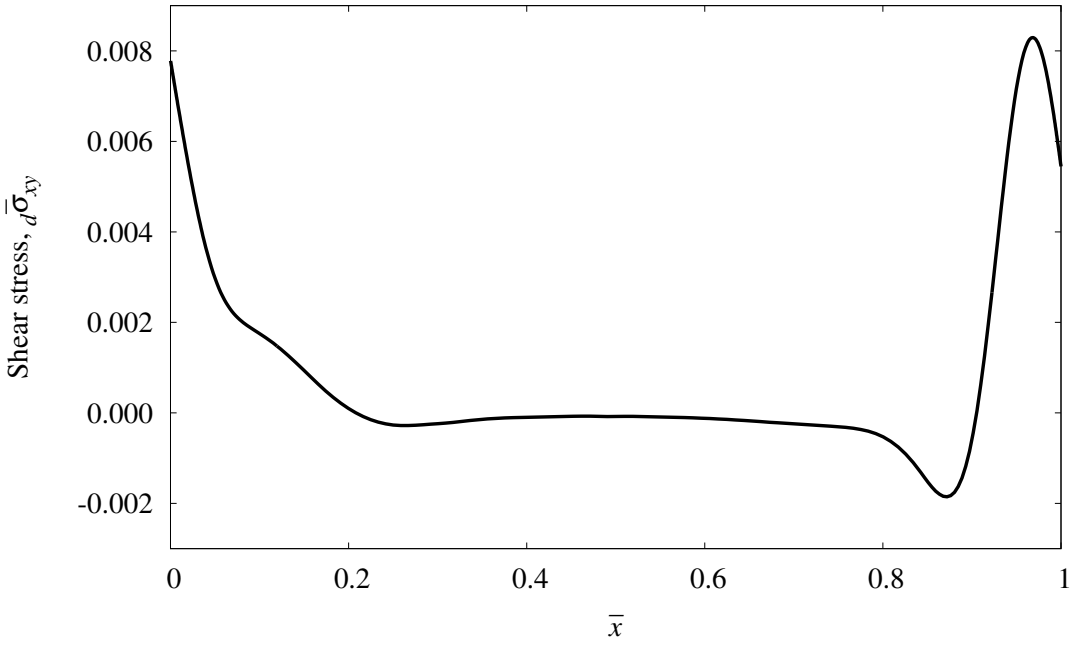

(b) ${}_d\overline{\sigma}_{xy}$ versus $\overline{x}$ at $\overline{y} = 0.5$

Figure 3.9: Shear stress ${}_d\overline{\sigma}_{xy}$ versus $\overline{y}$ at $\overline{x} = 0.5$ and shear stress ${}_d\overline{\sigma}_{xy}$ versus $\overline{x}$ at $\overline{y} = 0.5$ for different values of η_1 and/or η_3

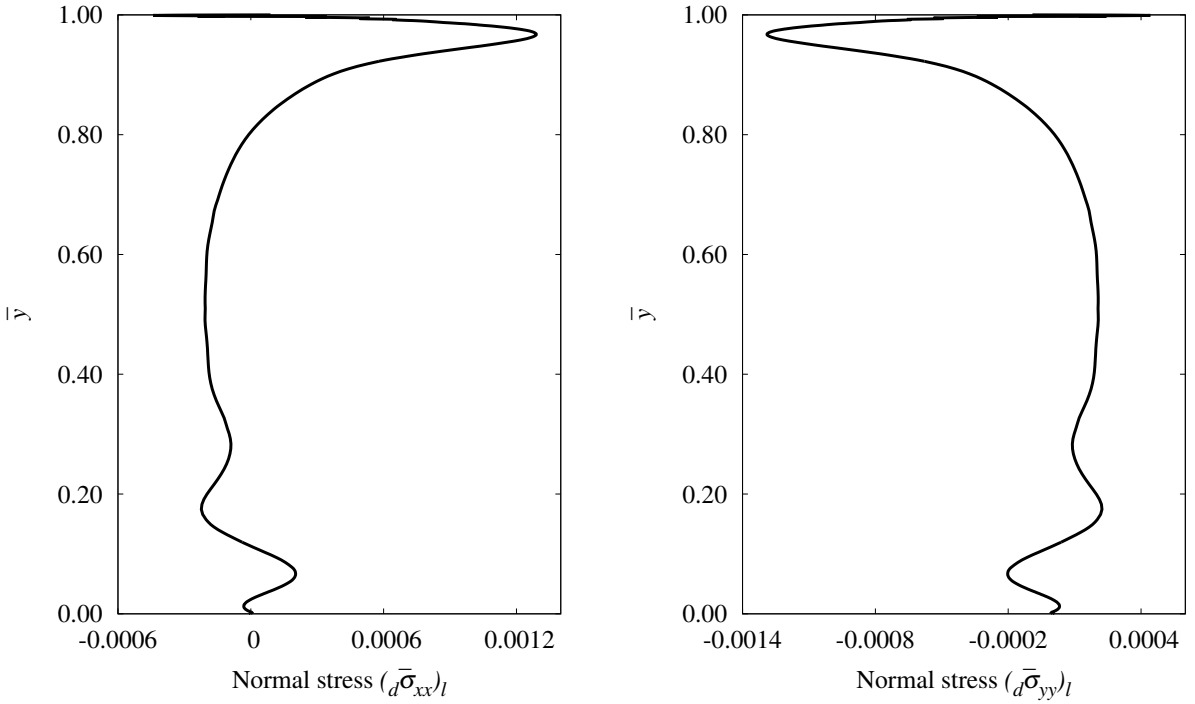

(a) $({}_d\overline{\sigma}_{xx})_l$ versus $\bar{y}$ at $\bar{x} = 0.5$

(b) $({}_d\overline{\sigma}_{yy})_l$ versus $\bar{y}$ at $\bar{x} = 0.5$

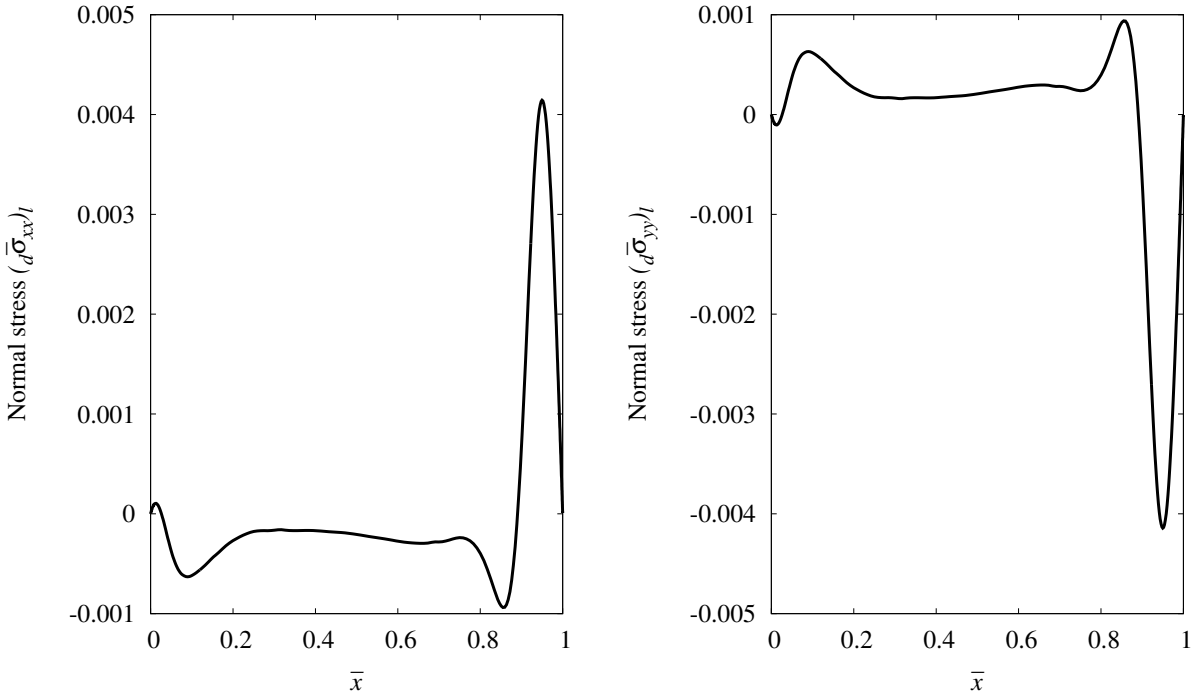

(c) $({}_d\overline{\sigma}_{xx})_l$ versus $\bar{x}$ at $\bar{y} = 0.5$

(d) $({}_d\overline{\sigma}_{yy})_l$ versus $\bar{x}$ at $\bar{y} = 0.5$

Figure 3.10: Normal stresses $({}_d\overline{\sigma}_{xx})_l$ and $({}_d\overline{\sigma}_{yy})_l$ versus $\bar{y}$ at $\bar{x} = 0.5$ and $({}_d\overline{\sigma}_{xx})_l$ and $({}_d\overline{\sigma}_{yy})_l$ versus distance $\bar{x}$ at $\bar{y} = 0.5$ for $\eta_1 = \eta_3 = 0$

First, we consider $({}_d\overline{\sigma}_{xx})_l$ and $({}_d\overline{\sigma}_{yy})_l$ shown in figures 3.10 (a) and (b) as a function of $\overline{y}$ for $\overline{x}$ = 0.5 and in figures 3.10 (c) and (d) as a function of $\overline{x}$ for $\overline{y}$ = 0.5. These are obviously independent of the choices of η_1 and η_3. Stresses $({}_d\overline{\sigma}_{xx})_l$ and $({}_d\overline{\sigma}_{yy})_l$ are same in magnitude but opposite in sign expected.

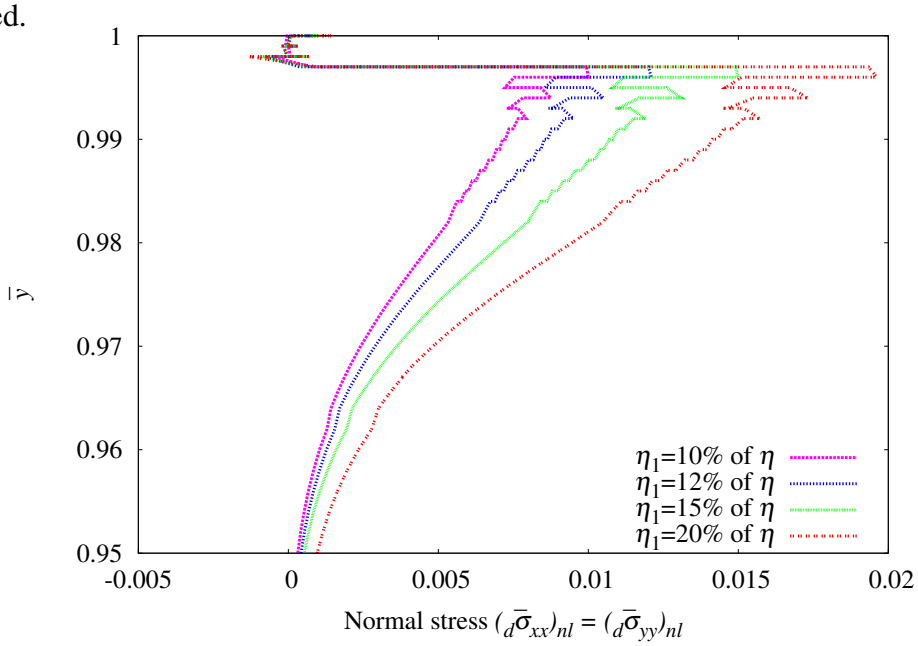

Figure 3.11: Normal stresses $({}_d\overline{\sigma}_{xx})_{nl}$ or $({}_d\overline{\sigma}_{yy})_{nl}$ versus $\overline{y}$ at $\overline{x}$ = 0.5 (exploded view) for different values of η_1 (η_3 = 0)

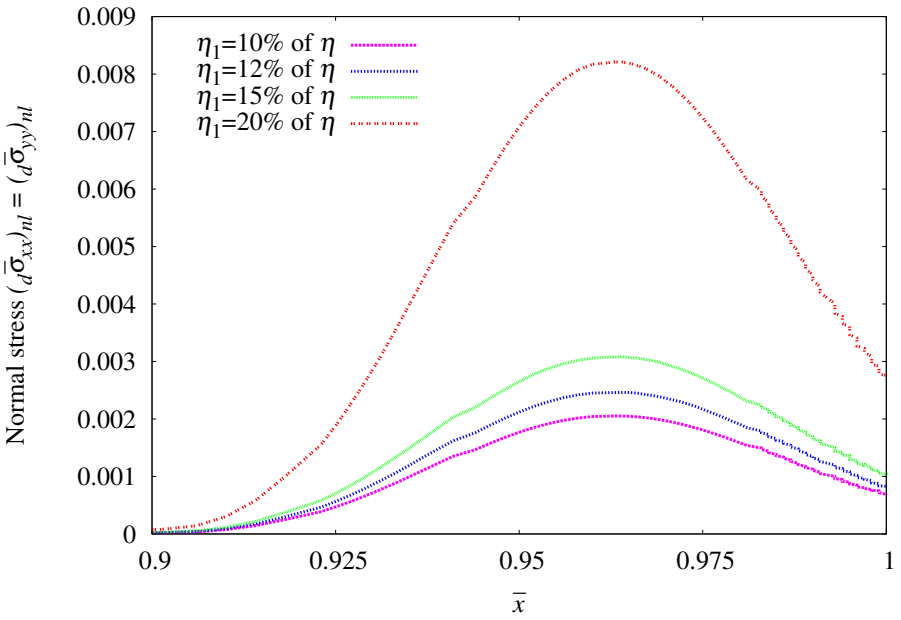

Figure 3.12: Normal stresses $({}_d\overline{\sigma}_{xx})_{nl}$ or $({}_d\overline{\sigma}_{yy})_{nl}$ versus distance $\overline{x}$ at $\overline{y}$ = 0.5 (exploded view) for different values of η_1 (η_3 = 0)

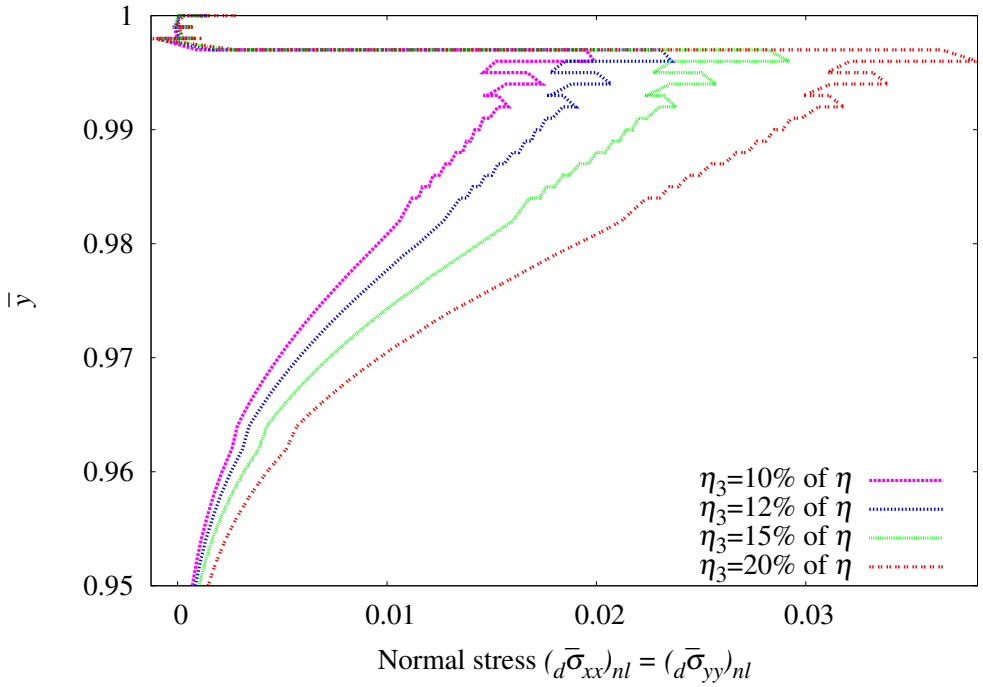

Figure 3.13: Normal stresses $({}_d\overline{\sigma}_{xx})_{nl}$ or $({}_d\overline{\sigma}_{yy})_{nl}$ versus $\bar{y}$ at $\bar{x} = 0.5$ (exploded view) for different values of η_3 ($\eta_1 = 0$)

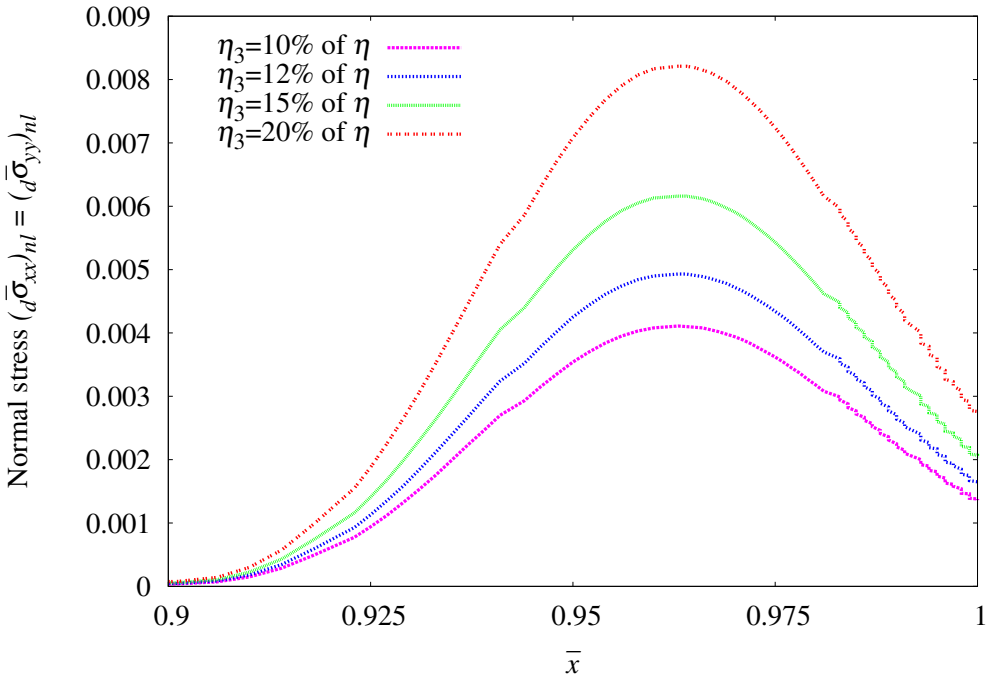

Figure 3.14: Normal stresses $({}_d\overline{\sigma}_{xx})_{nl}$ or $({}_d\overline{\sigma}_{yy})_{nl}$ versus distance $\bar{x}$ at $\bar{y} = 0.5$ (exploded view) for different values of η_3 ($\eta_1 = 0$)

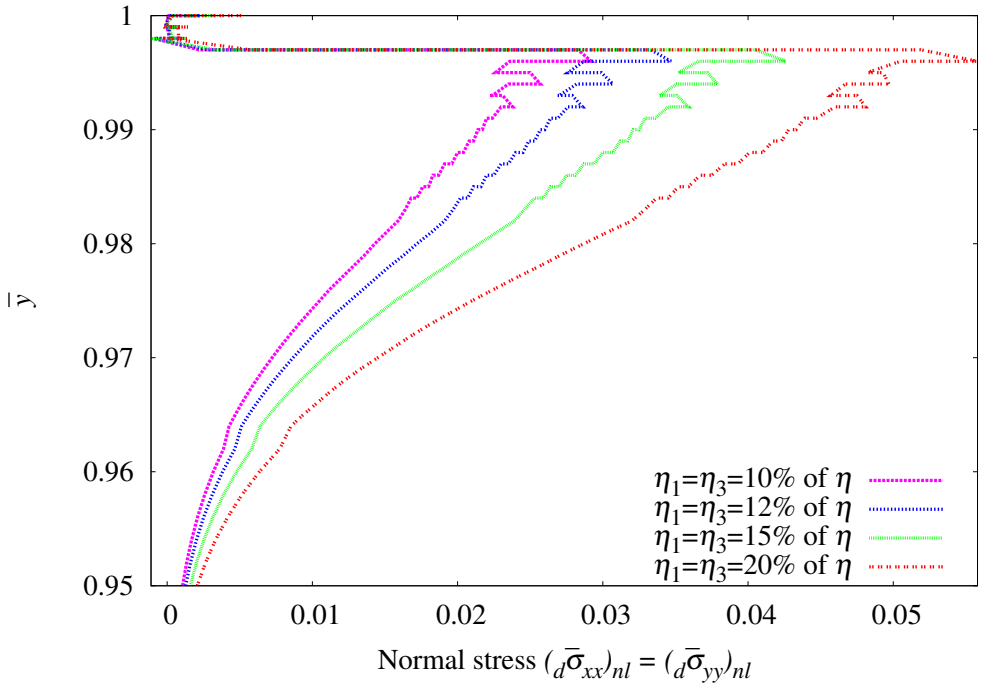

Figure 3.15: Normal stresses $({}_d\overline{\sigma}_{xx})_{nl}$ or $({}_d\overline{\sigma}_{yy})_{nl}$ versus $\bar{y}$ at $\bar{x} = 0.5$ (exploded view) for different values of η_1 and η_3

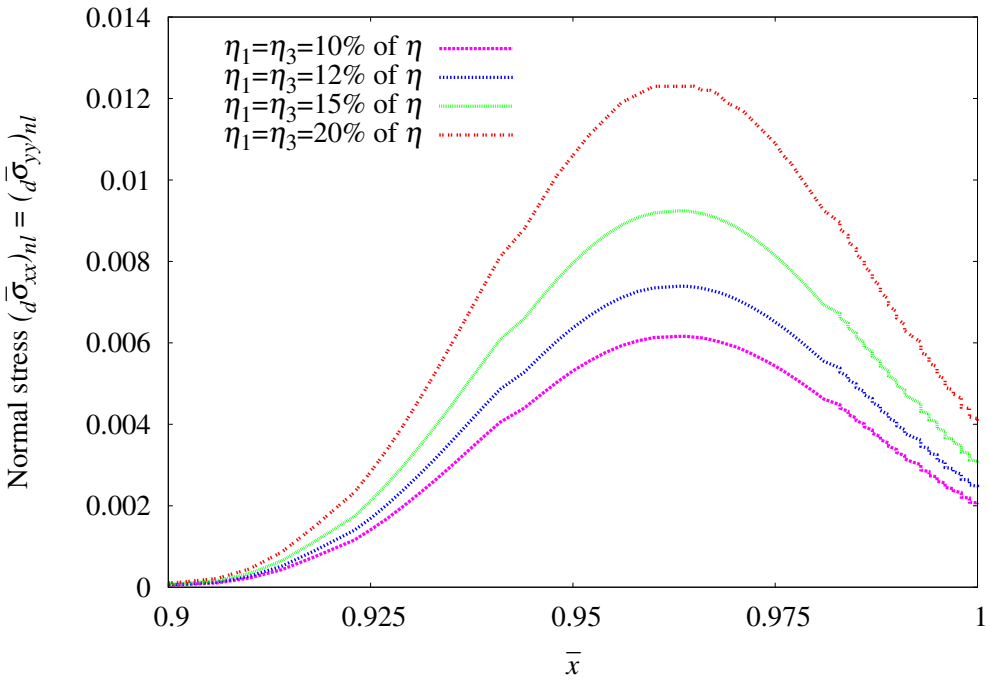

Figure 3.16: Normal stresses $({}_d\overline{\sigma}_{xx})_{nl}$ or $({}_d\overline{\sigma}_{yy})_{nl}$ versus distance $\bar{x}$ at $\bar{y} = 0.5$ (exploded view) for different values of η_1 and η_3

Figures 3.11 – 3.12 show plots of $({}_d\overline{\sigma}_{xx})_{nl} = ({}_d\overline{\sigma}_{yy})_{nl}$ versus $\overline{y}$ at $\overline{x} = 0.5$ and $({}_d\overline{\sigma}_{xx})_{nl} = ({}_d\overline{\sigma}_{yy})_{nl}$ versus $\overline{x}$ at $\overline{y} = 0.5$ for different values of η_1. Graphs of same quantities at the same location for different values of η_3 are shown in figures 3.13 – 3.14.

Figures 3.15 – 3.16 show graphs of same stress at same locations for different choices of $\eta_1 = \eta_3$. In all cases, these normal stress values are significant compared to $({}_d\overline{\sigma}_{xx})_l$ and $({}_d\overline{\sigma}_{yy})_l$ even for low range of the values of $\eta_1 = \eta_3$. Confirming that $[\bar{D}]^2$ term in the constitutive theory for $[{}_d\overline{\sigma}]$ is worthy of consideration in the calibration of the model.

Plots of mechanical pressure $\overline{p}$ versus $\overline{y}$ at $\overline{x} = 0.5$ and $\overline{p}$ versus $\overline{x}$ at $\overline{y} = 0.5$ for different values of η_1 but $\eta_3 = 0$, different values of η_3 but $\eta_1 = 0$ and for different values of $\eta_1 = \eta_3$ are compared with those for different values of $\eta_1 = \eta_3 = 0$ and shown in figures 3.17 - 3.22. We observe increase in $\overline{p}$ with progressively increasing values of η_1, η_3 and $\eta_1 = \eta_3$.

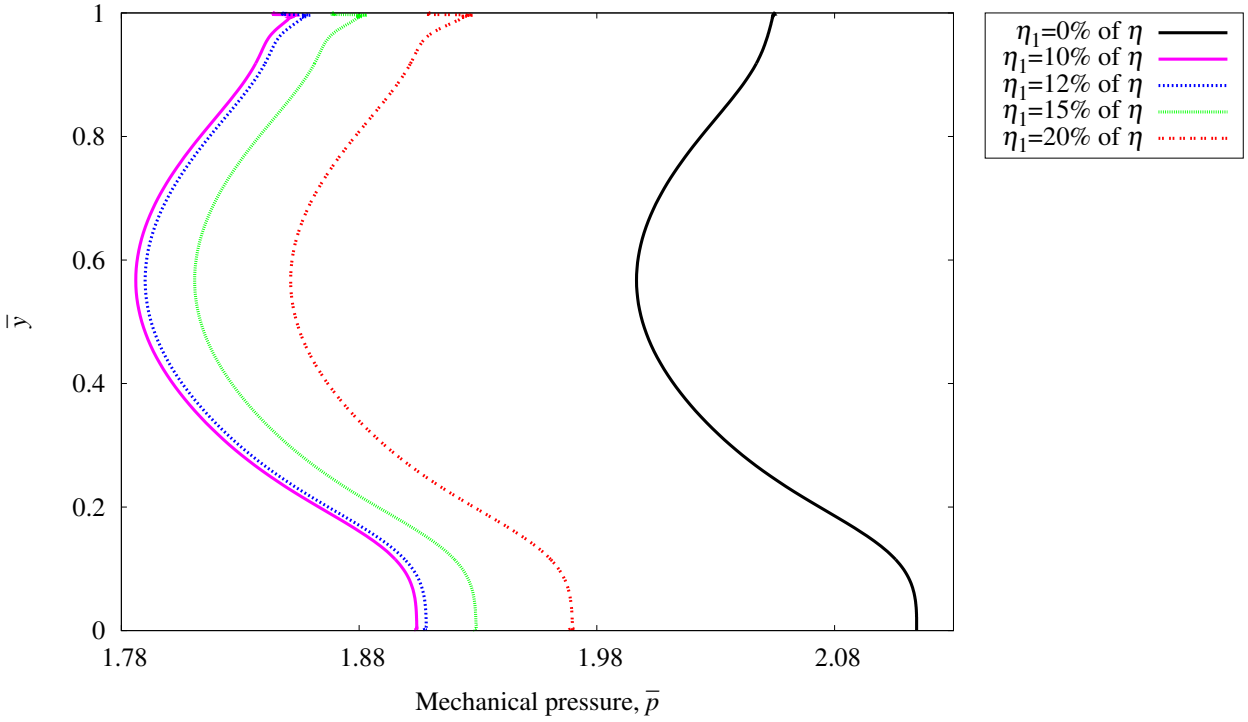

Figure 3.17: Mechanical pressure $\overline{p}$ versus $\overline{y}$ at $\overline{x} = 0.5$ for different values of η_1 ($\eta_3 = 0$)

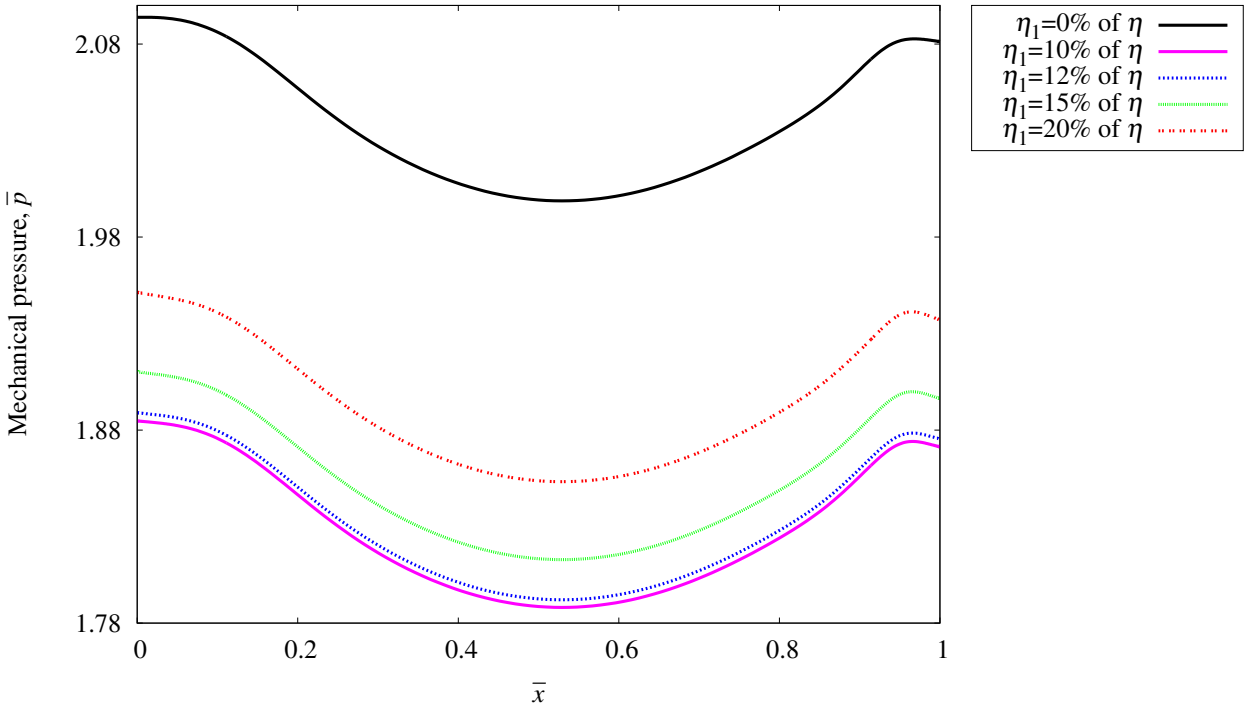

Figure 3.18: Mechanical pressure $\overline{p}$ versus $\overline{x}$ at $\overline{y} = 0.5$ for different values of η_1 ($\eta_3 = 0$)

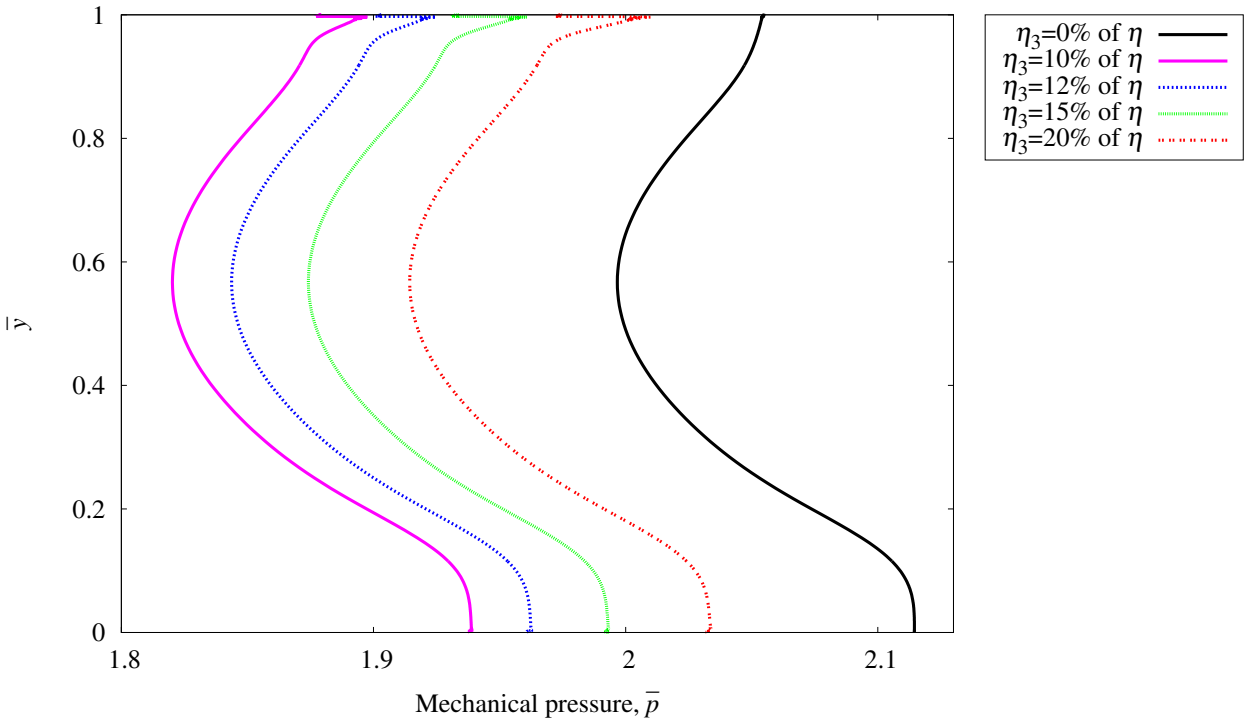

Figure 3.19: Mechanical pressure $\overline{p}$ versus $\overline{y}$ at $\overline{x} = 0.5$ for different values of η_3 ($\eta_1 = 0$)

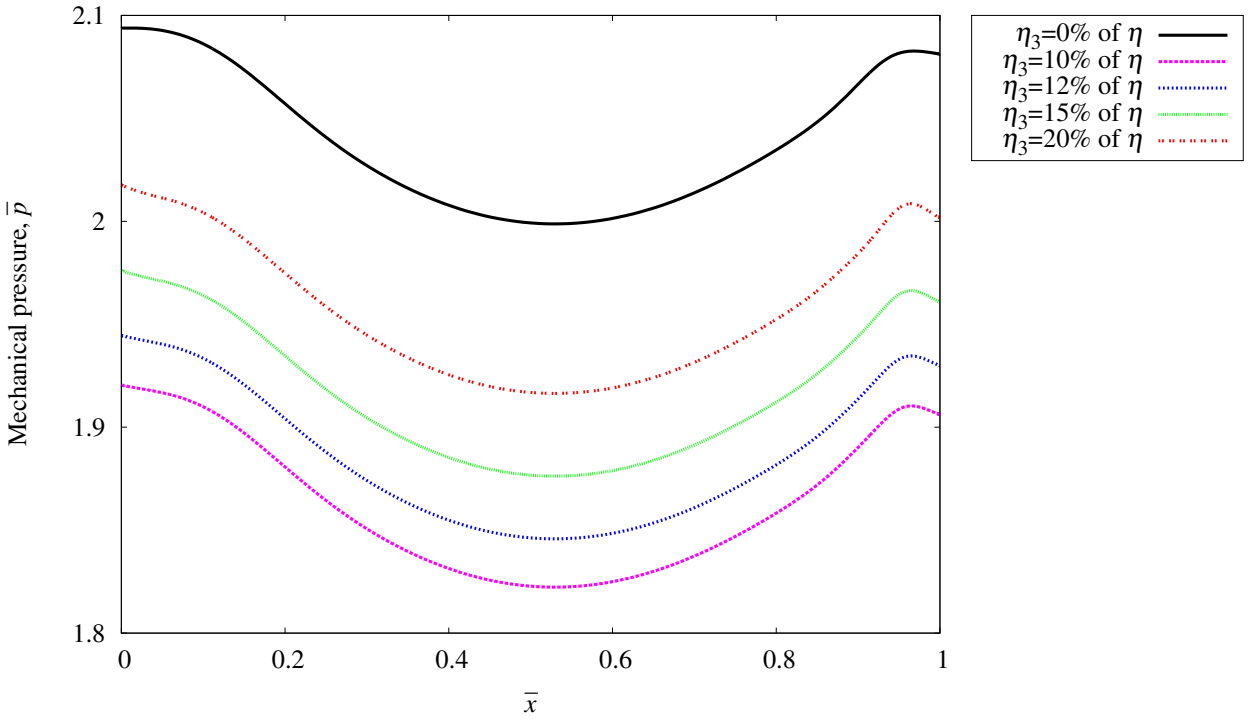

Figure 3.20: Mechanical pressure $\overline{p}$ versus $\overline{x}$ at $\overline{y} = 0.5$ for different values of η_3 ($\eta_1 = 0$)

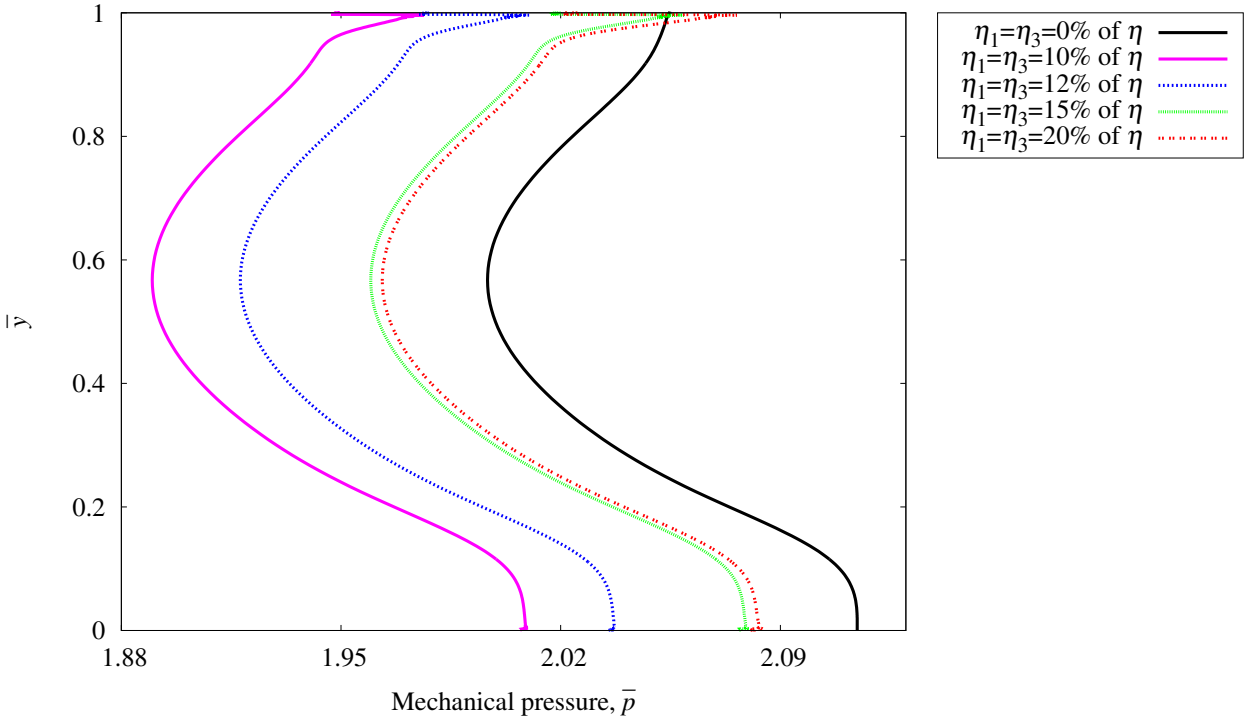

Figure 3.21: Mechanical pressure $\overline{p}$ versus $\overline{y}$ at $\overline{x} = 0.5$ for different values of η_1 and η_3

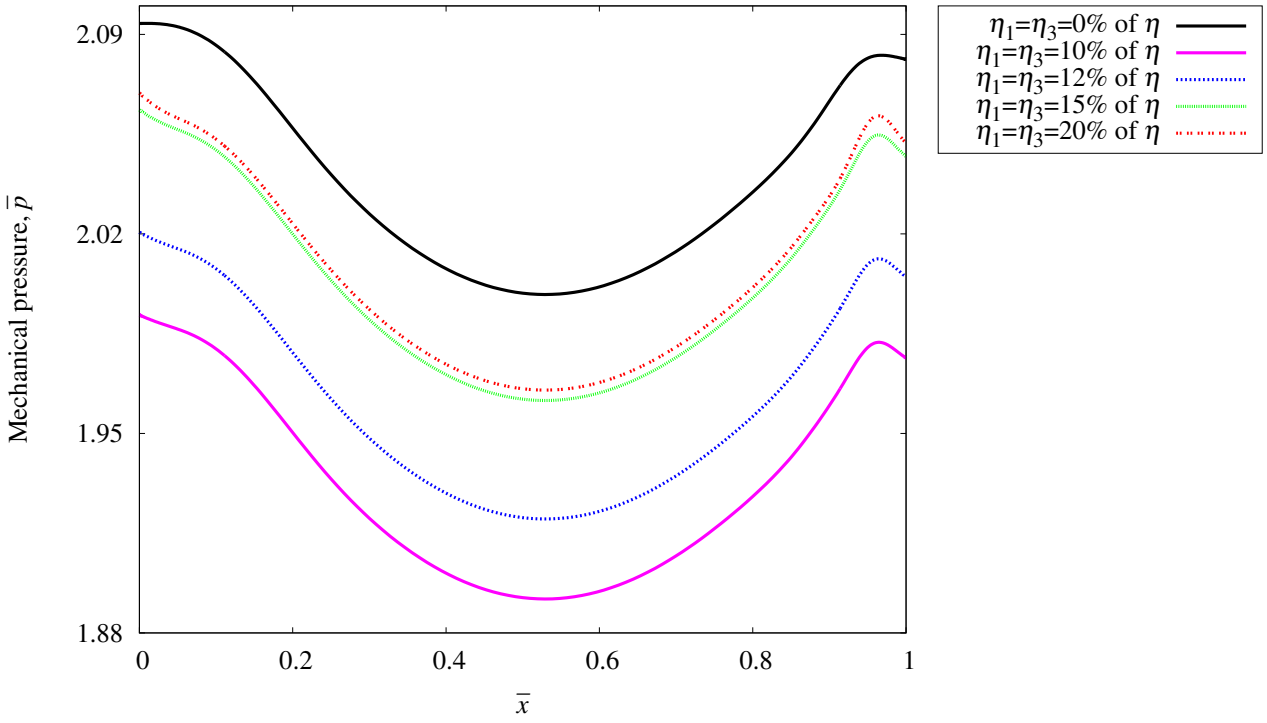

Figure 3.22: Mechanical pressure $\overline{p}$ versus $\overline{x}$ at $\overline{y} = 0.5$ for different values of η_1 and η_3

Plots of mechanical pressure gradient $\frac{\partial \overline{p}}{\partial \overline{x}}$ versus $\overline{y}$ at $\overline{x} = 0.5$ and $\overline{p}$ versus $\overline{x}$ at $\overline{y} = 0.5$ for different values of η_1 but $\eta_3 = 0$, different values of η_3 but $\eta_1 = 0$ and for different values of $\eta_1 = \eta_3$ are compared with those for different values of $\eta_1 = \eta_3 = 0$ and shown in figures 3.23 - 3.28.

Similarly, graphs for mechanical pressure gradient $\frac{\partial \overline{p}}{\partial \overline{y}}$ at same locations are shown in figures 3.29 - 3.34. The pressure gradients are observed to remain constant for non-zero values of η_1 and η_3, except in the vicinity of the lid of the cavity and near the right boundary of the cavity, hence the exploded views are shown here.

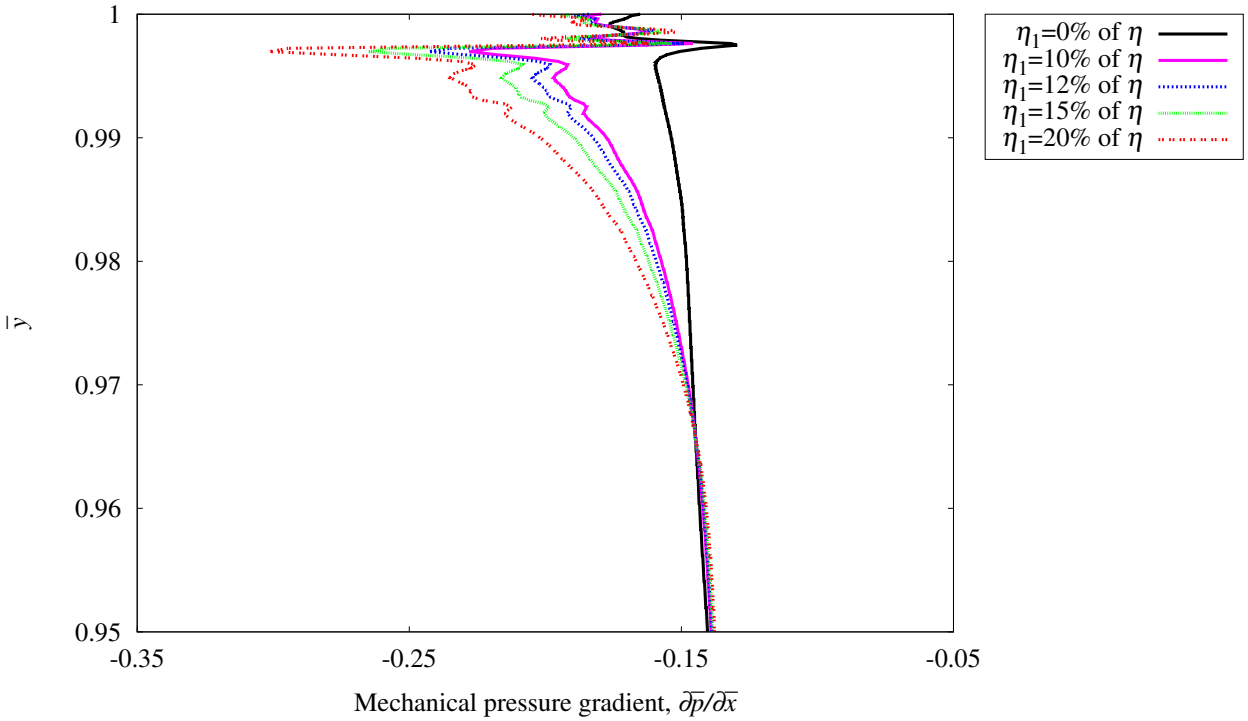

Figure 3.23: Mechanical pressure gradient $\frac{\partial \bar{p}}{\partial \bar{x}}$ versus $\bar{y}$ at $\bar{x} = 0.5$ (exploded view) for different values of η_1 ($\eta_3 = 0$)

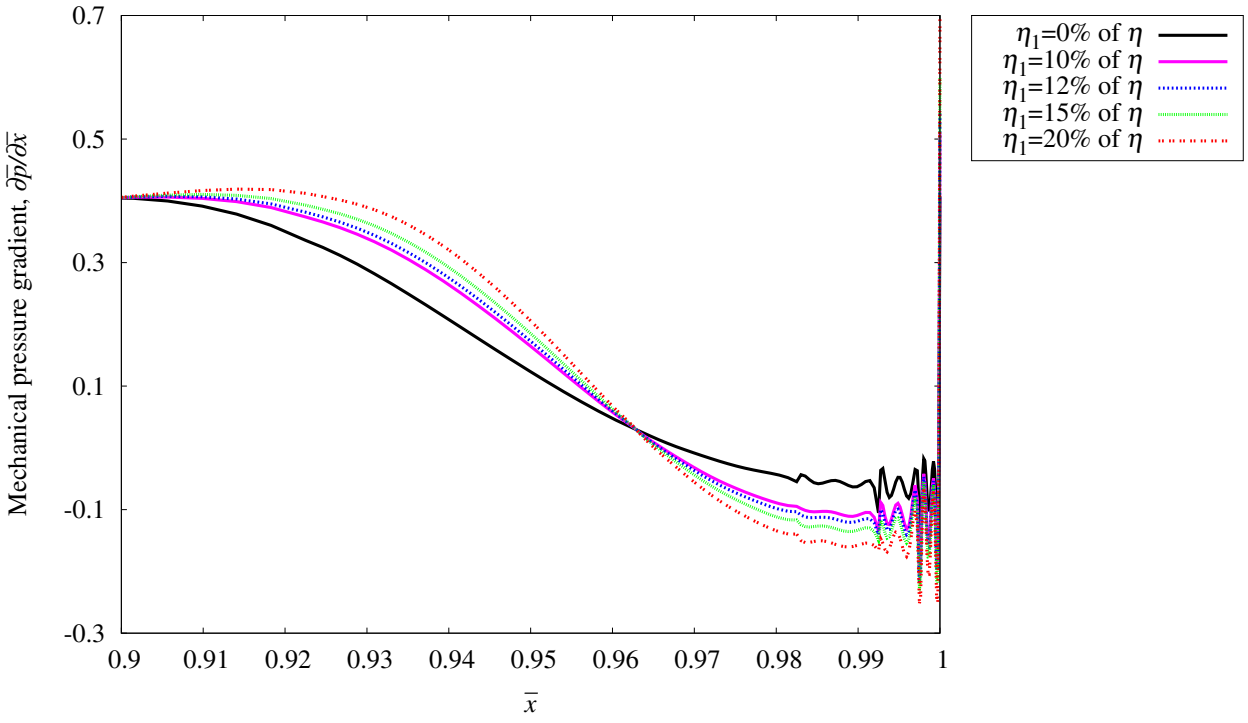

Figure 3.24: Mechanical pressure gradient $\frac{\partial \bar{p}}{\partial \bar{x}}$ versus $\bar{x}$ at $\bar{y} = 0.5$ (exploded view) for different values of η_1 ($\eta_3 = 0$)

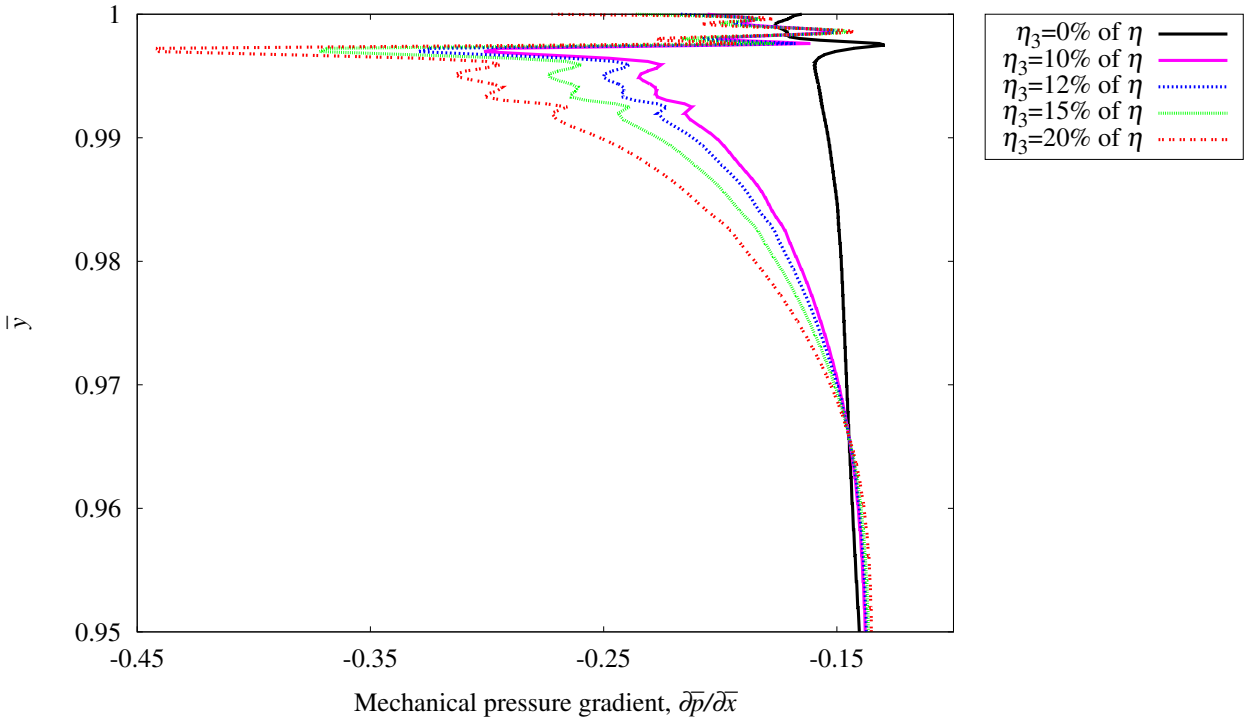

Figure 3.25: Mechanical pressure gradient $\frac{\partial \bar{p}}{\partial \bar{x}}$ versus $\bar{y}$ at $\bar{x} = 0.5$ (exploded view) for different values of η_3 ($\eta_1 = 0$)

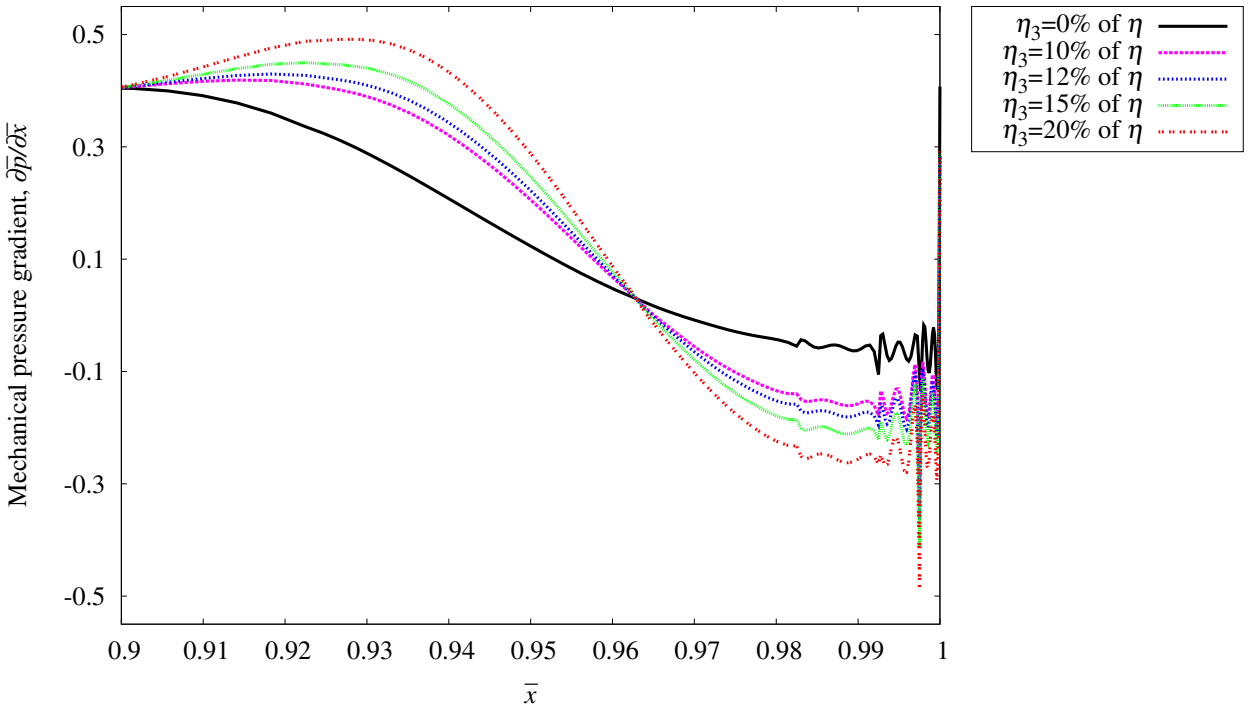

Figure 3.26: Mechanical pressure gradient $\frac{\partial \bar{p}}{\partial \bar{x}}$ versus $\bar{x}$ at $\bar{y} = 0.5$ (exploded view) for different values of η_3 ($\eta_1 = 0$)

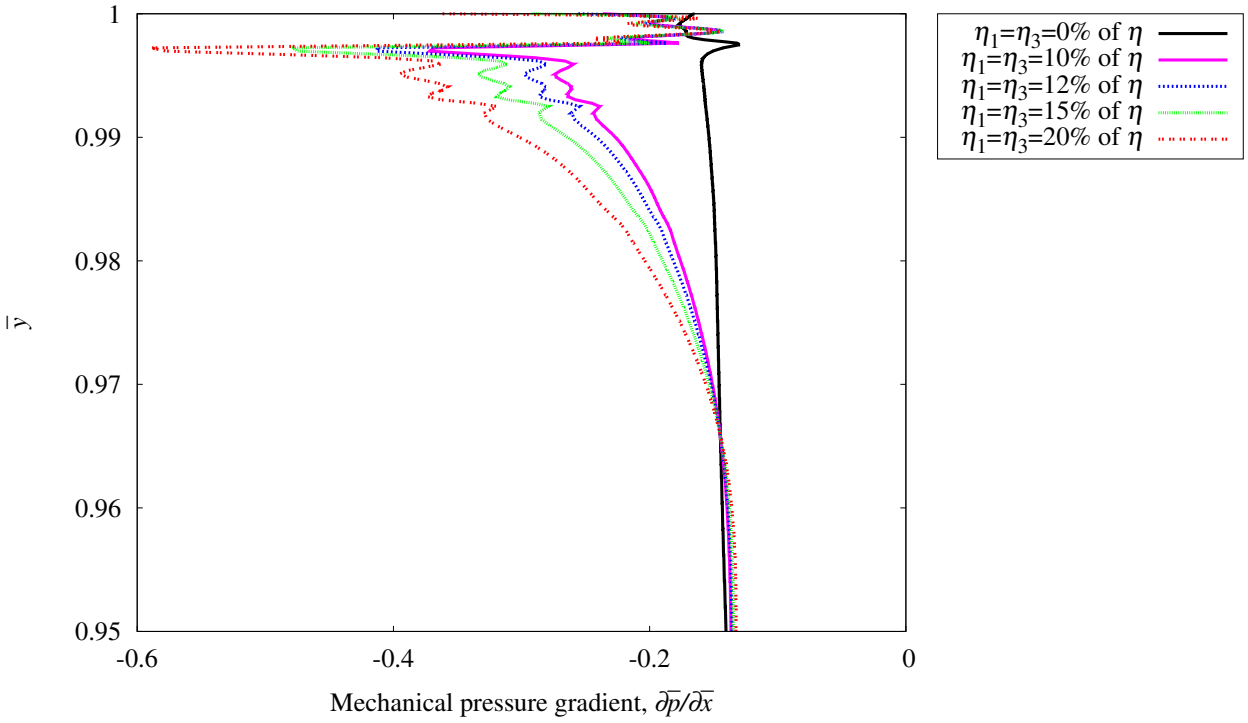

Figure 3.27: Mechanical pressure gradient $\frac{\partial\bar{p}}{\partial\bar{x}}$ versus $\bar{y}$ at $\bar{x} = 0.5$ (exploded view) for different values of η_1 and η_3

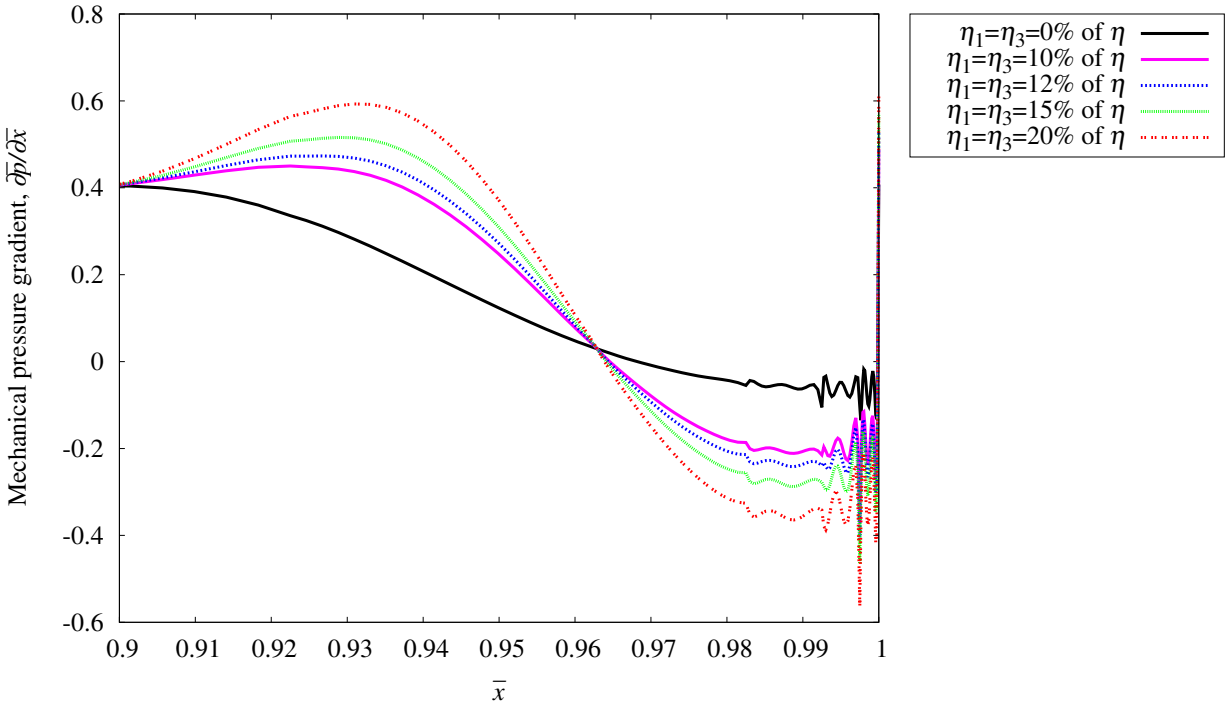

Figure 3.28: Mechanical pressure gradient $\frac{\partial\bar{p}}{\partial\bar{x}}$ versus $\bar{x}$ at $\bar{y} = 0.5$ (exploded view) for different values of η_1 and η_3

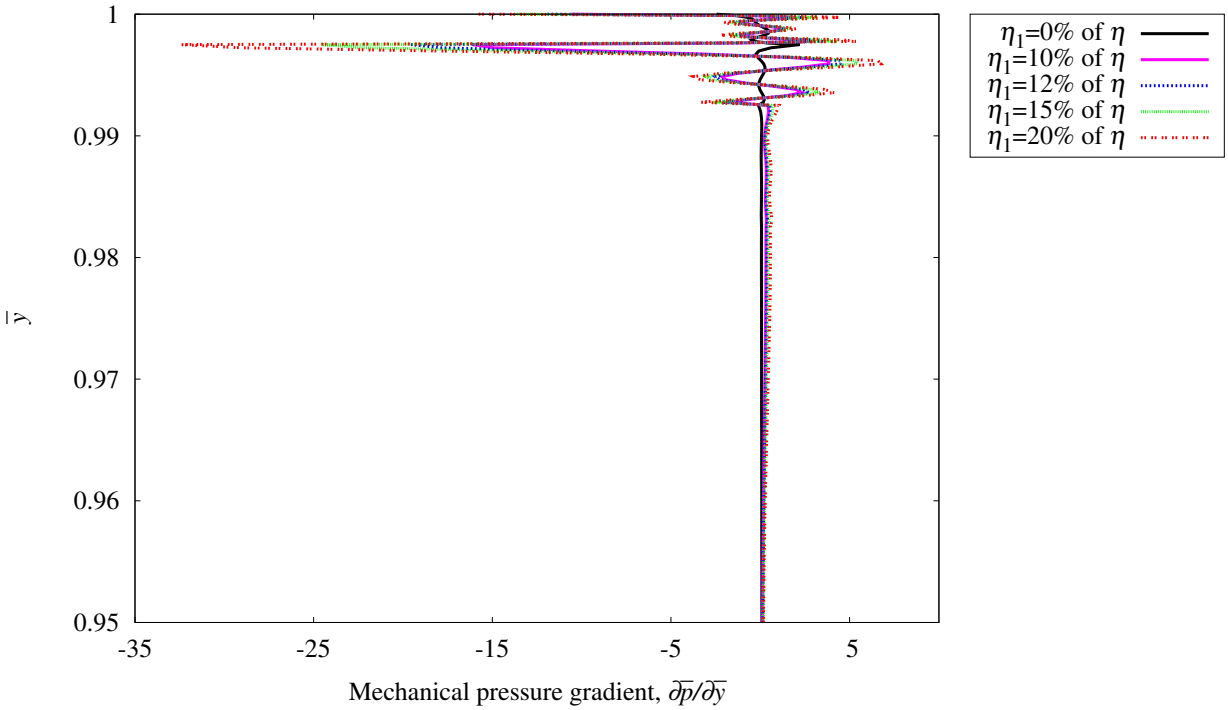

Figure 3.29: Mechanical pressure gradient $\frac{\partial\bar{p}}{\partial\bar{y}}$ versus $\bar{y}$ at $\bar{x} = 0.5$ (exploded view) for different values of η_1 ($\eta_3 = 0$)

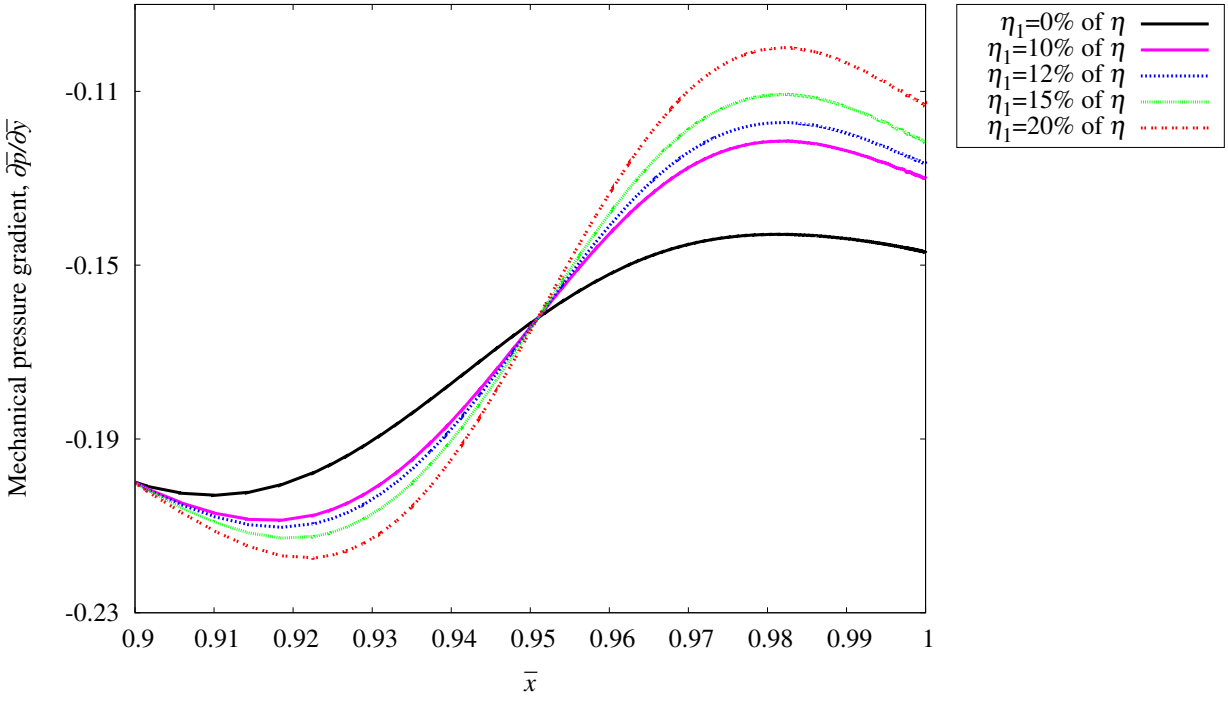

Figure 3.30: Mechanical pressure gradient $\frac{\partial\bar{p}}{\partial\bar{y}}$ versus $\bar{x}$ at $\bar{y} = 0.5$ (exploded view) for different values of η_1 ($\eta_3 = 0$)

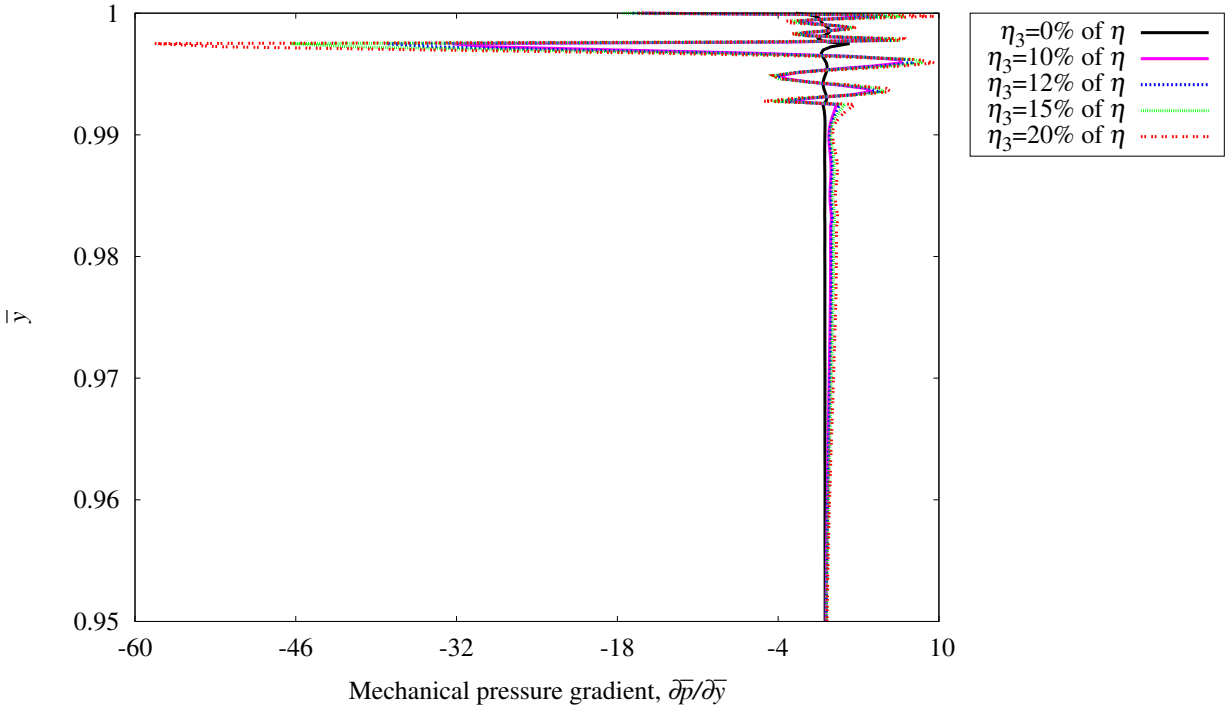

Figure 3.31: Mechanical pressure gradient $\frac{\partial \overline{p}}{\partial \overline{y}}$ versus $\overline{y}$ at $\overline{x} = 0.5$ (exploded view) for different values of η_3 ($\eta_1 = 0$)

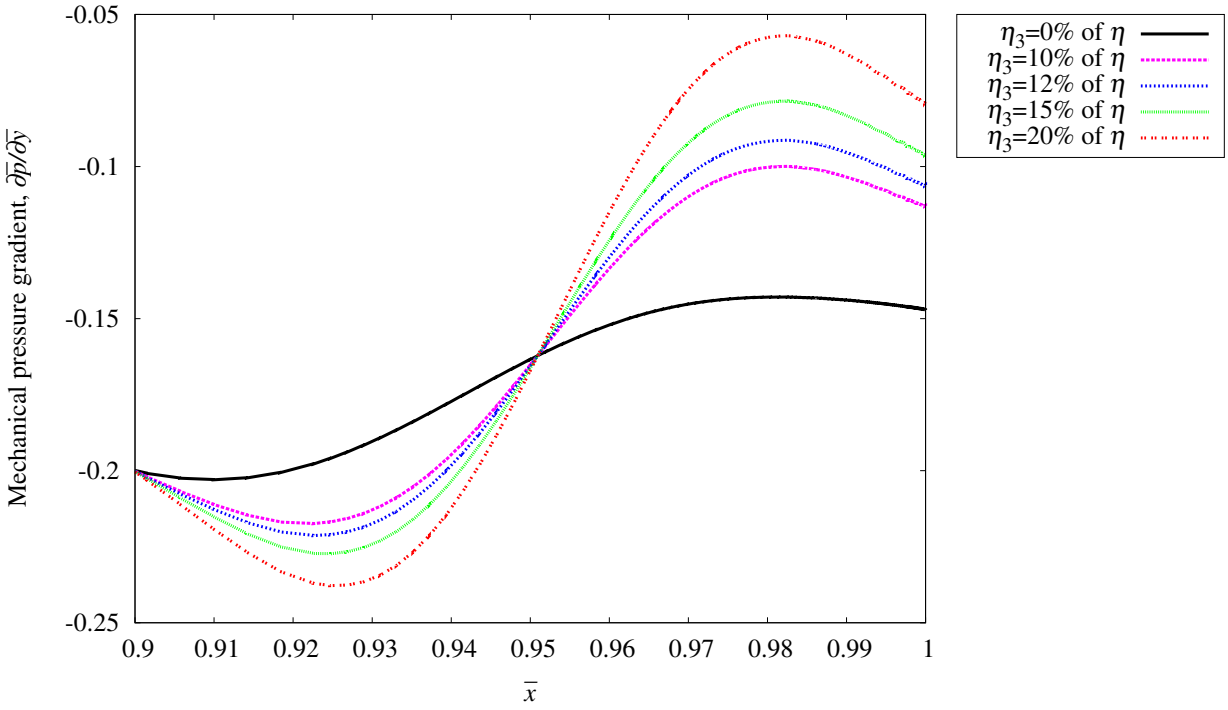

Figure 3.32: Mechanical pressure gradient $\frac{\partial \overline{p}}{\partial \overline{y}}$ versus $\overline{x}$ at $\overline{y} = 0.5$ (exploded view) for different values of η_3 ($\eta_1 = 0$)

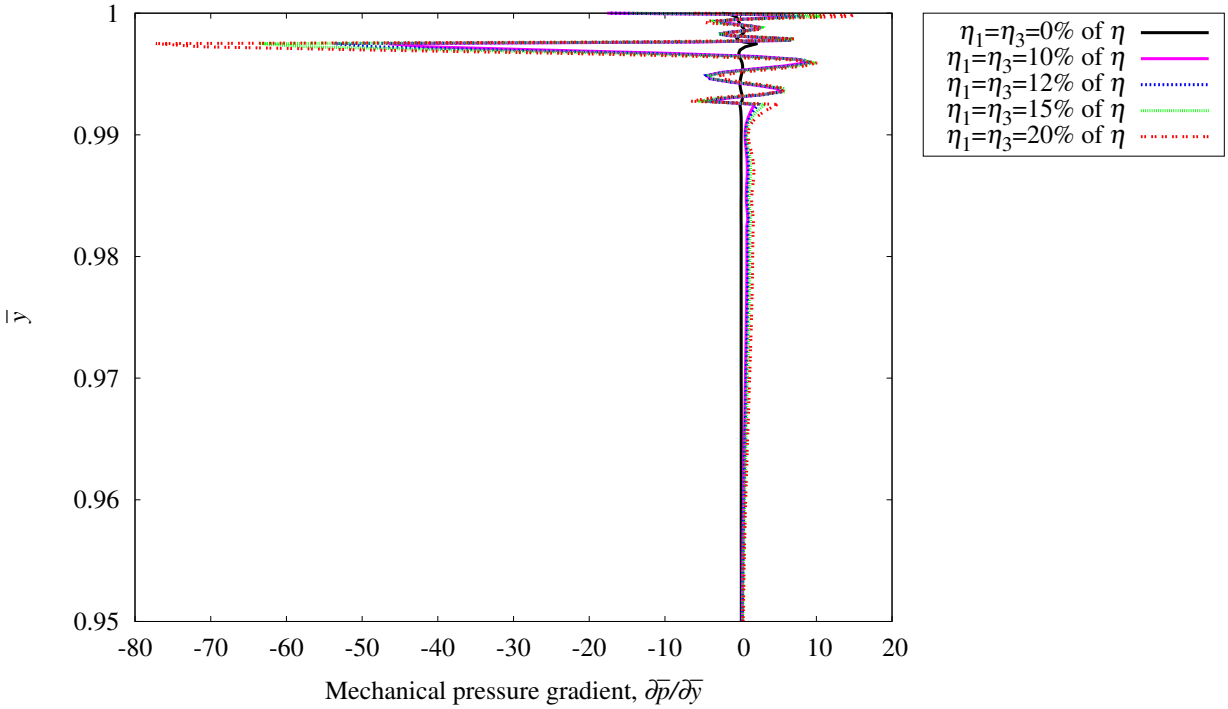

Figure 3.33: Mechanical pressure gradient $\frac{\partial \bar{p}}{\partial \bar{y}}$ versus $\bar{y}$ at $\bar{x} = 0.5$ (exploded view) for different values of η_1 and η_3

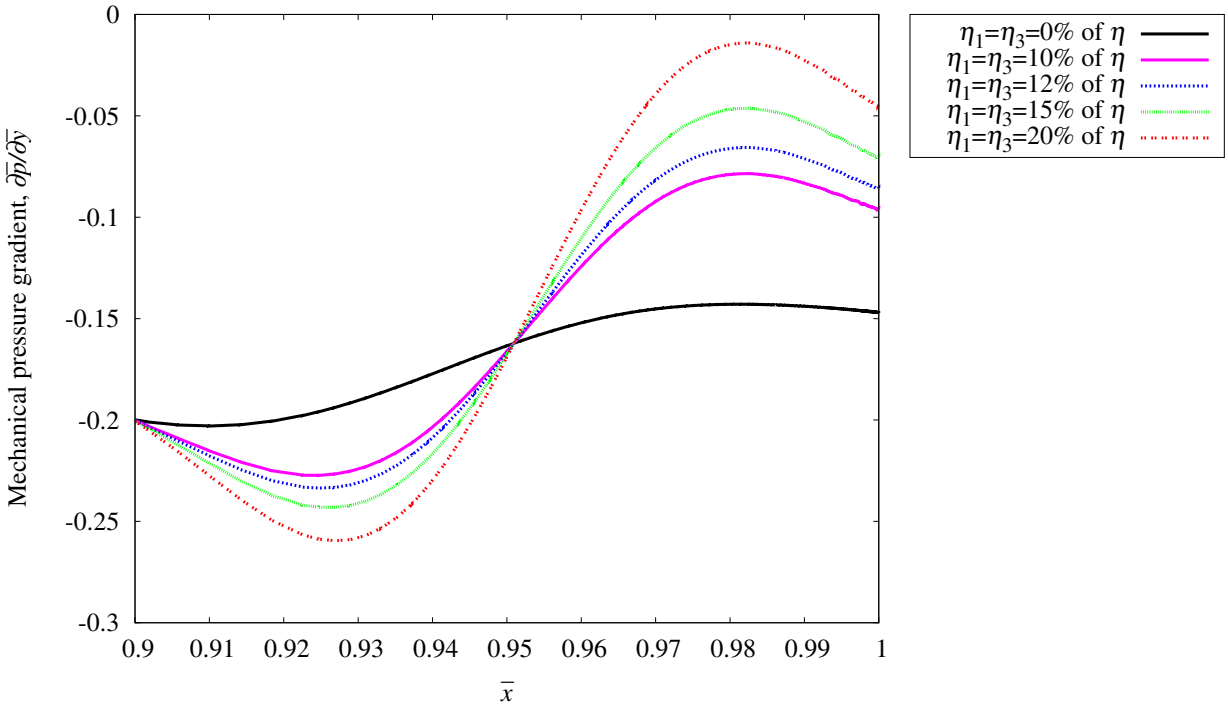

Figure 3.34: Mechanical pressure gradient $\frac{\partial \bar{p}}{\partial \bar{y}}$ versus $\bar{x}$ at $\bar{y} = 0.5$ (exploded view) for different values of η_1 and η_3

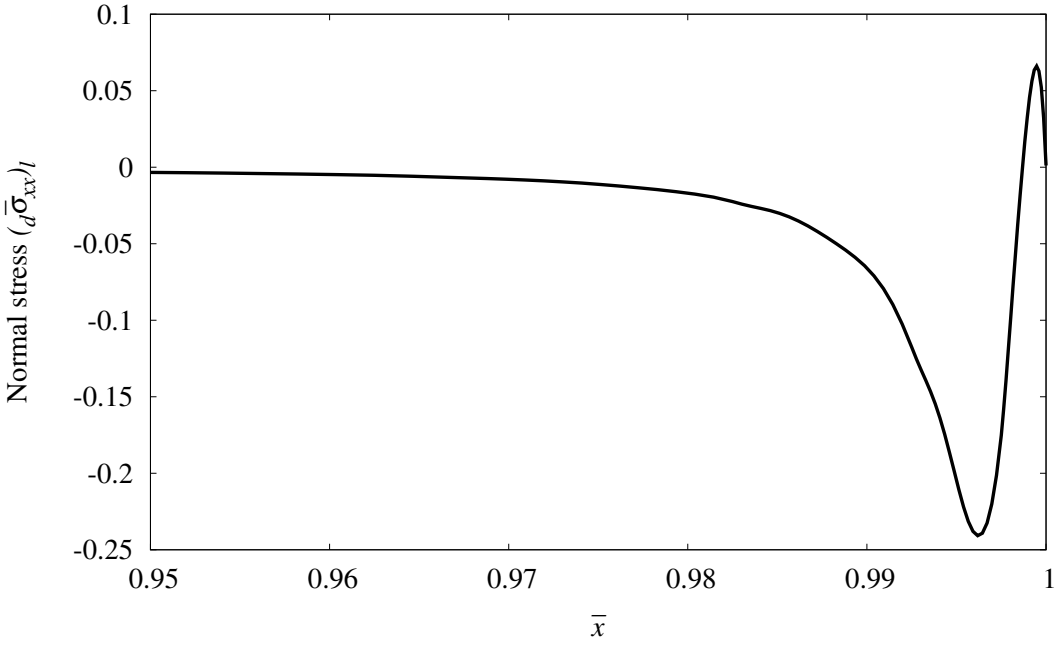

Figure 3.35: Normal stresses $({}_d\overline{\sigma}_{xx})_l$ versus $\overline{x}$ at $\overline{y} = 0.9975$ (exploded view) for $\eta_1 = \eta_3 = 0$

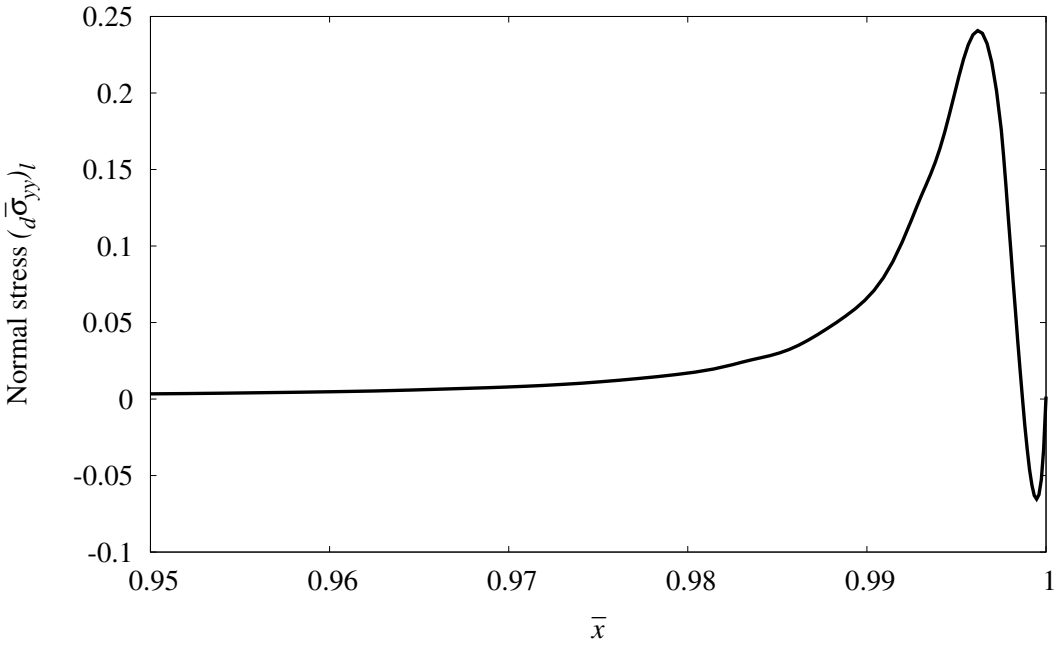

Figure 3.36: Normal stresses $({}_d\overline{\sigma}_{yy})_l$ versus $\overline{x}$ at $\overline{y} = 0.9975$ (exploded view) for $\eta_1 = \eta_3 = 0$

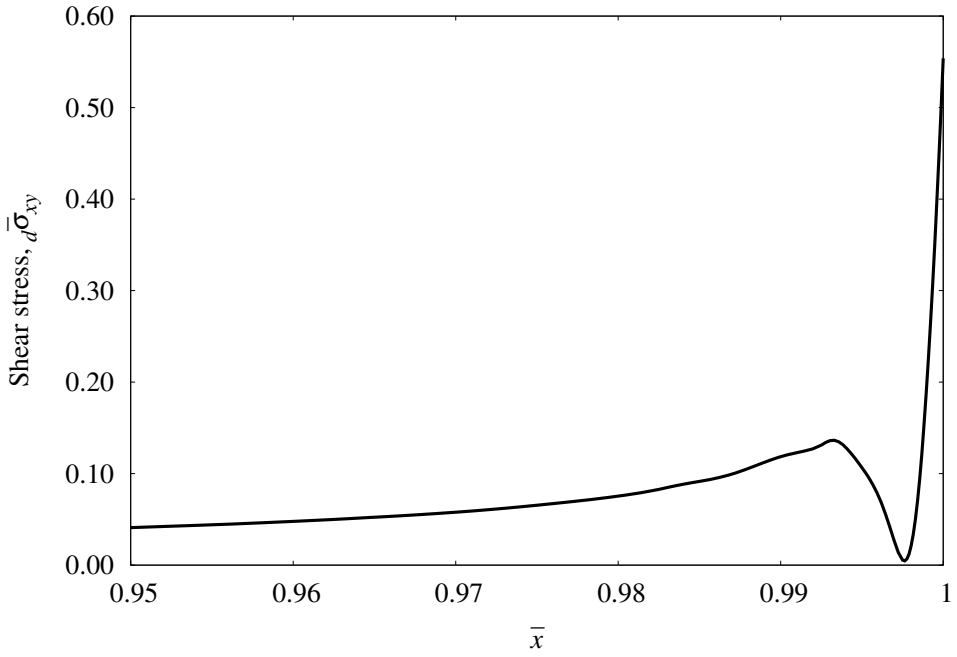

Figure 3.37: Shear stress $_d\overline{\sigma}_{xy}$ versus $\overline{x}$ at $\overline{y}$ = 0.9975 (exploded view) for different values of η_1 and η_3

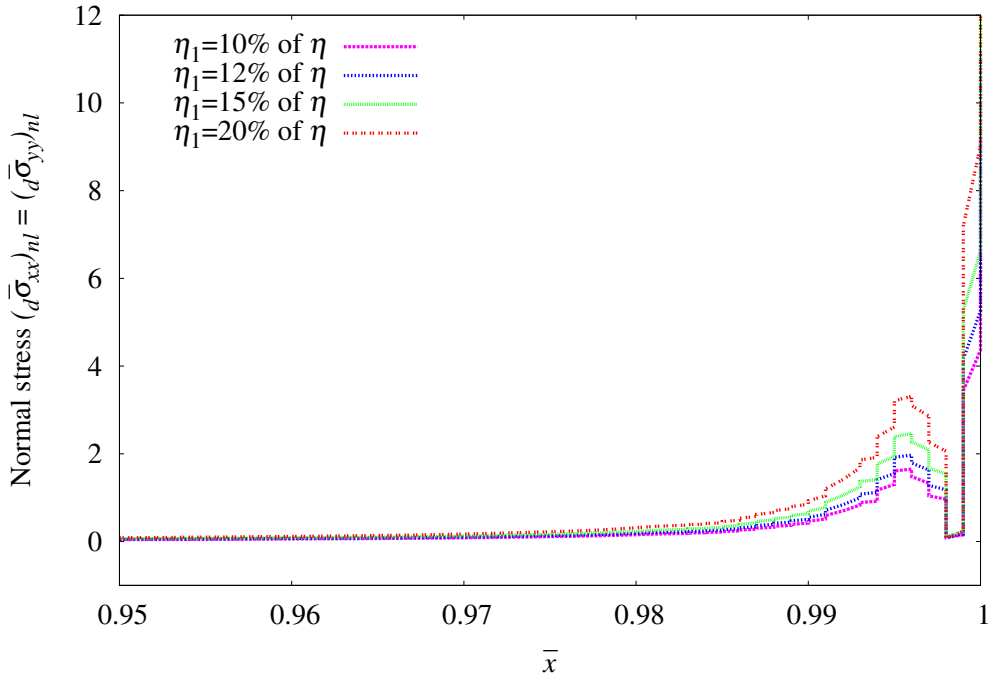

Figure 3.38: Normal stresses $(_d\overline{\sigma}_{xx})_{nl}$ or $(_d\overline{\sigma}_{yy})_{nl}$ versus $\overline{x}$ at $\overline{y}$ = 0.9975 (exploded view) for different values of η_1 ($\eta_3 = 0$)

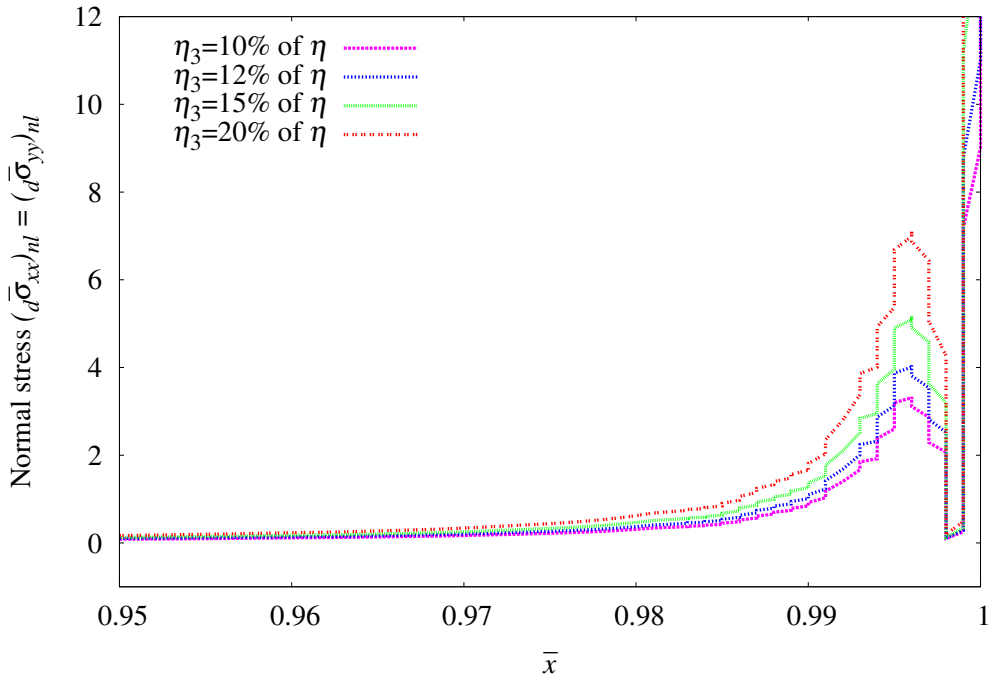

Figure 3.39: Normal stresses $({}_d\overline{\sigma}_{xx})_{nl}$ or $({}_d\overline{\sigma}_{yy})_{nl}$ versus $\overline{x}$ at $\overline{y}$ = 0.9975 (exploded view) for different values of η_3 ($\eta_1 = 0$)

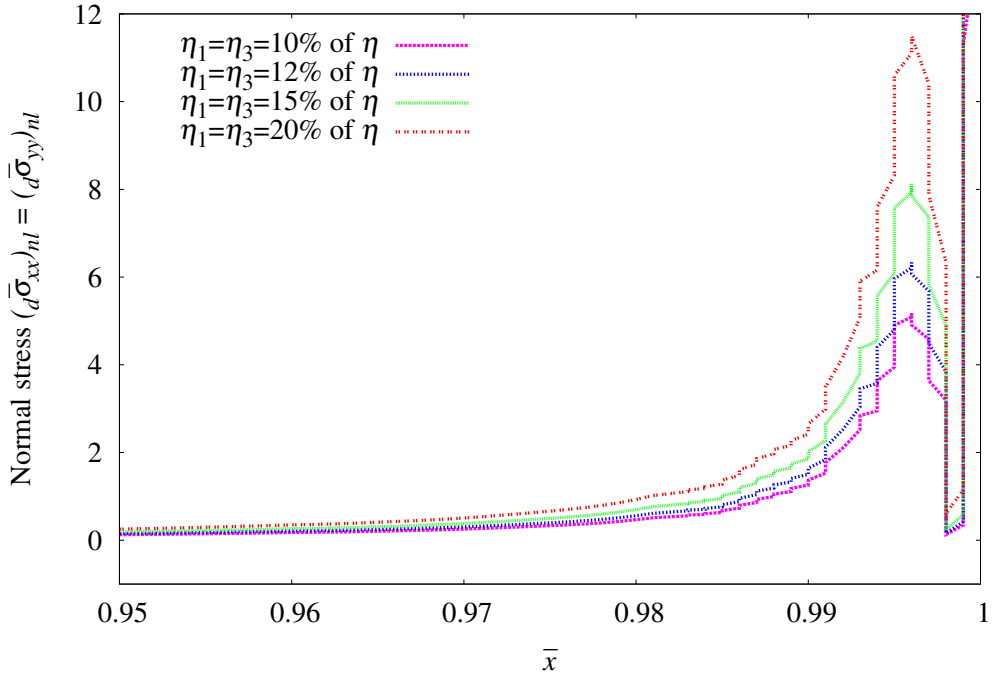

Figure 3.40: Normal stresses $({}_d\overline{\sigma}_{xx})_{nl}$ or $({}_d\overline{\sigma}_{yy})_{nl}$ versus $\overline{x}$ at $\overline{y}$ = 0.9975 (exploded view) for different values of η_1 and η_3

Plots of normal stresses $({}_d\overline{\sigma}_{xx})_l$, $({}_d\overline{\sigma}_{yy})_l$ and shear stress $({}_d\overline{\sigma}_{xy})_l$ near the lid ($\overline{y}$ = 0.9975) are functions of $\overline{x}$ are shown in figures 3.35 – 3.37. Plots of $({}_d\overline{\sigma}_{xx})_{nl} = ({}_d\overline{\sigma}_{yy})_{nl}$ versus $\overline{x}$ at $\overline{y}$ = 0.9975 for different values of η_1, η_3 and $\eta_1 = \eta_3$ are shown in figures 3.38 – 3.40. Significantly higher normal stresses are observed in close proximity along the lid near the right boundary of the cavity. These are higher due to the high velocity gradients near the right boundary of the cavity. In all cases, these normal stress values are significant compared to $({}_d\overline{\sigma}_{xx})_l$ and $({}_d\overline{\sigma}_{yy})_l$ even for low range of the values of $\eta_1 = \eta_3$.

3.4.3 Model Problem-III: Asymmetric Sudden Expansion

In this model problem we consider 3:2 sudden asymmetric sudden expansion. A schematic of the domain with dimensions, origin of the coordinate system $\overline{x}, \overline{y}$ and boundary conditions are shown in figure 3.41(a). A graded finite discretization of the domain using 174 nine node p-version hierarchical elements is shown in figure 3.41(b). This mesh is arrived at adaptively using element residuals.

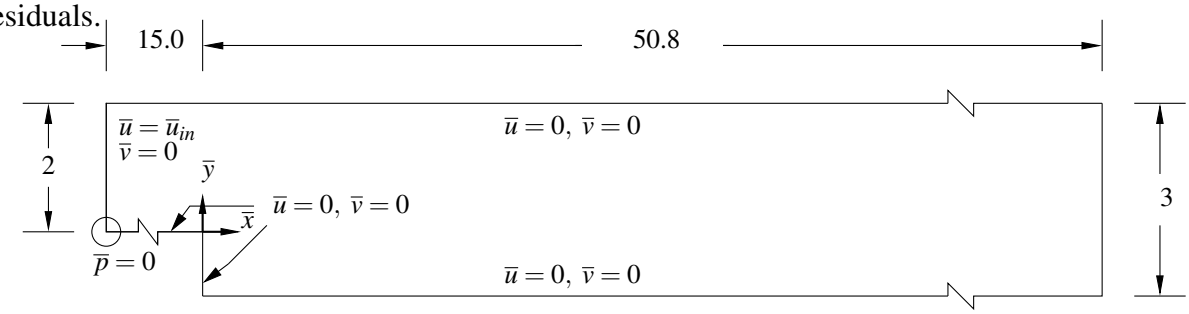

(a) Schematic representation

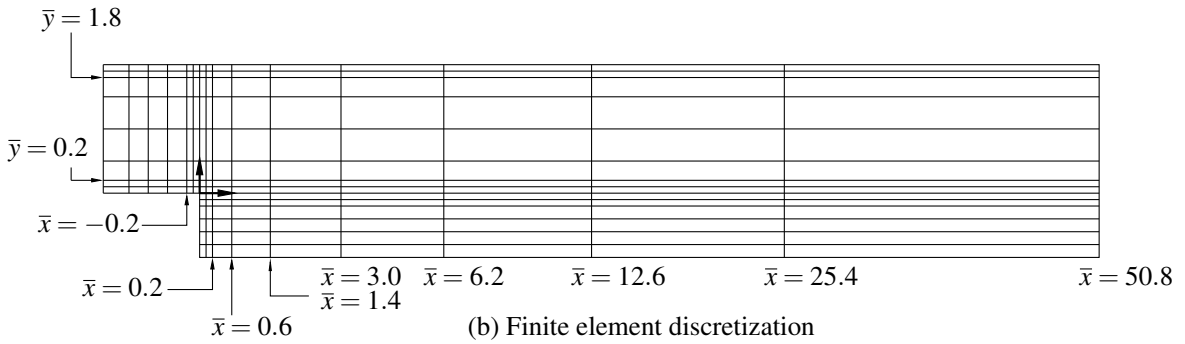

(b) Finite element discretization

Figure 3.41: Schematic representation and finite element discretization for an asymmetric sudden expansion

In this study we choose

$\hat{\bar{\rho}} = \rho_0 = 998.2$ kg/m^3 ; $\hat{\eta} = \eta_0 = 0.001002$ Pa.s.

$\hat{\bar{H}} = L_0 = 0.015$ m, $u_0 = 0.0153247$ m/s

η_1 ; η_3 = 0% of η, 10% of η, 12% of η, 15% of η and 20% of η.

η_1 & η_3 = 0% of η, 5% of η, 6% of η, 7.5% of η and 10% of η.

These give Re = 229.

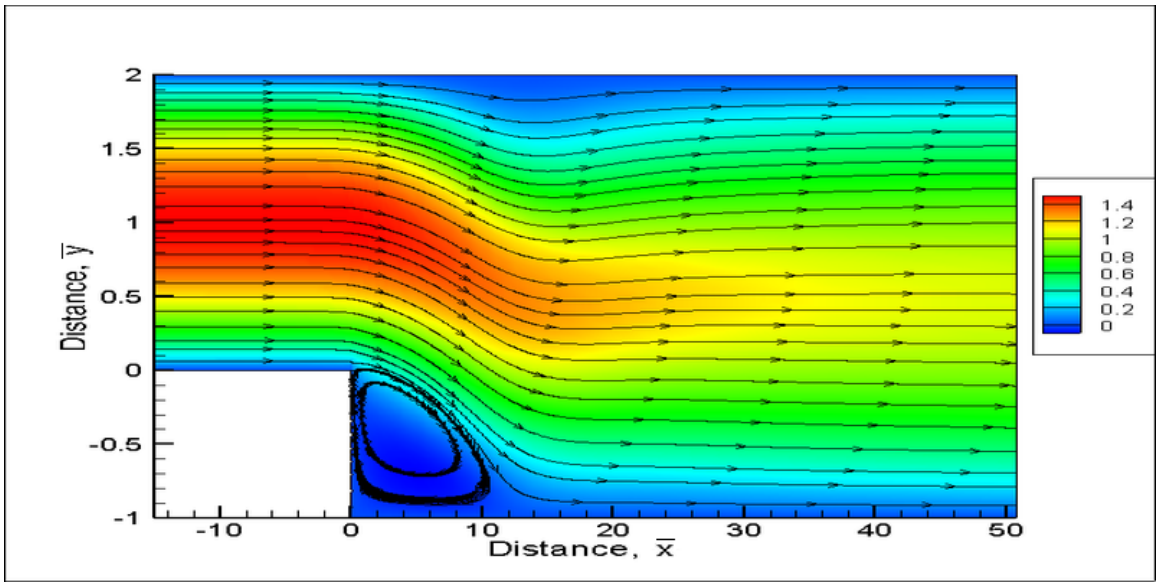

Figure 3.42: Contours of streamlines in the asymmetric sudden expansion for different values of η_1 and η_3

A fully developed velocity profile is applied at the inlet that results in flow rate of 2.02. No BCs are imposed at the outlet. Computations are performed for k = 2 at p-level of 9 for which I values of the order of $O(10^{-7})$ are achieved. Here also the velocity field is not affected by non-zero η_1 and/or η_3. Figure 3.42 shows contours of streamlines. Solution is smooth (free of any spurious oscillations) with clearly defined recirculation zone. Graphs of velocity $\bar{u}$ versus $\bar{y}$ at $\bar{x}$ = 0.0 (at expansion point), 0.2, 5.0 and 50.8 (outlet) are shown in figure 3.43. Plots of ${}_d\bar{\sigma}_{xy}$ versus $\bar{y}$ at the same locations are shown in figure 3.44. From figure 3.43(c) (velocity $\bar{u}$ versus $\bar{y}$ at $\bar{x}$ = 5.0), we observe negative $\bar{u}$ in the recirculation region. The deviatoric shear stress graph at $\bar{x}$ = 50.8 (outlet) confirms that the flow is not fully developed, hence the reason for not using the fully developed flow boundary conditions at the outlet.

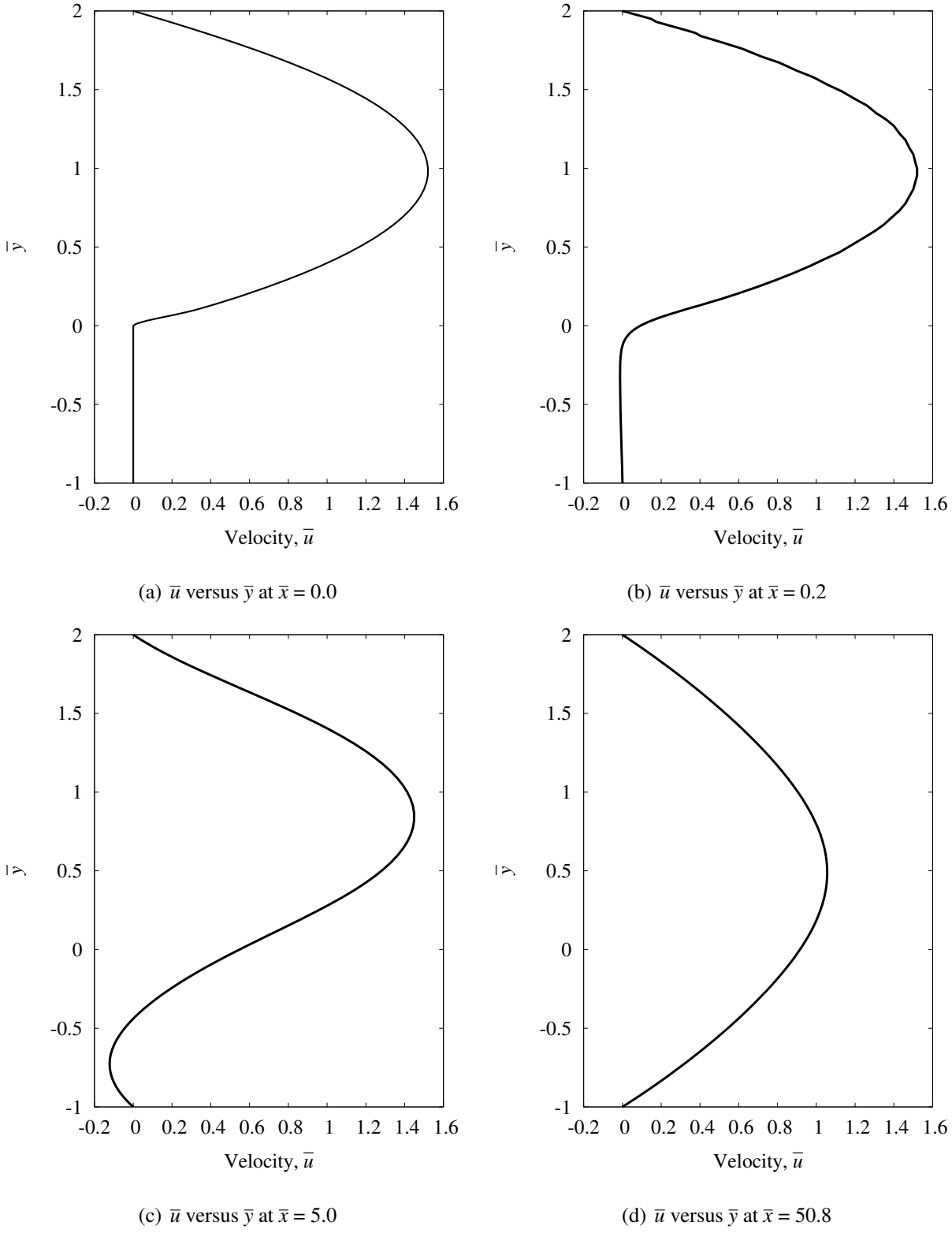

(a) $\overline{u}$ versus $\overline{y}$ at $\overline{x} = 0.0$

(b) $\overline{u}$ versus $\overline{y}$ at $\overline{x} = 0.2$

(c) $\overline{u}$ versus $\overline{y}$ at $\overline{x} = 5.0$

(d) $\overline{u}$ versus $\overline{y}$ at $\overline{x} = 50.8$

Figure 3.43: Velocities $\overline{u}$ versus $\overline{y}$ at different values of $\overline{x}$ for different values of η_1 and/or η_3

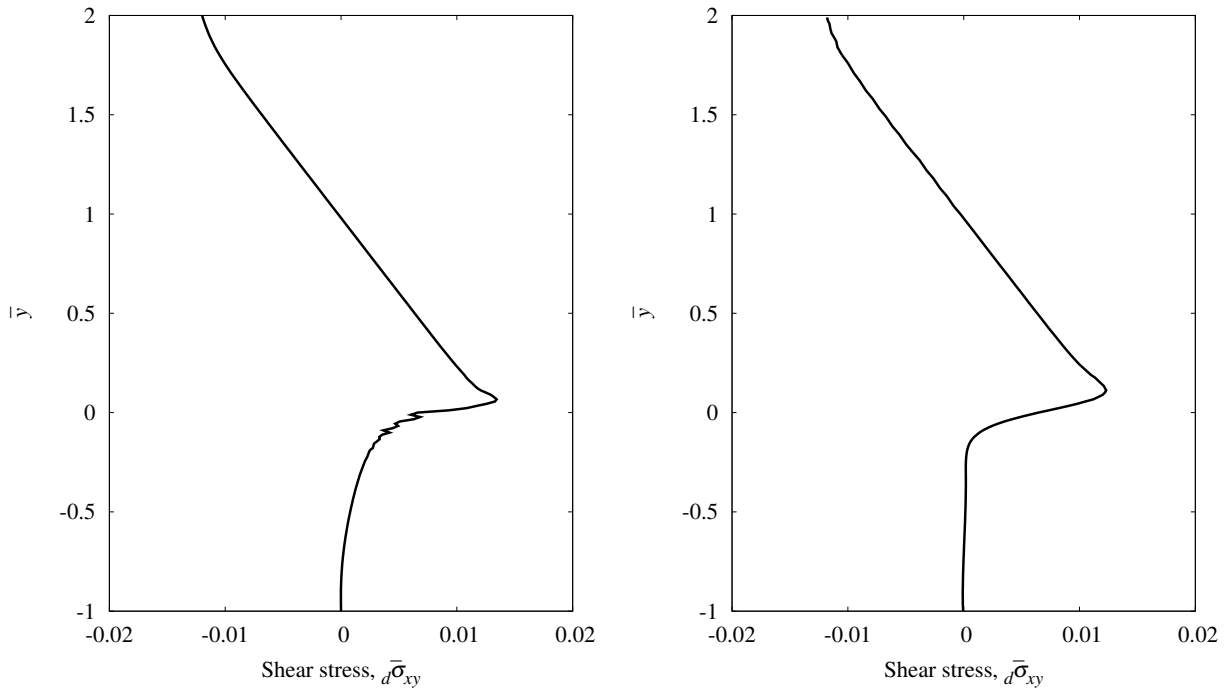

(a) ${}_d\overline{\sigma}_{xy}$ versus $\overline{y}$ at $\overline{x} = 0.0$

(b) ${}_d\overline{\sigma}_{xy}$ versus $\overline{y}$ at $\overline{x} = 0.2$

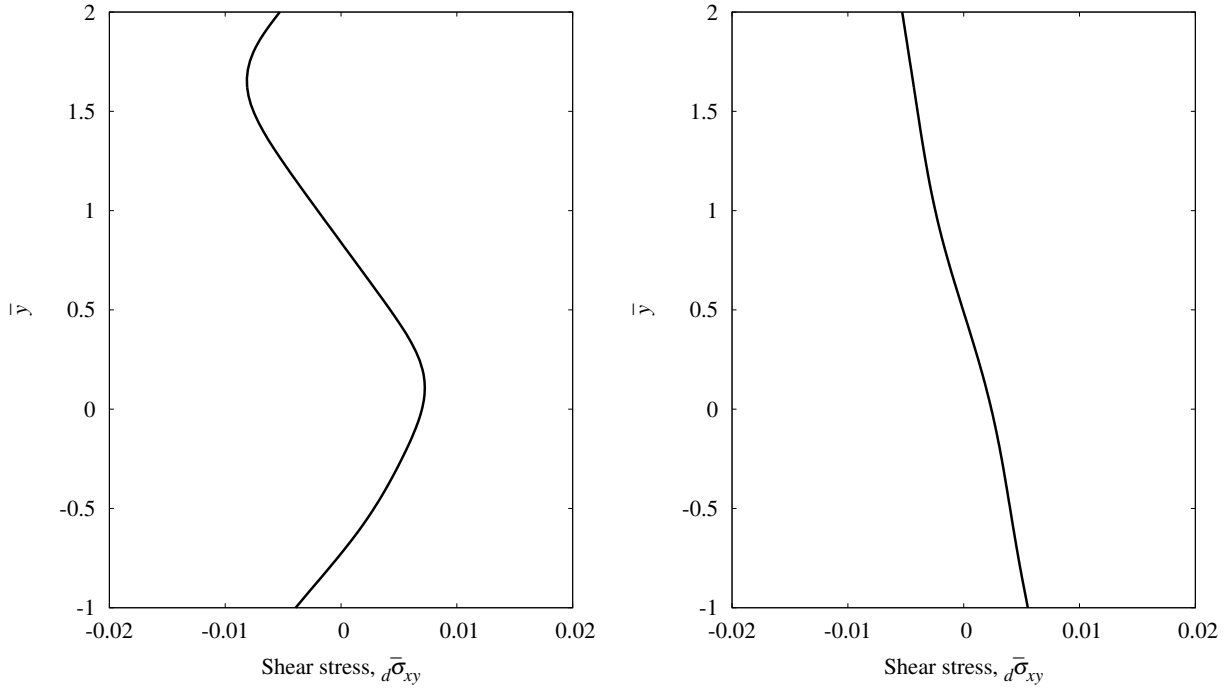

(c) ${}_d\overline{\sigma}_{xy}$ versus $\overline{y}$ at $\overline{x} = 5.0$

(d) ${}_d\overline{\sigma}_{xy}$ versus $\overline{y}$ at $\overline{x} = 50.8$

Figure 3.44: Shear stress ${}_d\overline{\sigma}_{xy}$ versus $\overline{y}$ at different values of $\overline{x}$ for different values of η_1 and/or η_3

Plots of $({}_d\overline{\sigma}_{xx})_l$ and $({}_d\overline{\sigma}_{yy})_l$ versus $\overline{y}$ at $\overline{x}$ = 0.0 (expansion point) are shown in figures 3.45 – 3.46. We clearly observe $({}_d\overline{\sigma}_{xx})_l = -({}_d\overline{\sigma}_{yy})_l$. Oscillations in the results at $\overline{x}$ = 0, $\overline{y}$ = 0 and its vicinity are due to non differentiable geometry at the expansion point and non-uniqueness of the definition of the boundary conditions. This behavior is highly isolated, hence does not influence the computed solutions away from it.

Plots of $({}_d\overline{\sigma}_{xx})_{nl} = ({}_d\overline{\sigma}_{yy})_{nl}$ versus $\overline{y}$ at $\overline{x}$ = 0.0 for different choices of η_1, η_3 and $\eta_1 = \eta_3$ are shown in figures 3.47 – 3.48. From figures 3.47(a) and (b), we clearly observe higher stresses for same value of η_3 as η_1. The individual non-linear terms associated with η_1 and η_3 are not identical with each other. Hence, we do not observe additive effect in case of graphs associated with $\eta_1 = \eta_3$. The magnitude of $({}_d\overline{\sigma}_{xx})_{nl} = ({}_d\overline{\sigma}_{yy})_{nl}$ is much higher for all values of η_1, η_3 and $\eta_1 = \eta_3$ when compared with $({}_d\overline{\sigma}_{xx})_l$ and $({}_d\overline{\sigma}_{yy})_l$ (when smooth) in figures 3.45 – 3.46.

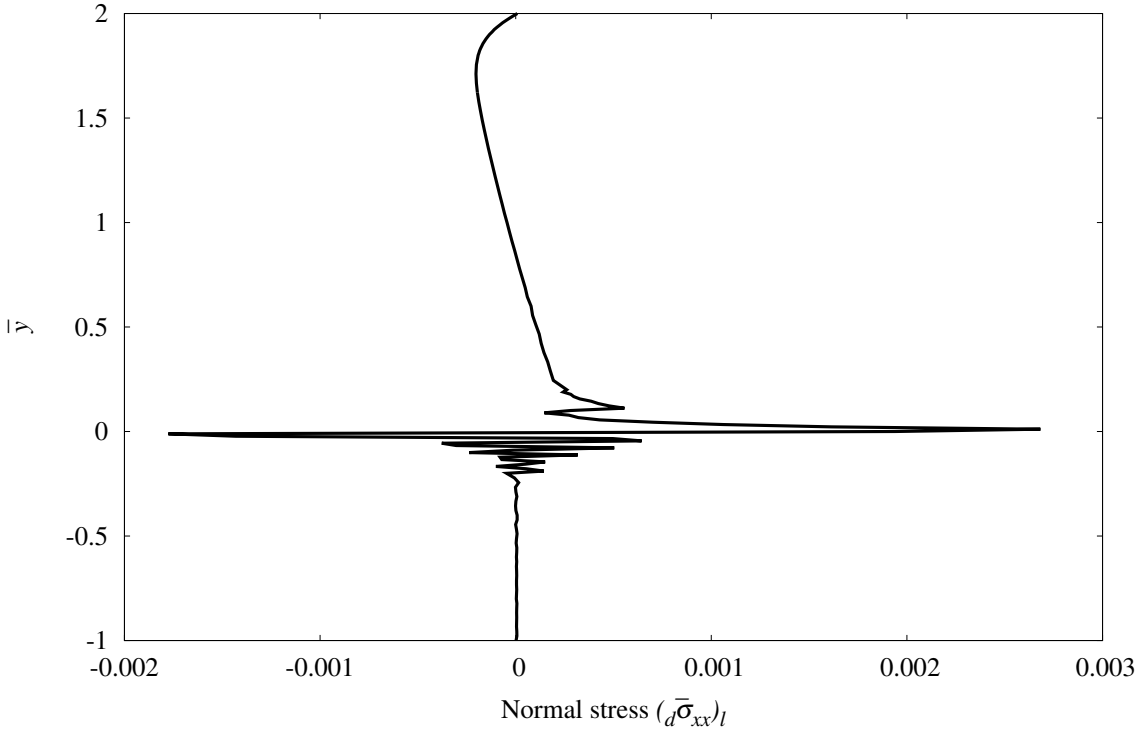

Figure 3.45: Normal stresses $({}_d\overline{\sigma}_{xx})_l$ versus $\overline{y}$ at $\overline{x}$ = 0.0 for $\eta_1 = \eta_3 = 0$

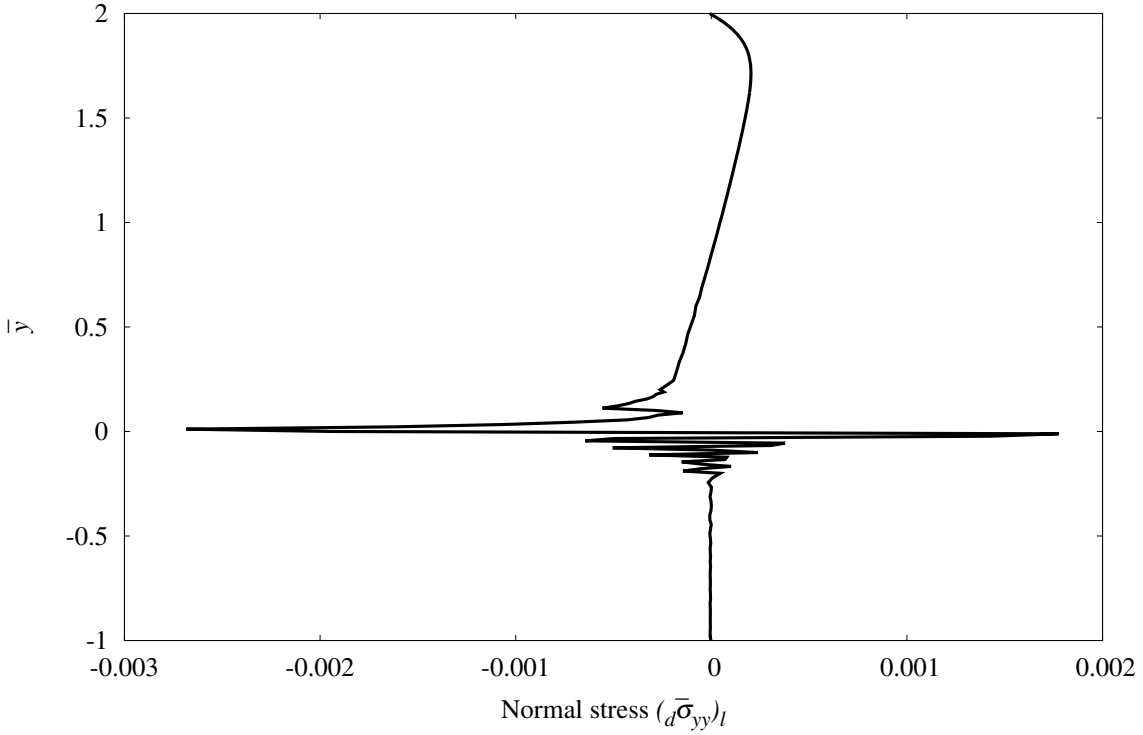

Figure 3.46: Normal stresses $({}_d\overline{\sigma}_{yy})_l$ versus $\bar{y}$ at $\bar{x} = 0.0$ for $\eta_1 = \eta_3 = 0$

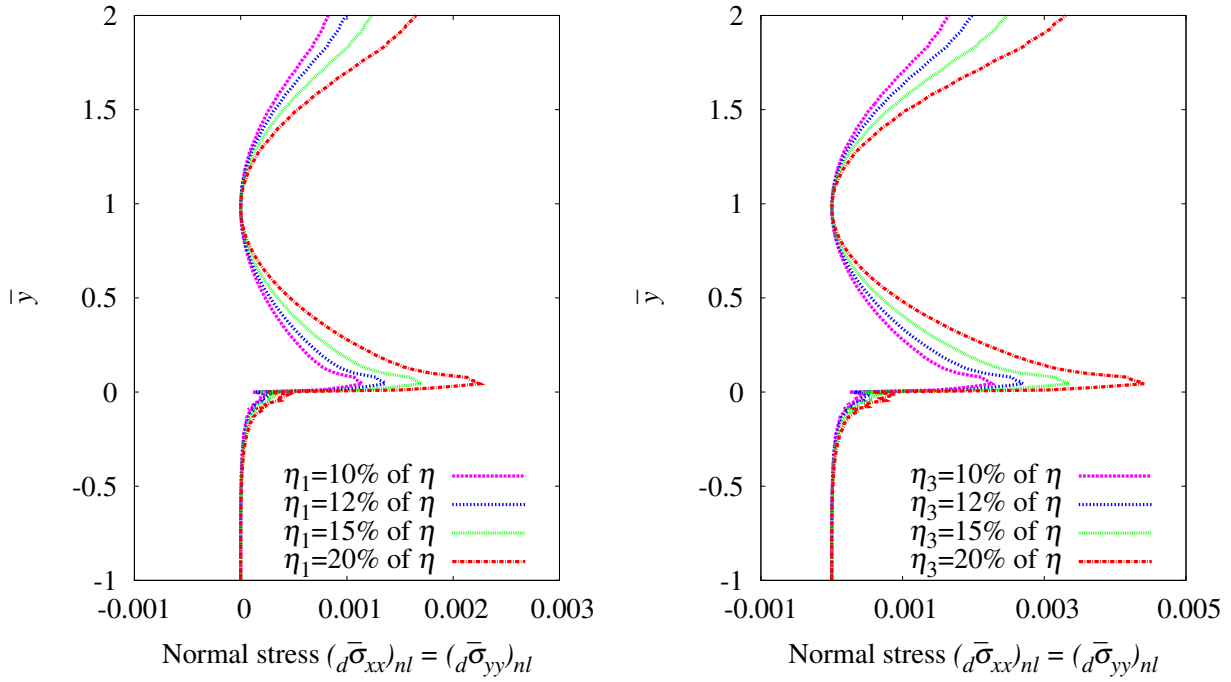

(a) $({}_d\overline{\sigma}_{xx})_{nl}$ or $({}_d\overline{\sigma}_{yy})_{nl}$ versus $\bar{y}$ at $\bar{x} = 0.0$

(b) $({}_d\overline{\sigma}_{xx})_{nl}$ or $({}_d\overline{\sigma}_{yy})_{nl}$ versus $\bar{y}$ at $\bar{x} = 0.0$

Figure 3.47: Normal stress $({}_d\overline{\sigma}_{xx})_{nl}$ or $({}_d\overline{\sigma}_{yy})_{nl}$ versus $\bar{y}$ at $\bar{x} = 0.0$ for different values of η_1 and η_3

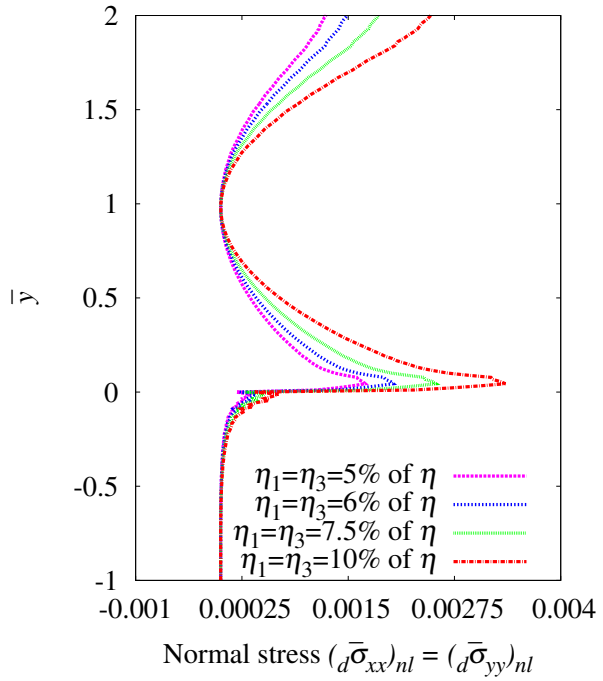

Figure 3.48: Normal stress $({}_d\overline{\sigma}_{xx})_{nl}$ or $({}_d\overline{\sigma}_{yy})_{nl}$ versus $\bar{y}$ at $\bar{x} = 0.0$ for different values of η_1 and η_3

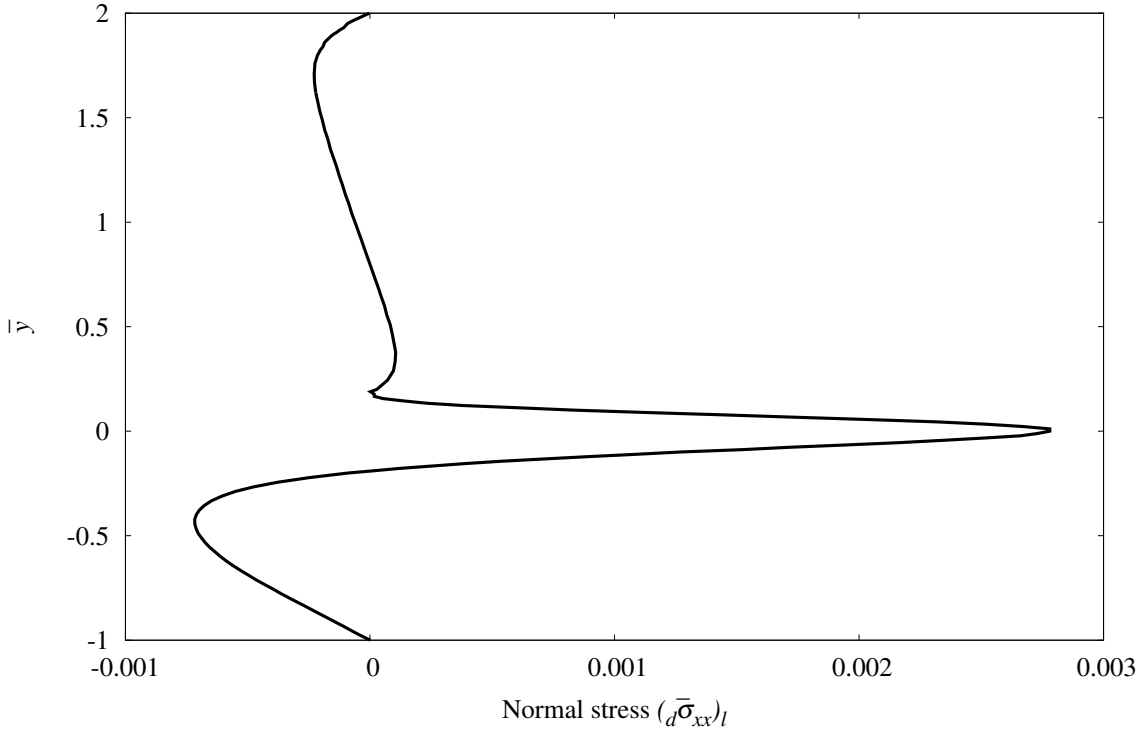

Figure 3.49: Normal stresses $({}_d\overline{\sigma}_{xx})_l$ versus $\bar{y}$ at $\bar{x} = 0.2$ for $\eta_1 = \eta_3 = 0$

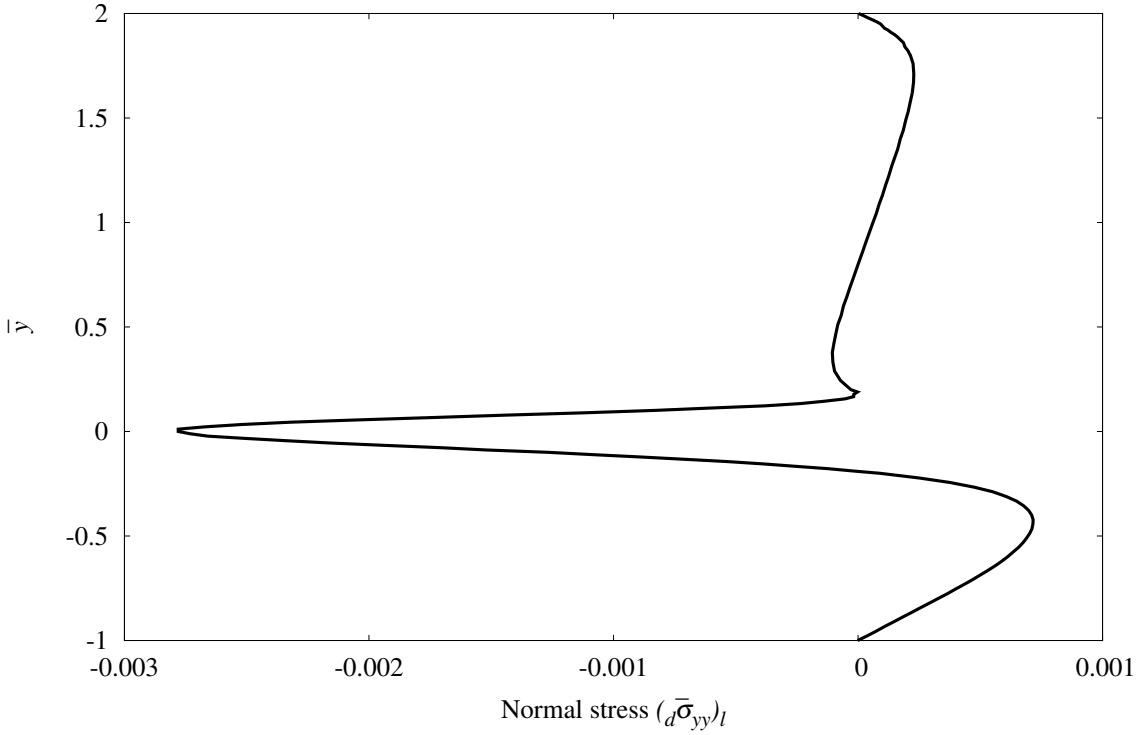

Figure 3.50: Normal stresses $({}_d\overline{\sigma}_{yy})_l$ versus $\bar{y}$ at $\bar{x} = 0.2$ for $\eta_1 = \eta_3 = 0$

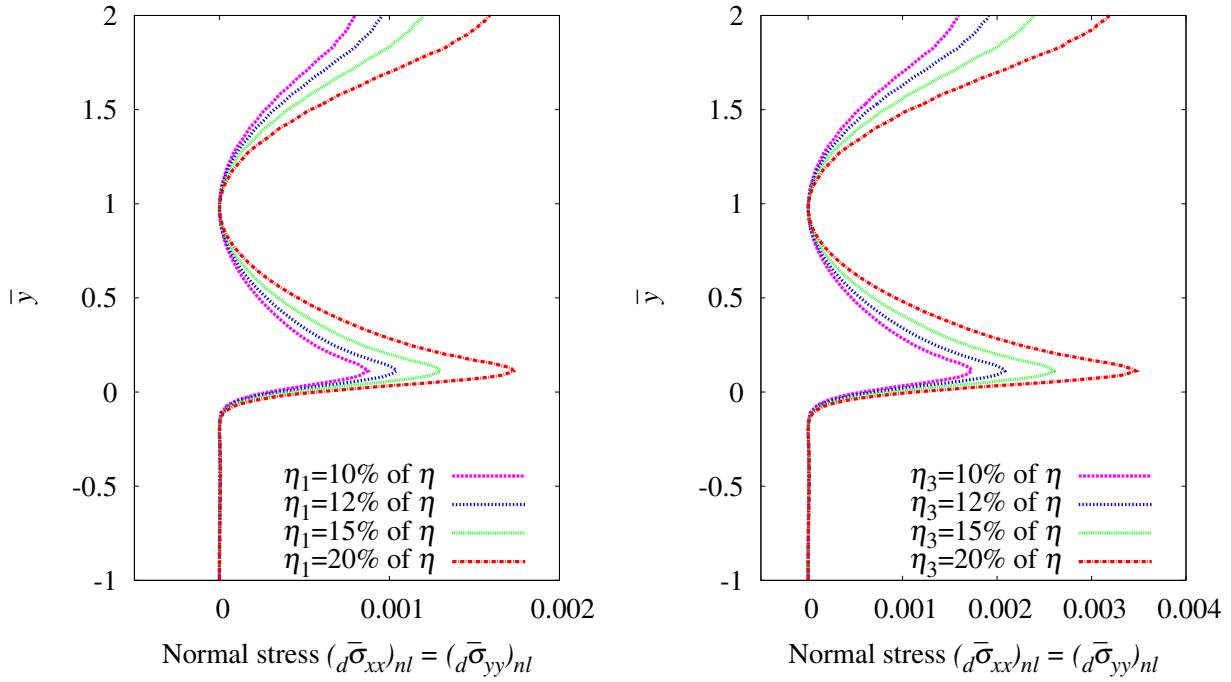

(a) $({}_d\overline{\sigma}_{xx})_{nl}$ or $({}_d\overline{\sigma}_{yy})_{nl}$ versus $\bar{y}$ at $\bar{x} = 0.2$

(b) $({}_d\overline{\sigma}_{xx})_{nl}$ or $({}_d\overline{\sigma}_{yy})_{nl}$ versus $\bar{y}$ at $\bar{x} = 0.2$

Figure 3.51: Normal stress $({}_d\overline{\sigma}_{xx})_{nl}$ or $({}_d\overline{\sigma}_{yy})_{nl}$ versus $\bar{y}$ at $\bar{x} = 0.2$ for different values of η_1 and η_3

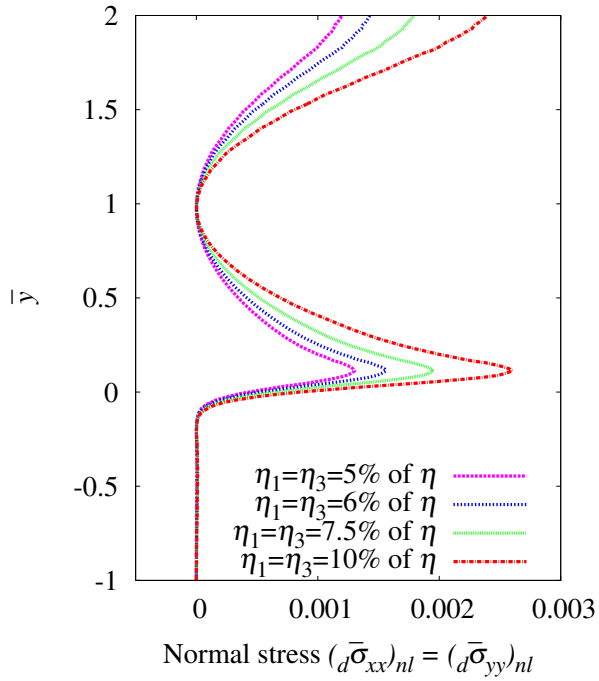

Figure 3.52: Normal stress $({}_d\bar{\sigma}_{xx})_{nl}$ or $({}_d\bar{\sigma}_{yy})_{nl}$ versus $\bar{y}$ at $\bar{x} = 0.2$ for different values of η_1 and η_3

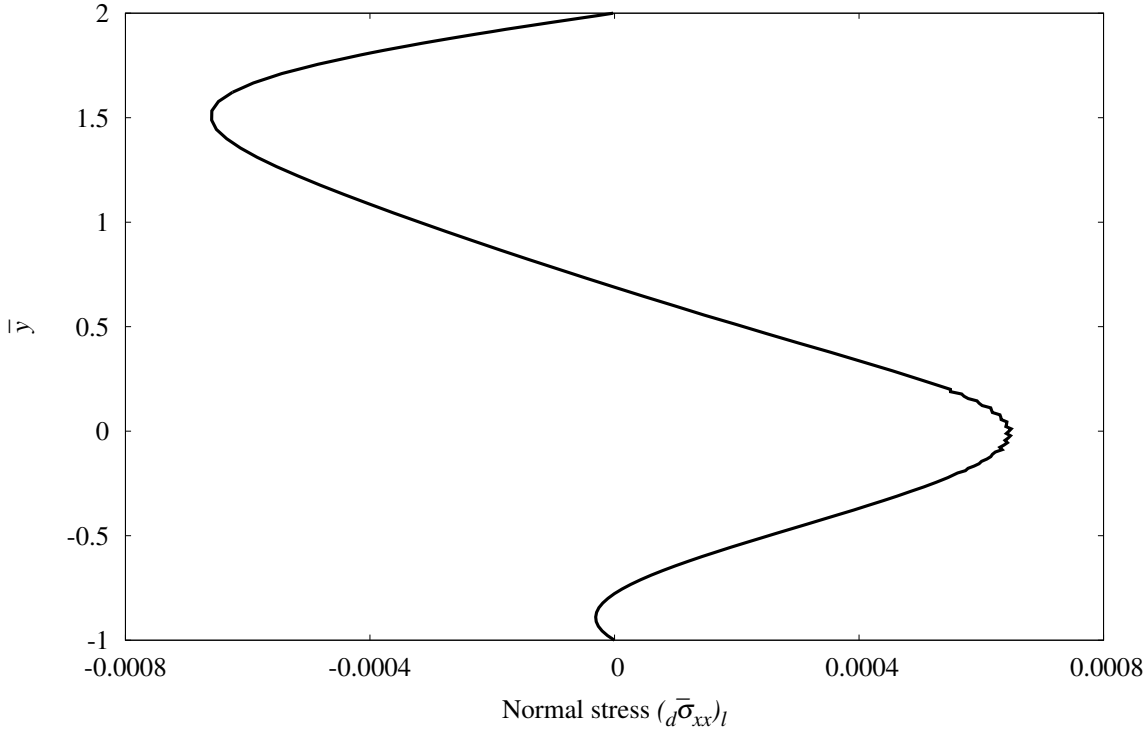

Figure 3.53: Normal stresses $({}_d\bar{\sigma}_{xx})_l$ versus $\bar{y}$ at $\bar{x} = 5.0$ for $\eta_1 = \eta_3 = 0$

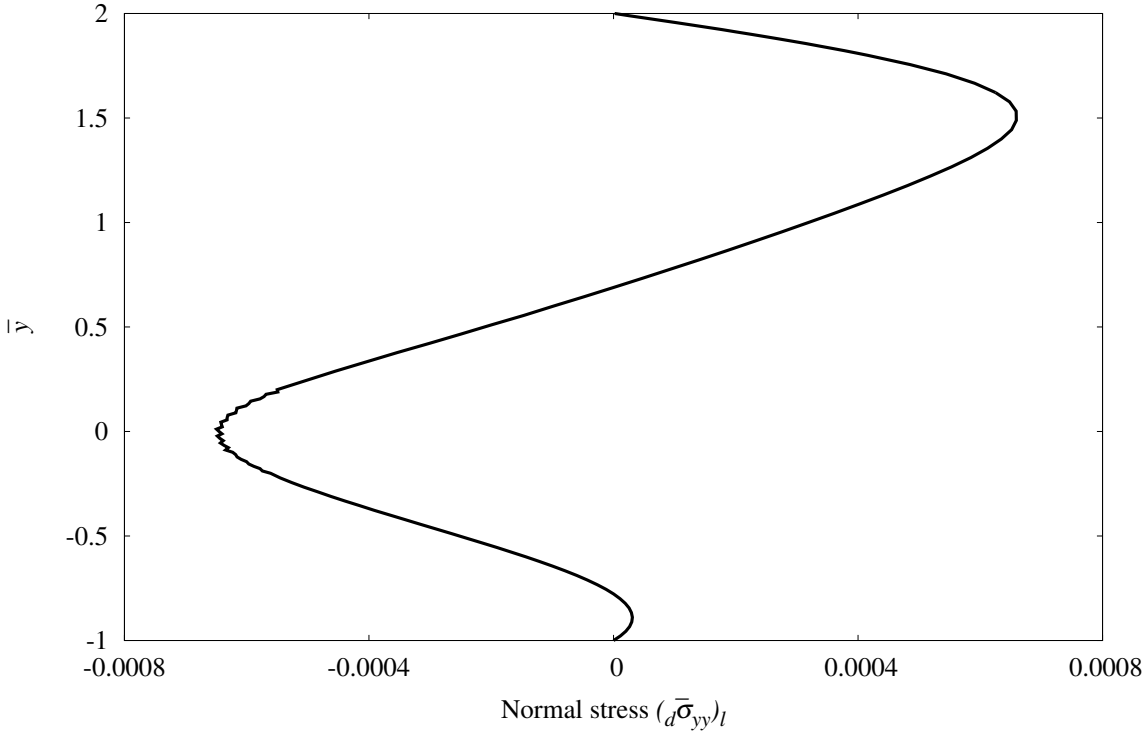

Figure 3.54: Normal stresses $({}_d\overline{\sigma}_{yy})_l$ versus $\bar{y}$ at $\bar{x} = 5.0$ for $\eta_1 = \eta_3 = 0$

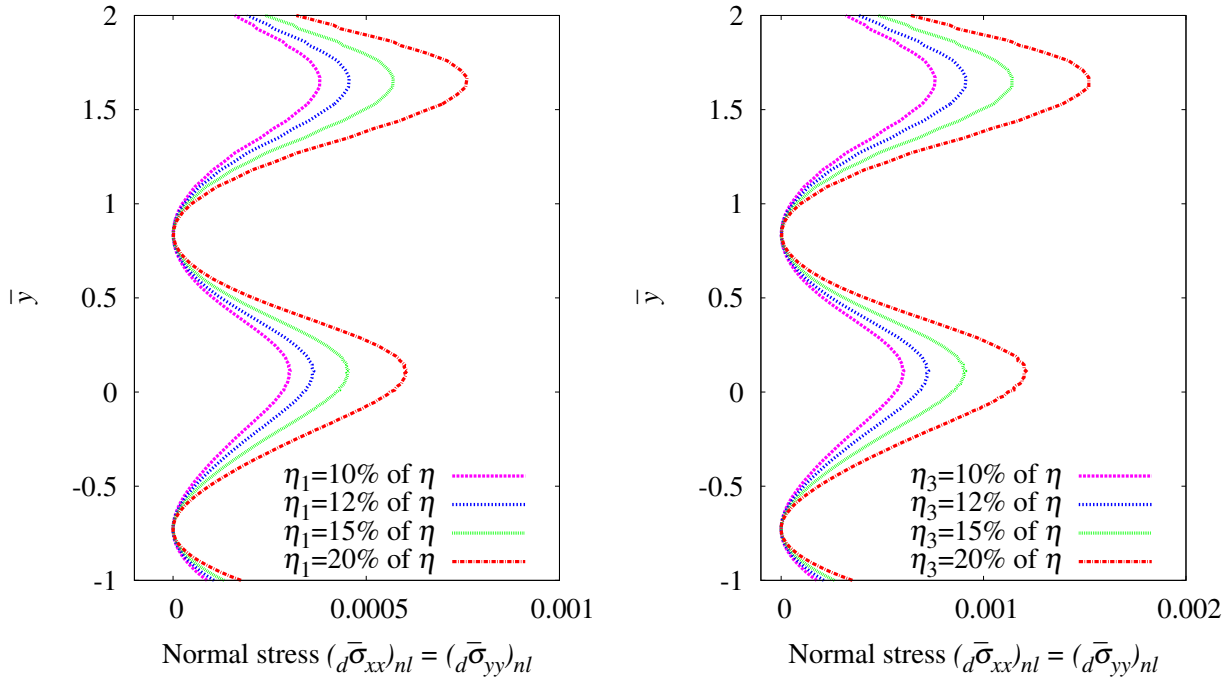

(a) $({}_d\overline{\sigma}_{xx})_{nl}$ or $({}_d\overline{\sigma}_{yy})_{nl}$ versus $\bar{y}$ at $\bar{x} = 5.0$

(b) $({}_d\overline{\sigma}_{xx})_{nl}$ or $({}_d\overline{\sigma}_{yy})_{nl}$ versus $\bar{y}$ at $\bar{x} = 5.0$

Figure 3.55: Normal stress $({}_d\overline{\sigma}_{xx})_{nl}$ or $({}_d\overline{\sigma}_{yy})_{nl}$ versus $\bar{y}$ at $\bar{x} = 5.0$ for different values of η_1 and η_3

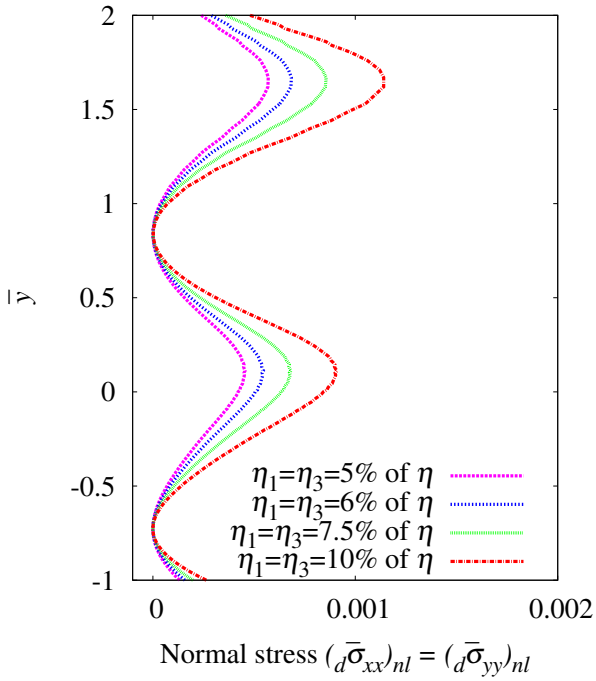

Figure 3.56: Normal stress $({}_d\overline{\sigma}_{xx})_{nl}$ or $({}_d\overline{\sigma}_{yy})_{nl}$ versus $\overline{y}$ at $\overline{x}$ = 5.0 for different values of η_1 and η_3

Graphs similar to those in figures 3.45 – 3.48 for $\overline{x}$ = 0.2 and $\overline{x}$ = 5.0 are shown in figures 3.49 – 3.56 with similar behavior as discussed for the location $\overline{x}$ = 0.0 (figures 3.45 – 3.48).

3.5 Summary

Three model problems have been presented: fully developed flow between parallel plates, a square lid driven cavity and a 3:2 asymmetric sudden expansion to demonstrate the significance of $[\bar{D}]^2$ term in the constitutive theory for deviatoric stress tensor $[{}_d\overline{\sigma}]$. Presence of $[\bar{D}]^2$ term in the form of $\eta_1[\bar{D}]^2$ and $\eta_3\left(tr[\bar{D}]^2\right)[I]$ in addition to $2\eta[\bar{D}]$ requires two additional material coefficients η_1 and η_3 i.e. the constitutive theory for $[{}_d\overline{\sigma}]$ presented here needs to be calibrated. Numerical studies presented here using values of η_1 and η_3 as fraction of η simply demonstrate the ability of this constitutive theory in producing normal stresses in flows that are believed to be pure shear flows (parallel plates) and additional normal stresses in flows in which normal stresses already exist (cavity, expansion).

Chapter 4

Summary and Conclusions

This thesis presents the numerical investigation of constitutive theories for heat vector in Lagrangian description for thermoelastic solids that are: (i) derived purely using entropy inequality and (ii) derived using theory of generators and invariants and is based on integrity. In the first case, the constitutive theory for $\boldsymbol{q}$ is a linear function of temperature gradient and the material coefficient (thermal conductivity) can be a function of temperature. In the second constitutive theory, the heat vector is up to a cubic function of temperature gradients and the material coefficients can be a function of temperature as well as invariant of temperature gradient. Two numerical studies presented here show that when the temperature gradients are significant such that their squares and cubes cannot be neglected compared to the temperature gradient, the constitutive theory based on pure Fourier heat conduction law is inadequate. With progressively increasing temperature gradients, the constitutive theory based on the theory of generators and invariants describes the physics of heat conduction more realistically. Numerical studies clearly demonstrate significant deviation of temperature distribution along the rod when compared with Fourier heat conduction law, as the temperature gradients increase.

The second numerical investigation presented in this thesis is related to using the constitutive theory for viscous, incompressible fluids for which the deviatoric stress tensor is derived [1] based on the theory of generators and invariants in which only up to quadratic terms in $[\bar{D}]$ are retained.

The presence of $[\bar{D}]^2$ and $\left(tr[\bar{D}]^2\right)[I]$ terms in the constitutive theory for ${}_d\overline{\boldsymbol{\sigma}}$ in addition to $[\bar{D}]$ brings in additional physics. The numerical investigation presented in this thesis are used to illustrate the additional features in the flow physics that are incorporated due to this new constitutive theory. These are summarized in the following. Fully developed flow between parallel plates, a square lid driven cavity and a 3:2 asymmetric expansion are used as model problems.

(1) The velocity field remains unaffected due to η_1 and η_3 associated with the quadratic terms in $[\bar{D}]$ in the constitutive theory. This is comforting as the Newton's law of viscosity described this quite accurately and that the new constitutive theory does not alter it.

(2) The most significant feature of the new constitutive theory is that it always produces deviatoric normal stresses in all flows, even in flow of simple fluids between parallel plates.

(3) When the deviatoric normal stresses are decomposed into linear (due to standard Newton's law of viscosity) and the non-linear parts (additional due to the new theory), we observe that $({}_d\overline{\sigma}_{xx})_l = -({}_d\overline{\sigma}_{yy})_l$ as expected, but $({}_d\overline{\sigma}_{xx})_{nl} = ({}_d\overline{\sigma}_{yy})_{nl}$ in all cases and the shear stress remain the same as from Newton's law of viscosity.

(4) All three numerical studies with three model problems demonstrate that $({}_d\overline{\sigma}_{xx})_{nl}$ and $({}_d\overline{\sigma}_{yy})_{nl}$ are often significant in magnitude compared to their linear parts for the values of η_1 and η_3 used here in the studies. Clearly, as η_1 and η_3 are increased, the non-linear normal stresses increase in magnitude as well.

These constitutive theories for heat vector and ${}_d\overline{\boldsymbol{\sigma}}$ investigated here clearly show that these permit additional physics in the mathematical models compared to presently used theories. Calibration of these theories through experiments is vital in determining the actual values of the new material coefficients so that these theories can be used in actual applications.

Bibliography

[1] Surana, Karan S. *Advanced Mechanics of Continua*. CRC Press, Boca Raton, FL, 2015.

[2] Reddy, J. N. *An Introduction to Continuum Mechanics: with Application*. Cambridge University Press, 2008.

[3] Eringen, A. C. *Mechanics of Continua*. John Wiley and Sons, 1967.

[4] Eringen, A. C. *Nonlinear Theory of Continuous Media*. McGraw-Hill, 1962.

[5] Carroll O Bennett and John Earle Myers. *Momentum, heat, and mass transfer*. McGraw-Hill New York, 1962.

[6] Dale Arden Anderson, John C Tannehill, and Richard H Pletcher. Computational fluid mechanics and heat transfer. 1984.

[7] Theodore L Bergman, Frank P Incropera, David P DeWitt, and Adrienne S Lavine. *Fundamentals of heat and mass transfer*. John Wiley & Sons, 2011.

[8] Karan S Surana, Daniel Nunez, JN Reddy, and Albert Romkes. Rate constitutive theory for ordered thermoelastic solids. *Annals of solid and structural mechanics*, 3(1-2):27–54, 2012.

[9] White, F. M. *Fluid Mechanics, Seventh Edition*. McGraw-Hill, 2010.

[10] K.S. Surana and J.N. Reddy. *The Finite Element Method for Initial Value Problems*. Manuscript under preparation, 2016.

[11] Michael J Moran, Howard N Shapiro, Daisie D Boettner, and Margaret B Bailey. *Fundamentals of engineering thermodynamics*. John Wiley & Sons, 2010.

[12] Panton, R. L. *Incompressible Flow, Third Edition*. John Wiley and Sons, 2005.

[13] Surana, K. S., Ma, Y., Reddy, J. N. and Romkes, A. The Rate Constitutive Equations and their Validity for Progressively Increasing Deformation. *Mechanics of Advanced Materials and Structures*, 17:509–533, 2010.

[14] Dumbre, Abhijit C. $\boldsymbol{k}$-version of finite element method in steady 2D Newtonian fluid flows. Master's thesis, University of Kansas, Department of Mechanical Engineering, July 2004.

[15] U K N G Ghia, Kirti N Ghia, and C T Shin. High-re solutions for incompressible flow using the navier-stokes equations and a multigrid method. *Journal of computational physics*, 48(3):387–411, 1982.